



Durham E-Theses

A $CO(2)$ laser lattice experiment for cold atoms

Weatherill, Kevin J.

How to cite:

Weatherill, Kevin J. (2007) *A $CO(2)$ laser lattice experiment for cold atoms*, Durham theses, Durham University. Available at Durham E-Theses Online: <http://etheses.dur.ac.uk/2310/>

Use policy

The full-text may be used and/or reproduced, and given to third parties in any format or medium, without prior permission or charge, for personal research or study, educational, or not-for-profit purposes provided that:

- a full bibliographic reference is made to the original source
- a [link](#) is made to the metadata record in Durham E-Theses
- the full-text is not changed in any way

The full-text must not be sold in any format or medium without the formal permission of the copyright holders.

Please consult the [full Durham E-Theses policy](#) for further details.

A CO₂ Laser Lattice Experiment for Cold Atoms

Kevin J. Weatherill

A thesis submitted in partial fulfilment
of the requirements for the degree of
Doctor of Philosophy

The copyright of this thesis rests with the author or the university to which it was submitted. No quotation from it, or information derived from it may be published without the prior written consent of the author or university, and any information derived from it should be acknowledged.



Department of Physics
Durham University

January 12, 2007



18 APR 2007

A CO₂ Laser Lattice Experiment for Cold Atoms

Kevin J. Weatherill

Abstract

This thesis presents work on a laser cooling experiment designed for trapping Rb atoms in a CO₂ laser optical trap. Some emphasis is placed on experimental features designed to allow the future implementation of a neutral atom quantum computation scheme.

The experiment was built from scratch and includes the development of stable and reliable lasers for laser cooling and the construction of a double-chamber ultra-high vacuum system. The construction of a magneto-optical trap and optical molasses are discussed and results presented.

The search for a signature of atoms trapped in the CO₂ laser optical trap is described but so far no such signature has been observed. Possible reasons for this difficulty are presented

Numerical modeling of the optical potential expected from the CO₂ laser lattice has been performed and the expected experimental parameters of trap depth and oscillation frequency deduced from them.

Declaration

I confirm that no part of the material offered has previously been submitted by myself for a degree in this or any other University. Where material has been generated through joint work, the work of others has been indicated.

Kevin J. Weatherill
Durham, January 12, 2007

The copyright of this thesis rests with the author. No quotation from it should be published without their prior written consent and information derived from it should be acknowledged.

*Dedicated to Nikki and Jasmine,
for making my life complete.*

Acknowledgements

I would like to begin by thanking the secretarial and technical staff at the department of physics who's help keeps everyone's experiment running and whose assistance was vital to this work.

Many thanks must go to my supervisor Charles Adams who's constant flow of ideas has proved a real inspiration and special thanks to Ifan Hughes for his 'open door' policy, proof reading this thesis and always knowing in which book i can find the answer.

Thanks to Simon Cornish and Aidan Arnold for getting me started with LabVIEW, Erling Riis and Robert Wiley for helping to create a monumental vacuum chamber, Simon Gardiner for Matlab assistance and Matt Pritchard and Mark Bason for experimental assistance.

Mention must go to Simon, Nick, Dave, Graham, Patrick, Margaret, Mark, Steven and Andrew for 'stimulating discussions' in the coffee room and Paul Griffin for sharing the best moments in the lab, the pub and the stag night in a field.

Finally, i would like to thank all of my family and friends with special mention to Karen for putting a roof over our heads and Dad, Mam and Ian for providing the seemingly never ending encouragement and financial contributions towards my continued education.

Contents

	Page
Abstract	i
Declaration	ii
Acknowledgements	iv
Contents	v
List of Figures	ix
List of Tables	xi
1 Introduction	1
1.1 Introduction	1
1.2 Far Off-Resonant Dipole Traps and Optical Lattices	3
1.3 Light-shift Engineering	5
1.4 Quantum Information Processing	5
1.4.1 DiVincenzo's Criteria	6
1.4.2 Progress in Quantum Information Processing	7
1.4.3 Neutral Atom Quantum Information Processing	7
1.5 Thesis Layout	8
1.6 Publications Arising from this Work	10
I Theory of Optical Trapping	11
2 Laser Cooling and Trapping of Atoms	12
2.1 Introduction to Atom-Light Interactions	12
2.2 Laser Cooling	13
2.2.1 Doppler Cooling	13
2.2.2 Optical Molasses	15
2.2.3 Magneto-Optical Trap	16
2.3 Dipole Trapping	17
2.3.1 The Dipole Force	17
2.3.2 The Form of the Polarisability	19

3	Modeling the Optical Lattice	25
3.1	Gaussian Beams	25
3.2	Modeling of Optical Potentials	26
3.3	Single Beam	27
3.4	1D lattice	29
3.5	3D Lattice	33
3.6	High T_c BEC	36
II	The Experiment	38
4	The Vacuum Chamber	40
4.1	Introduction	40
4.2	The Science Chamber	40
4.3	The Pyramid Chamber	42
4.3.1	Introduction	42
4.3.2	Pyramidal MOT	43
4.3.3	Pyramid Chamber Construction	44
4.4	Assembly and Bake-out	47
4.4.1	Cleaning Vacuum Components	47
4.4.2	Re-Useable UHV Viewports	48
4.4.3	Science Chamber Assembly	49
4.4.4	Bake-out	51
4.4.5	Joining of the Vacuum Chambers	52
4.5	Summary of the Vacuum Chamber	52
5	Laser Stabilisation and Optical Setup	58
5.1	Introduction	58
5.2	Laser Development	59
5.2.1	Double Boxed Mirror Mount Design	59
5.2.2	Compact 'O' Ring Design	61
5.2.3	Compact Mirror Mount Design	62
5.3	Laser Stabilization	64
5.3.1	Dichroic-Atomic-Vapor Laser Lock (DAVLL)	65
5.3.2	Dither Lock	66
5.3.3	Polarization Spectroscopy Lock	68
5.3.4	Summary and Comparison of Locking Techniques	68
5.4	The Optical Setup	70
5.4.1	Introduction	70
5.4.2	Section 1	70
5.4.3	Section 2	74
5.5	Summary of the Optical Setup	75

6	Experimental Procedures	79
6.1	General Infrastructure	79
6.1.1	Plumbing and Laser Safety	79
6.1.2	MOT Coils and Shim Coils	80
6.1.3	Magnetic Shielding	81
6.2	Computer Control of the Experiment	82
6.2.1	Radio Frequency Electronics for AOMs	83
6.2.2	Testing of the Injection Locking	83
6.3	Optimising the Pyramid MOT	84
6.4	Atom Number Measurements	86
6.5	Temperature Measurements	87
6.5.1	Camera Calibration	89
6.5.2	Time of Flight Measurements	90
6.6	Characterisation of the Optical Molasses	93
6.7	Summary of the Experiment	95
7	CO₂ Laser	97
7.1	Introduction	97
7.2	Using the CO ₂ Laser	97
7.2.1	Installation	98
7.2.2	Beam Profiling	98
7.2.3	Initial Alignment	100
7.3	Methods of Alignment	101
7.3.1	Thermal Paper and Imaging Plates	101
7.3.2	Resonant Tracer Beam	103
7.4	Search for the Dipole Trap Signal	105
7.4.1	Time of Flight Technique	106
7.4.2	Anti-Trap Signal	106
7.5	Possible Reasons for Null Result	108
III	The Future	110
8	Discussion and Future Directions	111
8.1	Discussion	111
8.2	Improvements to the Current Setup	112
8.2.1	Absorptive Imaging	112
8.2.2	Imaging Optics	113
8.2.3	RF Power Compensation for the CO ₂ laser AOM	113
8.3	Future Experiments	113
9	Conclusion	116

IV Appendices	118
A A Note on Polarisability	119
B Light-Shifts for the Two-Level Atom	120
C Lorentz Oscillator Model	124
D Circuits	126
Bibliography	128

List of Figures

Figure	Page
1.1 Demonstration of light-shift engineering.	6
2.1 Energy level diagram for the D2 line of Rb	14
2.2 Principle of operation for the MOT	16
2.3 Beyond the Rotating Wave Approximation	21
2.4 Polarisability as a function of wavelength	22
2.5 Rb levels used to calculate α	23
2.6 Change in calculated α by adding terms	23
3.1 Cartesian axes in the laboratory frame	27
3.2 Properties of a single Gaussian beam trap	28
3.3 Properties of a 1D lattice	30
3.4 Trap frequencies of the 1D lattice	32
3.5 Radial potential of the 1D lattice	33
3.6 Properties of the 3D CO ₂ lattice	35
3.7 Trap frequencies of the 3D lattice	36
4.1 3D model of the vacuum chamber	42
4.2 A partially made science chamber	43
4.3 Polarization configuration in a pyramid MOT	44
4.4 The pyramid MOT optics and alkali dispensers	45
4.5 Pyramid MOT chamber during the test phase	46
4.6 Home-made ultra-high vacuum viewport: Schematic	50
4.7 Home-made ultra-high vacuum viewport: Photograph	51
4.8 Completed vacuum chamber viewed from the front	53
4.9 Completed vacuum chamber viewed from the back	54
4.10 Vacuum chamber as viewed from above (schematic)	55
4.11 Vacuum chamber as viewed from the side (schematic)	56
5.1 Diode laser with two isolating boxes	60
5.2 Frequency drifts of the diode laser	61
5.3 Compact diode laser design	62
5.4 Compact diode laser design	63
5.5 A Lorentzian lineshape and its derivative	64
5.6 Laser locking circuit	65

5.7	DAVLL setup	66
5.8	Dither lock setup	67
5.9	Polarisation spectroscopy setup	69
5.10	Comparison of locking spectra	71
5.11	Section 1 of the optical setup.	76
5.12	Photograph of section 1 of the optical setup.	77
5.13	Section 2 of the optical setup.	78
6.1	Photograph of the experiment from above	82
6.2	RF electronics for the AOMs	84
6.3	A false colour image of the pyramid MOT	85
6.4	Second MOT filling rate against pyramid MOT detuning	86
6.5	Second MOT lifetime measurement	88
6.6	A typical data set for temperature measurements	92
6.7	Measurement of temperature and cloud size.	93
6.8	Temperature against molasses duration	94
6.9	Temperature against light-shift	95
7.1	Desired CO ₂ laser beam path	99
7.2	CO ₂ laser knife-edge measurement setup	100
7.3	Beam profile of the CO ₂ laser	100
7.4	CO ₂ laser alignment using thermal paper	102
7.5	CO ₂ laser alignment using a thermal plate	103
7.6	Tracer beam setup for CO ₂ alignment	104
7.7	Principle of anti-trap observation	107
D.1	Differential photodiode circuit	126
D.2	MOT photodiode circuit	126
D.3	Experiment trigger circuit	127
D.4	Shutter driver circuit	127

List of Tables

3.1	Single beam laser trap parameters	31
3.2	1D lattice trap parameters	32
3.3	3D lattice trap parameters	34
5.1	Comparison of locking techniques	69

Chapter 1

Introduction

1.1 Introduction

The phenomenal success of laser cooling [1–3] has paved the way for many and varied experiments in atomic physics during the past twenty years. It has become experimentally routine to produce ensembles of atoms in the micro-Kelvin regime by making use of the dissipative radiation pressure force. At such low temperatures traps based on the relatively weak but conservative optical dipole force can be utilised. The optical dipole force is of interest because optical dipole traps and optical lattices are finding increasing use in experiments on Bose-Einstein condensation (BEC) [4–9], degenerate Fermi gases [10, 11], optical clocks [12, 13], single atom manipulation [14, 15] and cold molecule production [16–18]. In the race to produce cold and dense samples of atoms needed to produce BEC, magnetic traps gained prevalence in the atomic physics community. However, optical traps can offer a number of significant advantages over magneto-static traps in certain circumstances. Optical dipole traps allow for many and varied trapping geometries [19]. Unlike magnetic traps which can only confine weak field seeking states, optical traps allow the direct study of spinor condensates [20]. Magnetic field independent states ($m_F = 0$ spin projections) can also be confined and so precision experiments can be conducted in optical traps [12, 13, 21, 22]

The optical dipole force arises from the coherent interaction of an inhomogeneous electro-magnetic (EM) field with the induced electric dipole moment



of an atom [23, 24]. The force is conservative as it is the result of coherent scattering from and to the driving field. The atomic energy levels are shifted by this process (a phenomenon known as the light shift or ac-Stark shift [25]) and so the atoms experience a potential related to the atomic polarisability, α , and the EM field strength, \mathcal{E} ,

$$V_{\text{dipole}} = -\frac{1}{2}\alpha\mathcal{E}^2. \quad (1.1)$$

The dependence of this potential (and hence maximum trap depth, U_0) upon the experimental parameters of laser intensity, I , and detuning, Δ can be approximated as [24]

$$U_0 \propto \frac{I}{\Delta}. \quad (1.2)$$

Here $\Delta = \omega - \omega_0$, where ω is the laser frequency and ω_0 is the atomic resonance frequency. The incoherent scattering rate, Γ_{sc} , which leads to heating in the trap, scales as [24]

$$\Gamma_{\text{sc}} \propto \frac{I}{\Delta^2}. \quad (1.3)$$

Since the force an atom experiences is proportional to the gradient of the potential, an atom will be attracted to regions of high or low intensity depending upon the sign of the atomic dipole. Below resonance (red detuned) atoms are attracted to regions of high intensity and can be trapped in the focus of a single laser beam as proposed by Ashkin [23]. For blue detuned traps, atoms are attracted to regions of low intensity.

The first experiments on optical dipole trapping used a laser detuned several GHz to the red of the $D1$ line of sodium [26]. In this experiment the laser field was relatively close to resonance and so the atoms were rapidly heated from the trap. From equation 1.3 we can see that this limitation can be overcome by detuning the trapping laser further from resonance, however from equation 1.2 we can see that this necessitates an increase in trapping laser power to achieve the same trap depth. Many subsequent experiments have been performed in such Far Off-Resonance Traps (FORTs).

1.2 Far Off-Resonant Dipole Traps and Optical Lattices

The first FORT was demonstrated in 1993 on ^{85}Rb using a trapping laser detuned 63 nm below resonance [27]. Confinement times of 200 ms were observed which were limited only by background-gas collisions showing that there was negligible heating within the trap. Indeed, on the whole, the further the trap frequency is tuned from the atomic resonance frequency, the less scattering occurs. Hence, far off-resonant optical traps based on high power CO_2 laser beams with wavelength $\lambda=10.6 \mu\text{m}$ combine low photon scattering rate and deep trapping potentials. In these traps the laser has a frequency closer to d.c. than the resonance frequency of the atoms and so it is a very good approximation to use the value of the static polarisability of the atoms when calculating the trap depth. It is for this reason that these traps are known as quasi-electrostatic traps (QUESTs).

In 1995 Takekoshi *et al.* first proposed the use of a CO_2 laser to trap atoms [28]. They highlighted the quasi-electrostatic nature of the trap and showed that it could trap any ground state atom or combination of atoms since the static polarizability of all ground state atoms is positive at $10.6 \mu\text{m}$. Shortly afterwards the same group reported the first realization of CO_2 laser trapping [29] where a sample of Cs atoms was held in the focus of a single tightly focused beam. Later, observation of trapped Cs dimers was reported by the same group [30]. Elsewhere, Engler *et al.* observed trapping lifetimes of several minutes and evidence of evaporative cooling of Cs in CO_2 laser trap [31] and O'Hara *et al.* observed lifetimes of 300 s for ^6Li fermions [32].

In recent years there have been many significant results achieved in experiments which were made possible due to the properties of FORTs and QUESTs, such as:

- The first all-optical BEC [6] was observed in the group of Chapman in 2001. Using a CO_2 trap with a crossed geometry, they were able to produce a BEC of 3.5×10^4 ^{87}Rb atoms in around 2 s, much faster than possible with a magnetic trap.
- The all-optical production of a degenerate Fermi gas of ^6Li [11] was

achieved in the group of Thomas by direct evaporation from a CO₂ laser trap.

- The creation of BEC in Caesium [7] was achieved using a combination of Nd:YAG and CO₂ laser traps. The QUEST allowed Cs to be trapped in its lowest energy state and so avoided the difficulties usually experienced in evaporation (due to the scattering properties of the magnetically trapable states [33]).
- The creation of BECs of non-alkali metals have used Nd:YAG laser optical traps. First, Ytterbium [8] in 2003 and then Chromium [34] in 2005.
- The study of ultra-cold atom-molecule collisions are possible as CO₂ laser traps are able to trap both atoms and molecules simultaneously at sufficiently high densities [16, 17].
- Similarly QUESTs have allowed the simultaneous trapping of mixtures of different atomic species in any internal state [35, 36] allowing the study of spin exchange collisions as well as elastic interactions.
- The Creation of Molecular BEC in the groups of Grimm, Jin and Ketterle have used optical dipole traps [37–39]

Optical lattices [40] are created when two or more laser beams are combined to form an interference pattern. To create a N dimensional lattice one requires at least $N+1$ laser beams. In contrast to condensed matter systems, an optical lattice is free from defects. Also, the depth, periodicity and structure of the lattice can be changed by changing laser parameters. Many condensed matter properties, such as band structure, have been observed for atoms in optical lattices [41].

Work of particular relevance to this thesis was performed by the group of Martin Weitz formerly of the Max Planck Institute in Garching and subsequently at the University of Tübingen. In 1998 a CO₂ laser optical lattice with laser cooled Rb atoms was demonstrated [42, 43]. The group then developed techniques to image individual lattice sites and highlighted the possibilities towards quantum engineering this allows [44, 45]. Ceninni *et al.*

later created BEC within the CO₂ laser trap [46] and then an atom laser was demonstrated by lowering the optical dipole potential [47].

1.3 Light-shift Engineering

Problems in the loading of deep CO₂ optical lattices were reported by Schuennemann in reference [44]. In Rb, at 10.6 μm the polarisability of the excited $5P$ state is approximately 2.5 times that of the $5S$ ground state [48]. This difference in polarisabilities means that the atomic resonance frequency becomes intensity dependent and laser cooling becomes ineffective at the centre of deep CO₂ traps for typical laser cooling parameters. In previous work at Durham we attempted to overcome the problems of loading the centre of deep optical traps by using an auxiliary laser field to cancel the differential light shifts of the atomic states used for laser cooling [49–51]. We demonstrated that the loading of atoms into the centre of a CO₂ laser lattice could be greatly enhanced by using this method. Further to that, we demonstrated that specifically chosen regions of the lattice could be loaded while the rest of the lattice is left unoccupied. Figure 1.1 a) shows the enhanced loading of a CO₂ lattice using this method. Figure 1.1 b) shows the selective loading of a specific region of the lattice.

The ability to load selectively specific lattice sites with cold atoms is an attractive prospect for array initialisation in quantum information processing (QIP) schemes based on neutral atoms in optical lattices.

1.4 Quantum Information Processing

Fifteen years ago QIP was little more than an interesting theoretical concept. The idea of using quantum bits or qubits [52] instead of classical binary digits to perform calculations was then an unrealistic experimental goal. However the explosive advances in quantum control (due to laser cooling of atoms and ions and advances in other fields), have brought quantum computation several steps closer.

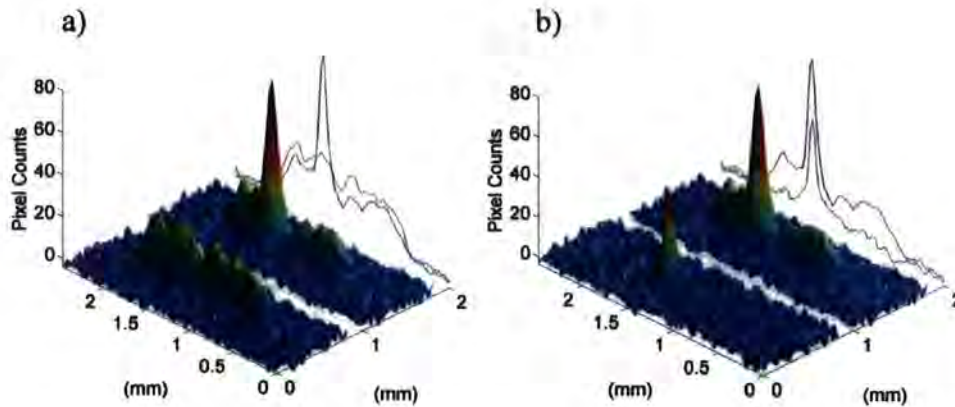


Figure 1.1: Demonstration of light-shift engineering. a) Loading can be enhanced in the centre of the lattice. The plot at the front is the CO_2 lattice alone and the rear plot contains the auxiliary field b) Specific regions of an optical lattice can be chosen to be loaded with cold atoms. The front plot shows atoms loaded into the combined trap during a blue detuned molasses phase. The rear plot during a red detuned molasses phase. Pixel counts are proportional to atom number.

1.4.1 DiVincenzo's Criteria

In 2000 DiVincenzo proposed certain criteria [53] that must be fulfilled before QIP could be usefully implemented.

1. A scalable physical system with well characterised qubits
2. The ability to initialise the state of the qubits
3. Long relevant decoherence times, much longer than the gate operation time
4. A universal set of quantum gates.
5. A qubit specific measurement capability
6. The ability to interconvert between stationary and flying qubits
7. The ability to faithfully transmit flying qubits between specified locations.

The successful application of these criteria has become the goal of many experimentalists worldwide and many advances have been made [54].

1.4.2 Progress in Quantum Information Processing

The early leaders in the field of experimental QIP were researchers using nuclear magnetic resonance (NMR) techniques on chain molecules. In 2001 workers from IBM and Stanford University used a molecule with seven spin $1/2$ nuclei to factor the number 15 into its prime factors by Shor's algorithm [55]. Although an impressive result, this QIP scheme struggles to meet the first of the Divincenzo criteria because the use of internal chemistry to define the qubits is not scalable. Probably the most promising QIP scheme to date involves ion trapping. Trapped ions offer very long coherence times, implying a very robust qubit memory. State preparation and readout are also highly efficient and have recently allowed the quantum Fourier transform to be implemented on Beryllium ions [56]. There are however serious doubts over whether ion trapping QIP schemes are scalable and whether motional decoherence due to stochastic fields from imperfect electrode surfaces can be eradicated. Although work is underway to address these issues (see for example reference [57]), atoms are seen by many as an attractive alternative as their neutrality protects them from many environmental decoherence effects.

1.4.3 Neutral Atom Quantum Information Processing

The simple and well understood quantum level structure of atoms and the ability to prepare atoms in specific (and known) states have inspired much research into devising practical methods for atomic QIP. Atoms in optical lattices can provide a ready-made quantum register which is scalable to many qubits. The neutrality of atoms provide attractively long decoherence times but it also encumbers the interactions that are essential for creating entanglement between particles. Two schemes to create entangled atomic states were proposed by Jaksch *et al.* One uses the dipole-dipole interactions of Rydberg atoms [58], the other uses controlled collisional phase shifts to entangle many atoms [59]. The latter scheme has been demonstrated in the

ground-breaking experiments of Immanuel Bloch [60, 61].

Although much progress has been achieved in a short time, the main stumbling block for optical lattice QIP is the inability to address individual lattice sites. The large lattice spacing of traps in the far infra-red allow this particular hurdle to be overcome but can then fall foul of different problems such as register initialisation (since the Mott insulator transition cannot be used at these wavelengths to obtain unity occupation of lattice sites, unlike the near resonant lattice in references [60–63]). In the group of Meschede, a quantum register was demonstrated with Cs atoms in a Nd:YAG laser lattice [64]. A high gradient MOT was used as a source of single atoms [65] which were loaded into a traveling wave lattice which can be controlled with sub-micron precision [66]. An optical tweezer was used to ‘manually’ place single atoms at desired locations to initialise the register [67]. In other work Yavuz *et al* have demonstrated fast ground state manipulation in Rb [68] for preparing qubit states in optical traps spaced by $\sim 5 \mu\text{m}$ apart. There are also proposed schemes to initialise a quantum register in a CO₂ laser lattice [69] and to manipulate atoms at individual sites [70].

To understand better the context of this work, it is important to know the long term aims of our research grant; to control single atoms and create entanglement between pairs of atoms (or BECs) by state selectively moving and addressing atoms within a CO₂ laser lattice. Although the execution of much of this work is beyond the scope of this thesis, much of the groundwork for these goals is described here and many features of the experimental setup are geared towards these longer term goals.

1.5 Thesis Layout

This thesis describes the design, construction and implementation of an experiment for cooling and trapping Rb in a CO₂ laser optical lattice. The document is structured in three parts: the first considers the theory of atom light interactions and modeling of optical potentials. The second considers the experiment itself. The final part considers future directions and improvements to the experiment. The chapter breakdown is as follows;

-
- Chapter 2 outlines the theory of atom-light interactions needed to understand the laser cooling and optical trapping of neutral atoms with particular emphasis on optical dipole trapping.
 - Chapter 3 contains details of the numerical modeling of the optical dipole potentials expected to be created by the CO₂ laser.
 - A description of experimental setup begins in chapter 4 with details of the design and construction of the vacuum system used in the experiment.
 - Chapter 5 describes the design and development of the laser system. Details of the optical setup, injection locking and the frequency stabilisation techniques employed are included.
 - Chapter 6 describes the optimisation and everyday running of the laser cooling experiment and the techniques for precision timing of the experiment using computer control. Details of temperature measurements are given.
 - Chapter 7 gives an account of how the CO₂ laser is included in the experiment. A description of the many alignment techniques used in the search for the dipole trap signal is given.
 - Chapter 8 discusses the limitations of the current experimental setup and outlines future directions, including suggestions for improvements to the current experimental setup.
 - Finally, conclusions are drawn in Chapter 9.

1.6 Publications Arising from this Work

Fast switching of alkali atom dispensers using laser induced heating.

P. F. Griffin, K. J. Weatherill and C. S. Adams.

Rev. Sci. Inst. **76**, 093102 (2005).

Loading of selected sites in an optical lattice using light-shift engineering.

P. F. Griffin, K. J. Weatherill, S. G. Macleod, R. M. Potvliege and C. S. Adams.

Proceedings of the XVII International Conference of Laser Spectroscopy, p307 (2005).

Spatially selective loading of an optical lattice by light shift engineering using an auxiliary laser field.

P. F. Griffin, K. J. Weatherill, S. G. MacLeod, R. M. Potvliege and C. S. Adams.

New. J. Phys. **8**, 11 (2006).

Re-usable Ultra-high Vacuum Windows

K. J. Weatherill, C. S. Adams and E. Riis

In Preparation.

Part I

Theory of Optical Trapping

Chapter 2

Laser Cooling and Trapping of Atoms

Since its conception in 1975 [71, 72] laser cooling has revolutionized the field of atomic physics research, an achievement that has been recognized by the awarding of the Nobel prize for Physics to the founders of the experimental techniques in 1997 [73–75]. No attempt will be made to describe in detail the principles behind laser cooling. Such material may be found in numerous sources, of which references [1, 3, 76, 77] are but a few. A brief outline of the underlying principles of atom-light interactions is presented here. Greater detail is supplied for topics particular to CO₂ laser trapping.

2.1 Introduction to Atom-Light Interactions

The force exerted on an atom by light can be split into two components.

- The optical *dipole* force is dispersive and proportional to the gradient of the field and the real component of the atomic dipole. This is the force which can trap an atom in the focus of a laser beam. It is conservative and therefore can be represented by a potential.
- The *spontaneous* force or *radiation pressure* force is dissipative and proportional to the gradient of the phase and the imaginary component of the atomic dipole. This force is responsible for the cooling and

trapping described in the following section.

2.2 Laser Cooling

In Doppler cooling, the Doppler effect is used to provide a velocity dependent force. Typically, lasers with a linewidth much narrower than the atomic transition are used. A requirement of laser cooling is that the system have a closed (or almost closed) transition such that the atoms remain in the cooling cycle. Alkali metals readily satisfy this requirement since for atoms undergoing transitions from the upper hyperfine state of the ground term F to an excited state with $F' = F + 1$ the atom must decay back to the upper hyperfine state. This is due to the selection rule $\Delta F = 0, \pm 1$. The finite width of the excited state allows some excitation to the excited state with $F' = F$ and atoms can be lost from the cooling cycle. A repumping laser can return this population to the upper hyperfine state. Figure 2.1 shows the hyperfine levels in the ground term and excited $5P_{3/2}$ level for ^{85}Rb and ^{87}Rb . The transitions used for cooling and for repumping are highlighted in red and blue respectively.

2.2.1 Doppler Cooling

In Doppler cooling, a friction-like force is used to cool the atoms. The force originates from the recoil kick an atom experiences when it absorbs a photon from a laser beam. The excited state decays by spontaneous emission in time $\tau = 1/\Gamma$ (where Γ is the natural linewidth of the excited state) in a random direction. The result is that over many absorption-spontaneous emission cycles the recoil from emission processes averages to zero. The atom receives net momentum in the direction of the wavevector \mathbf{k} of the laser beam at each absorption event.

From the *optical Bloch equations* (see for example [25]) we can calculate the scattering rate for an atom to be

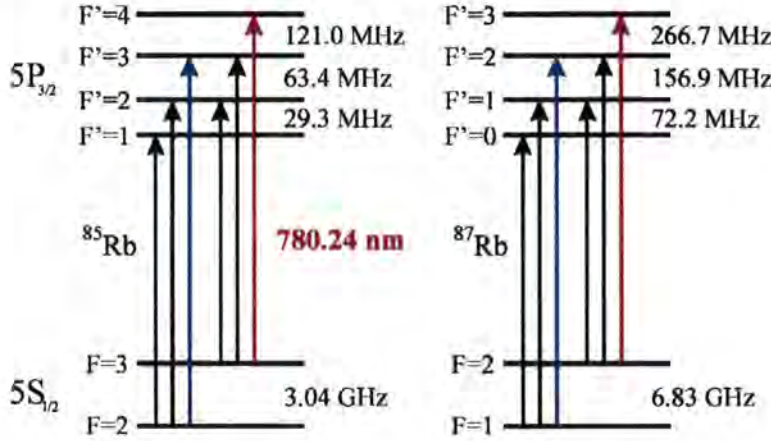


Figure 2.1: Energy level diagram for the D2 line of Rb. Allowed transitions are shown between the ground $5S_{1/2}$ and the excited $5P_{3/2}$ states. The cycling ‘cooling’ transitions are shown in red. The recycling ‘repump’ transitions are shown in blue. Values are stated for transitions in vacuum and are reproduced from reference [78].

$$\Gamma_{\text{sc}} = \frac{\Gamma}{2} \frac{I/I_s}{1 + I/I_s + 4(\Delta/\Gamma)^2}. \quad (2.1)$$

Here I_s is the saturation intensity and can be thought of as the photon energy (hc/λ) per unit time ($\tau = 1/\Gamma$) per unit area ($\sim \lambda^2$)

$$I_s = \frac{2\pi^2 \hbar \Gamma c}{3\lambda^3} \quad (2.2)$$

and λ is the wavelength, \hbar is Planck’s constant divided by 2π and c is the speed of light.

The force experienced by a stationary atom in the laser beam is then

$$\mathbf{F}_{\text{sc}} = \frac{\hbar \mathbf{k} \Gamma}{2} \frac{I/I_s}{1 + I/I_s + 4(\Delta/\Gamma)^2}, \quad (2.3)$$

where \mathbf{k} is the wave vector ($|\mathbf{k}| = 2\pi/\lambda$)

At low intensity $\mathbf{F}_{\text{sc}} \propto I$. and at high intensity saturates to $\hbar \mathbf{k} \Gamma / 2$. The *Doppler shift* introduces a velocity dependence to the force as the detuning (Δ in equation 2.3) becomes $\Delta = (\omega - \omega_0 - \mathbf{k} \cdot \mathbf{v})$.

In the limit of low intensity, the Doppler cooling temperature limit is given

by (see for example [1]),

$$T_D = \frac{\hbar\Gamma}{2k_B}. \quad (2.4)$$

k_B is Boltzmann's constant. The temperature is governed only by the linewidth of the cooling transition and not any other properties of the atom (such as the mass). The first 3D demonstration of Doppler cooling was reported by Chu *et al* in 1985 [79]. This type of cooling is characterised by a friction coefficient that depends on laser intensity and an effective velocity capture range of order $\pm\Delta/k$

2.2.2 Optical Molasses

Temperatures much colder than the Doppler limit are routinely achieved in 3D optical molasses. To understand the effects responsible, we need to consider the multi-level nature of atoms and the polarisation gradients that are unavoidable in 3D cooling schemes. Here we will give a brief phenomenological explanation of sub-Doppler cooling and direct the interested reader to the quantitative theories contained in references [80, 81].

The multi-level nature of atoms allows optical pumping between Zeeman sub-levels which results in population transfer between the levels through absorption/spontaneous emission cycles. In equilibrium, the population is pumped to the most light-shifted state (this is equivalent to aligning the atomic dipole with the field). The key point arises when we consider an atom in motion through regions of varying polarisation. The timescale for optical pumping is typically several natural lifetimes and the state of the atom doesn't have time to adjust. For $\text{lin}\perp\text{lin}$ polarisation the atom is transferred non-adiabatically to a superposition of states with higher energy. Cooling follows since the atom has increased its internal energy at the expense of kinetic energy. For $\sigma^+-\sigma^-$ polarisation, when an atom starts to move (for instance towards the σ^+ beam) the symmetry is broken and the atom is pumped towards positive m_F levels. The effect is run-away because the positive m_F levels couple more strongly to the light. Cooling results because this motionally induced redistribution of population leads to a larger scattering rate from the beam opposing the atomic motion. In 3D optical molasses, both $\text{lin}\perp\text{lin}$ and $\sigma^+-\sigma^-$ polarisation configurations are present. Sub-Doppler cooling is characterised

by a large friction coefficient that is independent of (and a small capture velocity that is proportional to) the laser intensity. For low I , the light shifts of the atomic states and the optical pumping rates are proportional to I . Long optical pumping times compensate for weaker light-shifts. For large detunings ($|\Delta| > 5\Gamma$) the temperature is proportional to $I/|\Delta|$. Theory calculates the limit to this cooling mechanism to be of the order of a few times the recoil temperature [82]. In the laboratory, optical molasses can be achieved after a Magneto-optical Trap (MOT) (see the next section) has pre-cooled the atoms by turning off the magnetic field gradient and reducing $I/|\Delta|$. In Rb, temperatures of below $2 \mu\text{K}$ have been achieved [83].

2.2.3 Magneto-Optical Trap

The most widely used trap for neutral atoms is the magneto-optical trap. Since its first demonstration in 1987 [84] the MOT has become prevalent in atomic physics experiments due to its versatility and robustness. It has been the subject of many studies [85–89]. The MOT provides both cooling and trapping of atoms and can be routinely used to cool room temperature gases to a fraction of a mK. The principle of operation of the MOT is most easily explained for the 1-D configuration illustrated in figure 2.2.

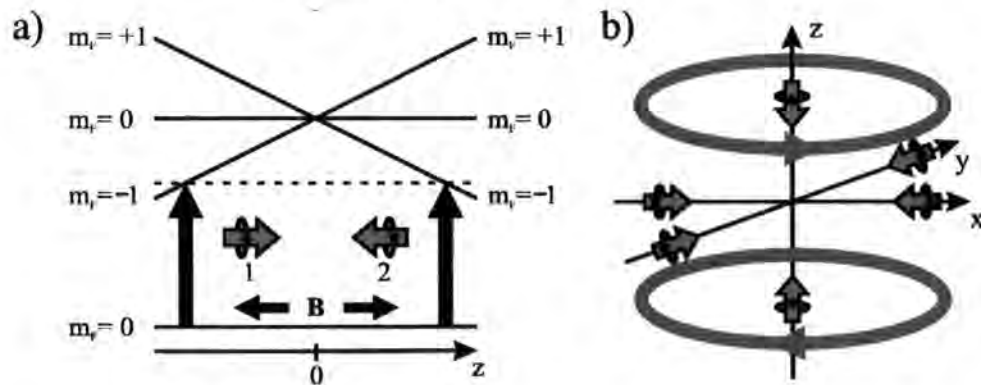


Figure 2.2: Principle of operation for the MOT. a) 1 D representation showing the atomic energy levels in the spatially varying field. Laser beam 1 drives σ^- transitions for $z < 0$ and σ^+ transitions for $z > 0$. The converse is true for beam 2. b) Extension to 3D, a quadrupole field is produced by coils with currents of opposite sense.

There is a magnetic field of the form $B = b|z|$ which lifts the degeneracy of the magnetic sublevels by an increasing amount away from the center of the trap ($z = 0$). By using red-detuned laser light, atoms moving away from the centre of the trap are Zeeman shifted into resonance with a laser beam which pushes it back to the centre. The force experienced by the atoms is the combined force from the counter-propagating beams and for small velocities and displacements can be given by

$$F = -\beta v - \kappa z, \quad (2.5)$$

Where β is a friction coefficient and κ is a 'spring constant'. The atoms are hence trapped by this position dependent force. In practise, 3D cooling and confinement of atoms is achieved by using three sets of orthogonal counter-propagating laser beams. A MOT can cool atoms to well below the Doppler limit [90].

2.3 Dipole Trapping

We will now consider the dispersive force due to atom-light interaction. This is the basis for dipole trapping experiments. In many situations it is sufficient to approximate the atom as a two-level structure and make the famous rotating wave approximation (RWA) [91]. In the case of CO₂ laser trapping of Rb however, this is not an adequate model as $\omega_0 \simeq 14\omega$ so $\omega_0 + \omega \simeq \omega_0 - \omega$. We will instead consider the atomic polarisability (for a note on polarisability see Appendix A).

2.3.1 The Dipole Force

Consider an atom in a laser beam. The electric field, $\mathcal{E} = \mathcal{E}_0 \cos(\omega t)$ induces a dipole moment, \mathbf{d} , in the atom which oscillates at the frequency of the driving field. The atomic dipole and the field are related by

$$\mathbf{d} = \alpha(\omega)\mathcal{E}, \quad (2.6)$$

where α is the complex polarizability of the atom and is a function of the frequency of the applied field. Assuming the atom has a linear response to

the field, as in equation 2.6, we can write the instantaneous electrostatic energy as [92]

$$V_{\text{inst}} = \int_0^{\mathcal{E}} -\mathbf{d}(\mathcal{E}) \cdot \delta\mathcal{E} \quad (2.7)$$

$$= -\frac{1}{2} \mathbf{d} \cdot \mathcal{E}. \quad (2.8)$$

Substituting in the atomic dipole and taking the time average of the field gives us,

$$V_{\text{dipole}} = -\frac{1}{4} \text{Re}(\alpha) \mathcal{E}_0^2. \quad (2.9)$$

Writing the potential in terms of intensity, $I = (1/2)\epsilon_0 c \mathcal{E}_0^2$, gives,

$$V_{\text{dipole}} = -\frac{\text{Re}(\alpha)I}{2\epsilon_0 c}. \quad (2.10)$$

V_{dipole} is equivalent to the light-shift of the atomic state [25].

It is often convenient to describe the potential in terms of experimentally measurable quantities and so we can rewrite equation 2.10 in terms of the laser beam power and size. For a Gaussian beam with $1/e^2$ radius of w_0 (described later in equation 3.1) the peak intensity and the laser beam power are related by $I = 2P/\pi w_0^2$, giving a maximum trap depth, U_0 , of

$$U_0 = -\frac{\text{Re}(\alpha)P}{\epsilon_0 c \pi w_0^2} \quad (2.11)$$

The optical *dipole force* occurs due to gradients in the light field, ie,

$$\begin{aligned} \mathbf{F}_{\text{dipole}} &= -\nabla V_{\text{dipole}} \\ &= \frac{1}{2\epsilon_0 c} \text{Re}(\alpha) \nabla I. \end{aligned} \quad (2.12)$$

If the frequency of the driving field is below that of an atomic resonance then \mathbf{d} will be in phase with \mathcal{E} and, from equation. 2.6, α will be positive. Thus 3D confinement can be realised in the simple geometry of a focussed laser beam that is red-detuned from an atomic resonance, as was proposed by Ashkin in 1978 [23]. If the driving field is above resonance then the dipole will oscillate out of phase and the atom will be attracted to regions of low intensity. In such *blue detuned* traps, atoms can be confined to regions of low intensity allowing long coherence times to be observed [93].

The imaginary part of the polarisability results in absorption. The power of which can be expressed as,

$$P_{ab} = \frac{\omega}{\epsilon_0 c} \text{Im}(\alpha) I \quad (2.13)$$

The power absorbed is re-emitted and can be interpreted in terms of photon scattering. The rate of which is then given by

$$\Gamma_{sc} = \frac{P_{ab}}{\hbar\omega} = \frac{1}{\hbar\epsilon_0 c} \text{Im}(\alpha) I \quad (2.14)$$

Now to proceed further, we need to consider the form of the polarisability, α .

2.3.2 The Form of the Polarisability

In general, the atomic polarisability is a tensor and it depends on the frequency of the driving field. It can also take very different values depending on the atomic state. For example, spherically symmetric S orbitals are much less polarisable than states with non-zero orbital angular momentum. The polarisability can be derived from perturbation theory (see for example [94]) to be

$$\alpha(\omega) = \frac{2e^2}{3\hbar} \sum_f \frac{\omega_{if} |\langle i|\mathbf{r}|f\rangle|^2}{(\omega_{if} - \omega - i\Gamma_f/2)(\omega_{if} + \omega + i\Gamma_f/2)}. \quad (2.15)$$

Here i denotes the initial state of the atom and f denotes some other level. Γ_f is the linewidth of the upper level and

$$\mathbf{r} = \sum_{\text{all electrons}} \mathbf{r}_i.$$

Accounting for the polarisability of all electrons in the atom is a difficult prospect and is achieved by Safronova *et al.* by using many-body relativistic calculations with a random phase approximation to account for the core electrons [95, 96].

Having neither the time or the know-how to perform such calculations we look for an easier approach to determine the polarisability of Rb atoms at CO₂ laser wavelength. Since the photon scattering rates from CO₂ laser traps

are so low [32], we will consider only the real part of the polarisability as this is responsible for the light shift of the atom. We will also consider only the valence electron and assume that the detuning is large and the atomic excited state population is negligible.

Two-Level Atom

The light shift of a two-level atom in the RWA can be easily calculated from time-dependent perturbation theory. The result is well known and is derived in references [76, 77] and in Appendix B for completeness. The energy shift is

$$\Delta E = \frac{\hbar\Omega^2}{4\Delta}, \quad (2.16)$$

where Ω is the Rabi frequency and is defined as

$$\Omega = \langle i|d|f\rangle \frac{\mathcal{E}}{\hbar}. \quad (2.17)$$

During the derivation of equation 2.16, if the counter-rotating terms are kept (equation B.16) then the equations are insoluble and it is not possible to find an expression for the light shift directly in this way. However, if $1/\Delta = (\omega_0 - \omega)$ from equation 2.16 is replaced with an effective detuning of $1/\Delta_e = \left(\frac{1}{\omega_0 - \omega} + \frac{1}{\omega_0 + \omega}\right)$ then we find that the new expression for the light shift is

$$\Delta E = \frac{\hbar\Omega^2}{4} \left(\frac{1}{\omega_0 - \omega} + \frac{1}{\omega_0 + \omega} \right), \quad (2.18)$$

which matches that derived from the Lorentz oscillator model derived in reference [24] and Appendix C and from using coupled Floquet equations (derived in Appendix C of reference [51]).

Figure 2.3 shows the optical dipole potential for a two-level atom. The red line shows the calculated optical dipole potential using the RWA. The blue line is the same calculation but with the counter-rotating term retained. The plot shows how the contribution of the counter-rotating term makes the potential deeper and how the sign of the potential changes on either side of resonance ($\lambda/\lambda_0 = 1$). The plot also show how the potential approaches the static polarisability limit at the CO₂ laser wavelength.

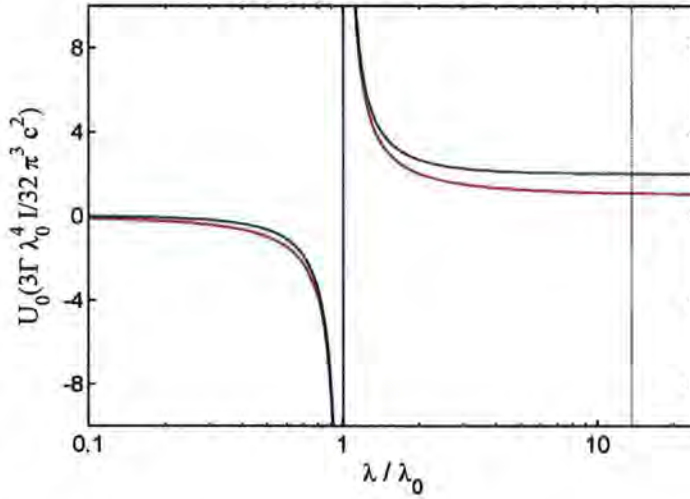


Figure 2.3: The optical dipole potential calculated using the rotating wave approximation (red) and keeping the counter rotating term (blue). The dashed line denotes the CO₂ laser wavelength.

Adding more levels

Of course Rb atoms are not simple two-level systems and other energy levels make a contribution to the polarisability of the ground state. By substituting equation 2.17 into equation 2.16 and summing over all electric-dipole allowed transitions we get

$$\Delta E_i = -\frac{\mathcal{E}^2}{4\hbar} \sum_{i \neq f} |\langle i|\mathbf{d}|f\rangle|^2 \left(\frac{1}{\omega_{if} - \omega} + \frac{1}{\omega_{if} + \omega} \right) \quad (2.19)$$

Using the Wigner-Eckart theorem [97], the matrix elements $\langle i|\mathbf{d}|f\rangle$ can be separated into the product of a Clebsch-Gordan coefficient $\langle F, m_F|F', 1, m_F, \epsilon\rangle$ and a reduced matrix element $\langle F||\mathbf{d}||F'\rangle$

$$\langle i|\mathbf{d}|f\rangle = \langle F, m_F|F', 1, m_F, \epsilon\rangle \langle F||\mathbf{d}||F'\rangle. \quad (2.20)$$

Here ϵ is the polarisation vector. $\epsilon = 0, \pm 1$ for π, σ^\pm transitions respectively. The reduced matrix element can be further decomposed [98],

$$\langle F||\mathbf{d}||F'\rangle = \langle J||\mathbf{d}||J'\rangle (-1)^{F'+J+1+I} \sqrt{(F'+1)(2J+1)} \begin{Bmatrix} J & J' & 1 \\ F' & F & I \end{Bmatrix}. \quad (2.21)$$

At large detuning the hyperfine structure can be neglected and making use of the expression for the Einstein A coefficient [99]

$$A_{if} = \frac{\omega_{if}^2}{3\pi\epsilon_0\hbar c^3} \frac{2J+1}{2J'+1} |\langle J||\mathbf{d}||J' \rangle|^2 \quad (2.22)$$

gives us

$$\Delta E_i = \frac{3\pi c^2 I}{2} \sum_{f \neq i} \frac{A_{if}}{\omega_{if}^3} \left(\frac{1}{\omega_{if} - \omega} + \frac{1}{\omega_{if} + \omega} \right) \quad (2.23)$$

and hence from equation 2.10 the real component of the polarisability is,

$$\text{Re}(\alpha) = -3\pi\epsilon_0 c^3 \sum_{f \neq i} \frac{A_{if}}{\omega_{if}^3} \left(\frac{1}{\omega_{if} - \omega} + \frac{1}{\omega_{if} + \omega} \right). \quad (2.24)$$

Figure 2.4 shows the real component of the polarisability for ground state Rb (in atomic units) plotted as a function of wavelength. The red curve is the two level model (D2 transition) and the blue curve includes eight strongest transitions (see figure 2.5) from the ground state. Values for the wavelengths and Einstein A coefficients were taken from reference [100]. We can see that although adding the contribution of more transitions changes the polarisability drastically in the vicinity of the transition, at the CO₂ wavelength there is very little change. Figure 2.6 shows the percentage change in the value of the polarisability at 10.6 μm with added terms.

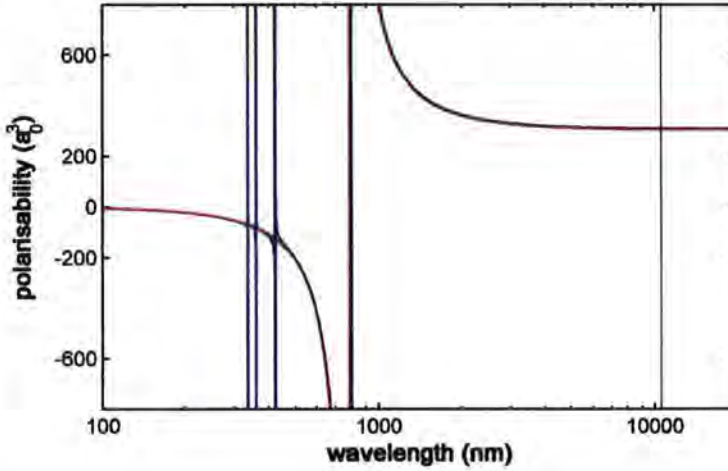


Figure 2.4: The real component of the atomic polarisability as a function of wavelength. The vertical black line denotes the CO₂ laser wavelength.

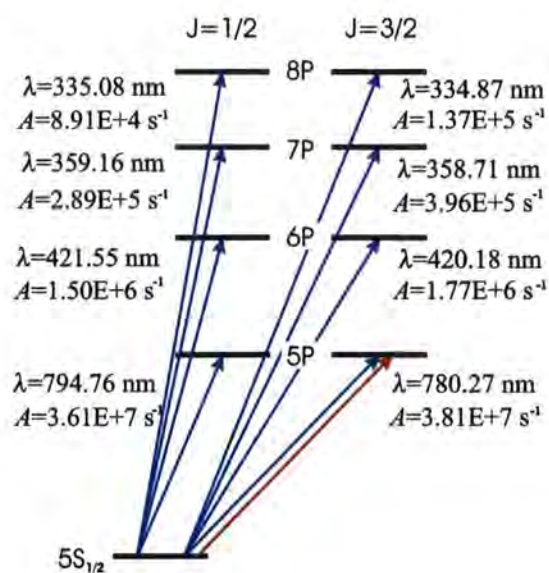


Figure 2.5: Energy level diagram for Rb with the transitions used to calculate α . The transitions shown in red and blue were used to calculate the red and blue lines in figure 2.4 respectively.

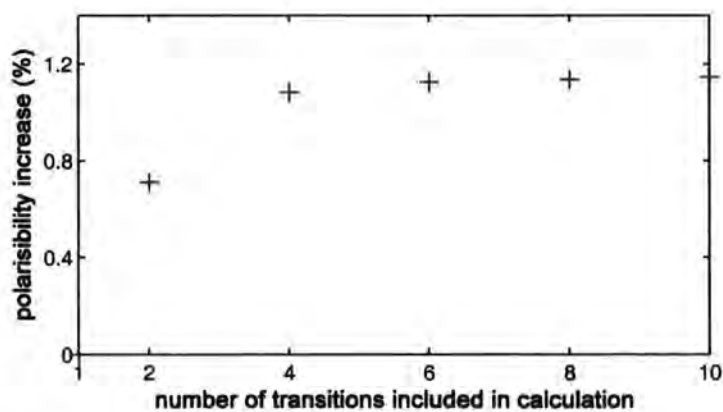


Figure 2.6: Change in the calculated value of the polarisability as more transitions are included. There is negligible change beyond four transitions.

Tensor Polarisability

For most ground state atoms (and other systems with spherical symmetry) the polarisability at a particular applied wavelength is the same regardless of the direction of the applied field and so can be represented by a single scalar quantity (as in the above analysis). For non-spherical systems this is not the case and the polarisability can be decomposed such that for linearly polarised light

$$\alpha = \alpha_0 \mathbf{1} + \alpha_2 \mathbf{Q} \quad (2.25)$$

where α_0 is the scalar polarisability and corresponds to the dipole being induced in the direction of the applied field, $\mathbf{1}$ is the unitary matrix, α_2 is a second rank tensor and corresponds to an induced dipole perpendicular to the applied field. This tensor polarisability mixes the hyperfine and magnetic sublevels via the operator \mathbf{Q} [101, 102].

For the lightshift engineering experiments described in section 1.3, we concerned ourselves with calculating α_0 and α_2 because we needed to know the effect of two applied fields on the hyperfine levels of the $5S$ and $5P$ states of Rb. Details of these calculations can be found in references [49–51]. Calculated values for α_0 and α_2 for many low-lying levels of Rb can be found in reference [103]. In this work however, only one applied field is considered, that of the CO_2 laser and knowledge of α_2 is not necessary. In the next chapter we model the optical potentials we expect to achieve for ground state atoms in the CO_2 laser beam simply using the two-level atom model (as we know the results will be accurate to about 1%). When considering excited state shifts we will use values for the static polarisability [48].

Chapter 3

Modeling the Optical Lattice

Before trying to create and characterize dipole traps and optical lattices in the laboratory it is important to know what to expect. For instance, if we want to use the method of parametric driving to measure the frequencies of the trap [42], then having a calculated estimate would speed up this procedure immensely by making it easier to find the resonances. For this reason, this chapter is devoted to the numerical simulation of optical traps based on the expected experimental parameters. This technique could also allow us to estimate the effects of misalignment and power imbalances of the lattice beams, although this is not discussed here.

3.1 Gaussian Beams

The simplest optical trap is a tightly focused, red detuned single beam as discussed in section 2.3. In the sections that follow, we model the optical potential experienced by atoms in CO₂ lasers beams. The beams are assumed to be of circular Gaussian profile traveling in the z -direction. i.e.

$$\mathcal{E}(r, z) = \mathcal{E}_0 \epsilon \frac{w_0}{w(z)} e^{i(kz - \omega t)} e^{-i\alpha(z)} e^{-r^2/w(z)^2} e^{ikr^2/2R(z)}. \quad (3.1)$$

Here w_0 is the beam waist, $w(z)$ is the beam width at distance z from the focus, α is the Gouy phase (defined as $\tan^{-1}(z/z_R)$) and $R(z) = z + (z_R^2/z)$, z_R is the Rayleigh range and is defined as $z_R = \pi w_0^2/\lambda$. ϵ is the polarisation vector.

The component parts of equation 3.1 can be explained as follows [104],

\mathcal{E}_0	maximum scalar amplitude of the electric field (on axis at waist),
$\frac{w_0}{w(z)}$	amplitude gets smaller away from waist,
$e^{i(kz-\omega t)}$	wave traveling in z -direction,
$e^{-i\alpha(z)}$	additional (Gouy) phase change with z ,
$e^{-r^2/w(z)^2}$	transverse Gaussian profile,
$e^{ikr^2/2R(z)}$	wavefronts have radius of curvature $R(z)$.

A thorough discussion of the properties of Gaussian beams and their propagation can be found in reference [105].

3.2 Modeling of Optical Potentials

It is often difficult to visualize (and sometimes calculate) the electric field intensity due to interfering laser beams, especially if many beams are used. In this case a numerical approach was used to calculate the electric field intensity due to Gaussian laser beams at specific points in space. Initially, a meshgrid is defined with x , y and z in the laboratory frame. For each laser beam the coordinates are then rotated through angles θ and ϕ about the x and z axes respectively to transfer into a set of cartesian coordinates x' , y' and z' where z' is defined as the direction of propagation of the laser beam, see figure 3.1. The new coordinates are calculated by multiplying the original coordinates by Euler matrices as in equation 3.2.

$$\begin{pmatrix} x' \\ y' \\ z' \end{pmatrix} = \begin{pmatrix} \cos \theta & 0 & -\sin \theta \\ 0 & 1 & 0 \\ \sin \theta & 0 & \cos \theta \end{pmatrix} \begin{pmatrix} \cos \phi & \sin \phi & 0 \\ -\sin \phi & \cos \phi & 0 \\ 0 & 0 & 1 \end{pmatrix} \begin{pmatrix} x \\ y \\ z \end{pmatrix}$$

$$\begin{pmatrix} x' \\ y' \\ z' \end{pmatrix} = \begin{pmatrix} x \cos \theta \cos \phi + y \cos \theta \sin \phi - z \sin \theta \\ -x \sin \phi + y \cos \phi \\ x \cos \phi \sin \theta + y \sin \theta \sin \phi + z \cos \theta \end{pmatrix} \quad (3.2)$$

The \mathcal{E} field due to each laser beam is then calculated for each point on the grid and then its components resolved back into x , y and z in the laboratory

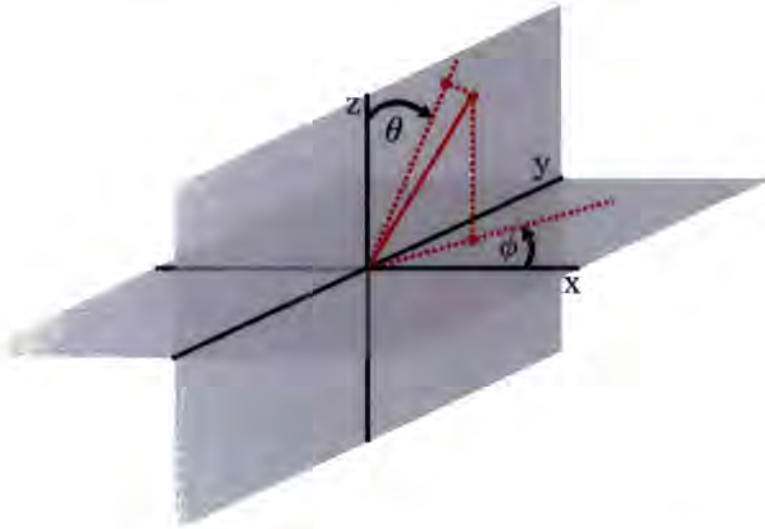


Figure 3.1: Cartesian axes in the laboratory frame. The red solid line depicts a laser beam whose orientation is defined by the angles θ and ϕ with respect to the z and x axes.

frame. This approach is far from the most numerically efficient way to model the electric field due to a laser beam described by equation 3.1. This method does however allow the intensity pattern for an arbitrary number of beams at arbitrary angles to be calculated. Once calculated, cuts and slices through the potential can be obtained to facilitate analysis of the shape, depth and trapping frequency of the wells. The electric field intensity is converted into ground state trap depth via equation 2.23. In the following sections, this modeling technique is applied to investigate the trapping of ground state atoms in a single beam trap, a 1D lattice and a 3D lattice derived from CO_2 laser beams at $\lambda = 10.6 \mu\text{m}$. The realistic laser parameters remain constant for each case, power $P = 60 \text{ W}$ and $w_0 = 50 \mu\text{m}$. All trap frequencies are calculated for ^{85}Rb atoms.

3.3 Single Beam

From equation 3.1 the inherent volume-depth trade-off of a single focused laser beam trap is immediately apparent. The smaller the focus of the beam,

the deeper the trap. Figure 3.2 a) shows an intensity profile cut through a single beam trap. The potential depth experienced by atoms in the laser beam is proportional to the square modulus of the electric field, ie. the intensity, as discussed in section 2.3.1. The trapping potential can therefore be described by the square of equation 3.1 ie.

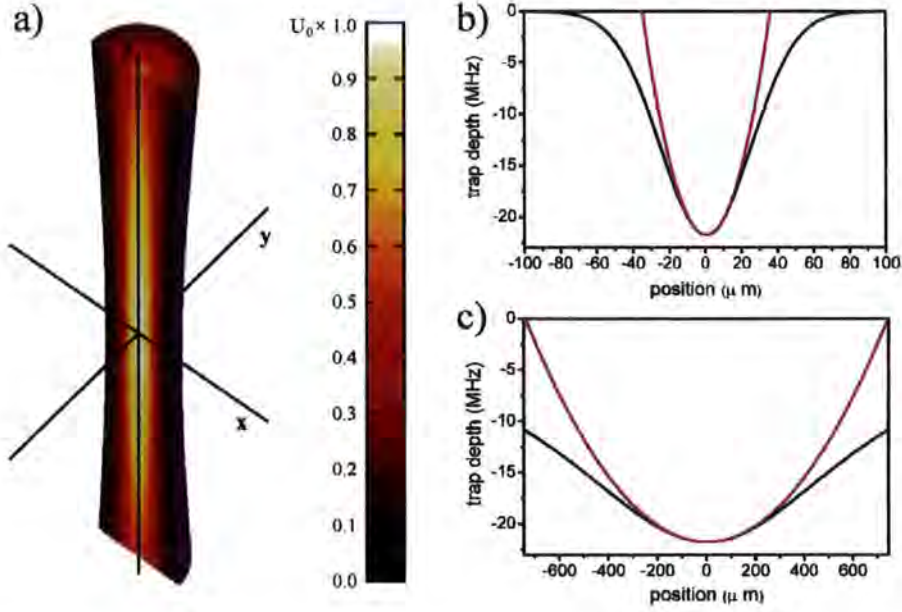


Figure 3.2: Single Gaussian beam a) 3D intensity plot with slice through the $y=0$ plane b) trap depth in the radial direction at the beam focus and c) trap depth in the axial direction over two Rayleigh ranges - based on estimated laser parameters shown in table 3.1. The red lines are harmonic fits to the potential.

$$U = U_0 \frac{\exp[-2r^2/w(z)^2]}{1 + (z/z_R)^2} \quad (3.3)$$

The bottom of the trap can be considered to be parabolic and so, by using the Maclaurin series for the exponential the trap frequencies ω_r and ω_z for a single beam trap can be calculated by simply taking the harmonic term from an expansion of equation 3.3 and comparing with the energy of a particle in a harmonic oscillator potential. Doing this we get

$$\begin{aligned}\frac{2r^2U_0}{w_0^2} &= \frac{1}{2}mr^2\omega_r^2 \\ \Rightarrow \omega_r &= \sqrt{\frac{4U_0}{mw_0^2}}.\end{aligned}\tag{3.4}$$

This approach was adopted by Friebe *et al* [42] to calculate the trap frequencies of a 1D CO₂ laser optical lattice. A plot of the harmonic fit to the radial potential is shown as the red line in figure 3.2 b). The width of the beam changes as $w(z) = w_0\sqrt{1 + (z/z_R)^2}$ and so the intensity profile is Lorentzian along z . By taking the Maclaurin series for a Lorentzian and considering the harmonic term in z gives,

$$\begin{aligned}\frac{U_0}{z_R} &= \frac{1}{2}mz^2\omega_z^2 \\ \Rightarrow \omega_z &= \sqrt{\frac{2U_0}{mz_R^2}}.\end{aligned}\tag{3.5}$$

A plot of the harmonic fit to the potential along the z axis is shown as the red line in figure 3.2 c). The confinement is much weaker in this direction than the radial direction since the gradient of the potential is small. The vast majority of single beam dipole trap experiments are aligned horizontally as the confinement along the z direction is usually so weak it will not support the atoms against gravity. The calculated parameters for the single beam trap are shown in table 3.1.

It is interesting to note that the Lamb-Dicke regime is not reached for the single beam trap. Calculating the Lamb-Dicke parameter, η [106], for the D1 transition ($\lambda=795\text{nm}$) $\eta = \sqrt{\pi\hbar/\lambda^2m\omega_{\text{osc}}}$, where ω_{osc} is the oscillation frequency, we find $\eta_r = 3.4$ and $\eta_z = 15.5$ and so cooling to the ground vibrational state by Raman sideband cooling [107] is not possible.

3.4 1D lattice

After achieving a single beam dipole trap the next proposed stage of the experiment is to form a 1D lattice. Given the geometry of the vacuum

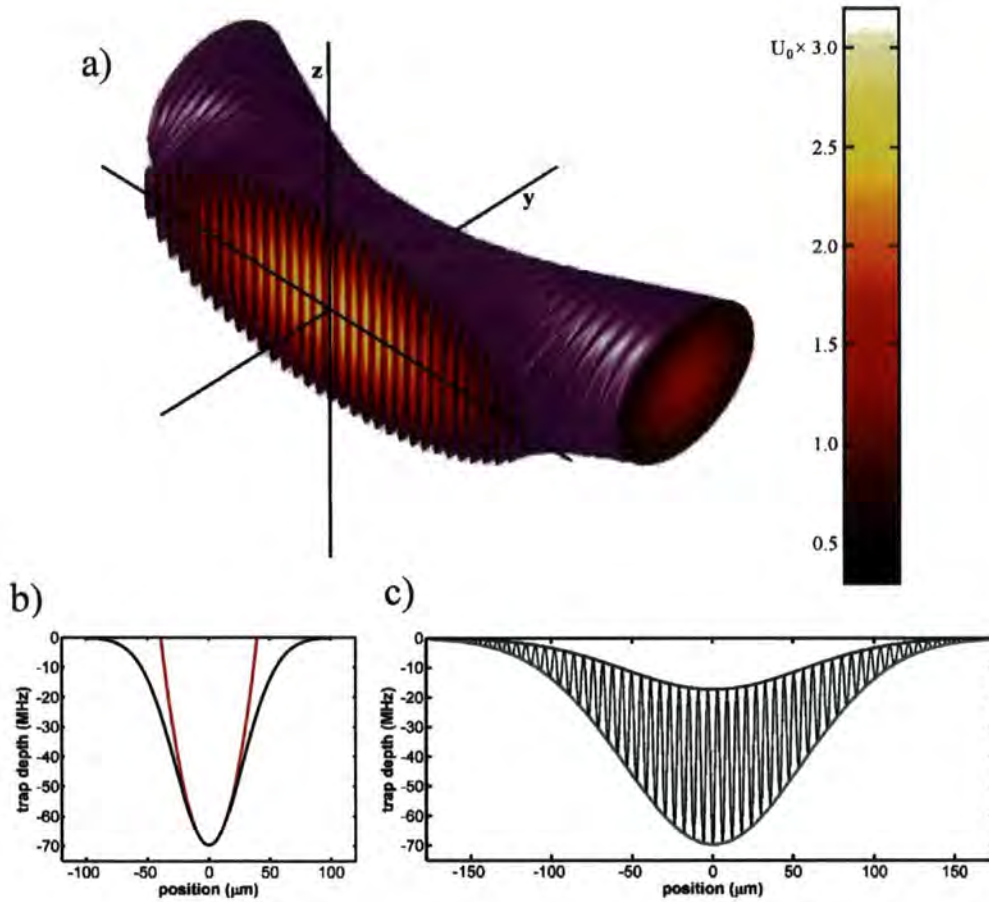


Figure 3.3: Two Gaussian beams crossing at $\arcsin(4/5)$ a) 3D intensity plot with slice through the $y=0$ plane b) trap depth in the y and z directions at the focus c) trap depth along the x direction in the region where the beams overlap

P (W)	w_0 (μm)	I_0 (mW/cm^2)	z_R (μm)	U_0 (MHz)	ω_r (kHz)	ω_z (Hz)
60	50	1.53×10^9	741	$(2\pi)21.76$	$(2\pi)2.03$	$(2\pi)96.8$

Table 3.1: Single beam laser trap parameters

chamber (see chapter 4), this can be achieved by either retro-reflecting the input beam or by applying a second beam at an angle of $\arcsin(4/5)$ to the input beam as shown in figure 3.3 a). This second case is the scheme we will consider for two reasons. Firstly, a retro-reflected beam would propagate back along the beam path and cause undesirable heating of optical elements [108] and possibly feedback into the laser, secondly; the crossed 1D lattice is a step towards the 3D lattice discussed in the next section. For equal intensity horizontally polarized beams, the maximum trap depth of the crossed lattice is 3.2 times the trap depth of the single beam due to the interference between the crossing beams and the angle between the polarisation of the beams (For a retro-reflected 1D lattice the maximum trap depth would be four times the single beam trap depth). The period of this crossed lattice $\lambda' \equiv \lambda/2 \sec(\theta/2) = 5.93 \mu\text{m}$, where $\lambda = 10.6 \mu\text{m}$ and θ is the angle between the beams.

Figure 3.3 a) shows the geometry of the 1D lattice in the laboratory frame. Although the y and z profile of the interfering beams are no longer exactly Gaussian, they can still be modeled with great accuracy as a Gaussian of depth $3.2U_0$ and a width of $w_0 \sec(\theta/2)$. Figure 3.3 b) shows a line profile of the trap depth along the y and z axes. The red line shows a harmonic fit to the Gaussian calculated in the same way as described for the single beam trap of section 3.3.

Along the x axis, the spatial variation of the trap depth can be accurately modeled by a \cos^2 function contained between two Gaussian envelopes (the green and blue lines in figure 3.3 c). The equation

$$U(x) = \frac{3}{4} \cdot 3.2 \cdot U_0 \cos^2\left(\frac{\pi x}{\lambda'}\right) \exp\left[\frac{-2x^2}{w^2}\right] + \frac{1}{4} \cdot 3.2 \cdot U_0 \exp\left[\frac{-2x^2}{w^2}\right] \quad (3.6)$$

describes the spatial variation of the trap depth to within 1.5% over the central 31 lattice sites (as compared to the numerically calculated values).

Figure 3.4 shows how the trap frequencies of the lattice sites vary as we move away from the trap centre.

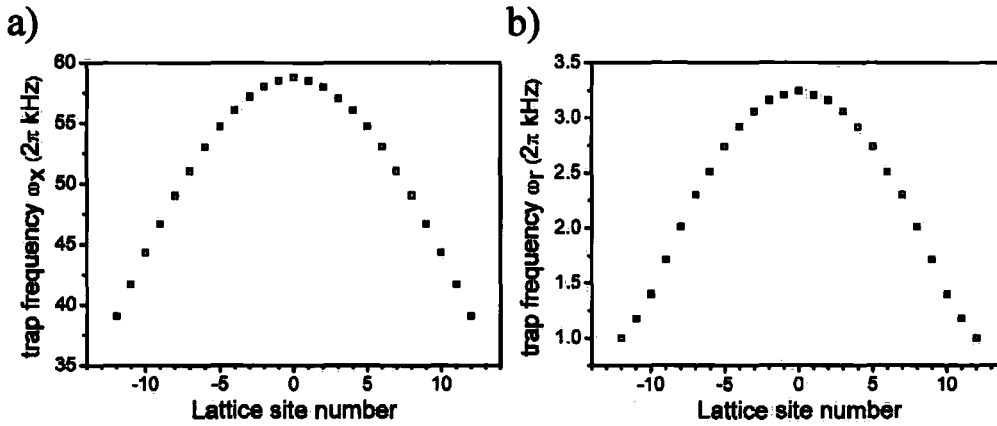


Figure 3.4: Calculated axial trap frequencies a) ω_x and b) ω_r for the 25 central lattice sites

Figure 3.5 shows the radial trapping potential for lattice sites 0-12 of the 1D lattice. We define site 0 as the central, deepest site with sites ± 1 on either side. The beams cross and overlap at the foci but as the beams diverge, the harmonic fit becomes inadequate. Indeed the 12th site is the last with a single minimum as the two spots become resolved.

It is interesting to note that the Lamb-Dicke regime is reached in the x direction ($\eta_x = 0.63$) but not in the y and z directions ($\eta_{y,z} = 2.68$). It is possible that Raman sideband cooling could be achieved along the x axis [107, 109]

P (W)	w_0 (μm)	I_0 (mW/cm^2)	z_R (μm)	U_0 (MHz)	$\omega_{y,z}$ (kHz)	ω_x (kHz)
60	50	4.90×10^9	741	$(2\pi)69.64$	$(2\pi)3.23$	$(2\pi)58.80$

Table 3.2: 1D lattice trap parameters

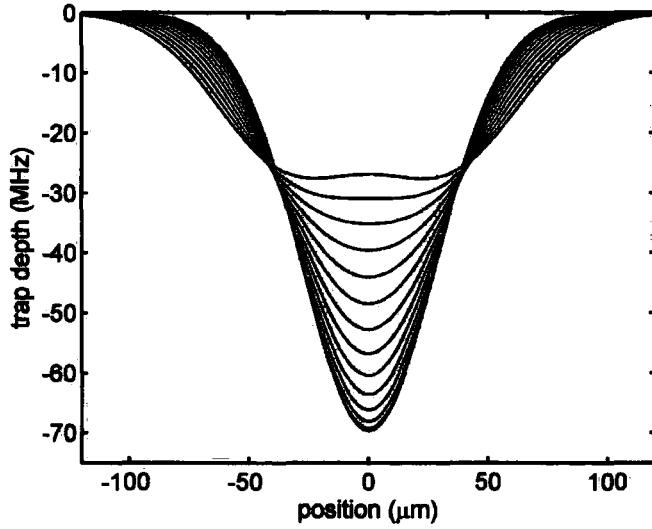


Figure 3.5: Radial potential of the 1D lattice for 13 lattice sites

3.5 3D Lattice

An obvious extension to this work is to extend the trapping geometry into more dimensions. If another crossed 1D lattice (as described in the previous section) is added and rotated 90° about the y axis, (ie. four beams now arranged with two beams in the vertical $y-z$ plane at θ to the y axis, and two beams in the horizontal $x-y$ plane at θ to the y axis) the resulting structure is a 3D face-centered cubic lattice with a lattice constant of $\lambda/2\sin(\theta)$. In our case θ is $\arctan(2)$. The structure of the lattice is discussed in detail in reference [110]. The maximum trap depth is 12.8 times the single beam trap depth and the barriers between adjacent sites are 31% of the maximum depth. Figure 3.6 a) shows a 3D intensity plot. Figures 3.6 b) and c) show the trap depth along the x (and z) axis and y axis respectively. The x (and z) axis is more tightly bound than the y axis.

The 3D lattice has relatively high trap frequencies for sites in the centre region. The frequencies decrease rapidly as we move away from the centre. In figure 3.7 the red lines show a harmonic fit to the trapping potential for the central lattice site along the x (or z) and y axes. The calculated parameters for this 3D lattice are shown in Table 3.3. $\bar{\omega} = (\omega_x\omega_y\omega_z)^{1/3}$ is the geometric

mean of the trap frequencies.

P (W)	w_0 (μm)	I_0 (mW/cm^2)	U_0 (MHz)	$\omega_{x,z}$ (kHz)	ω_y (kHz)	$\bar{\omega}$ (kHz)
60	50	1.96×10^{10}	278.6	$(2\pi)89.7$	$(2\pi)67.8$	$(2\pi)81.7$

Table 3.3: 3D lattice trap parameters

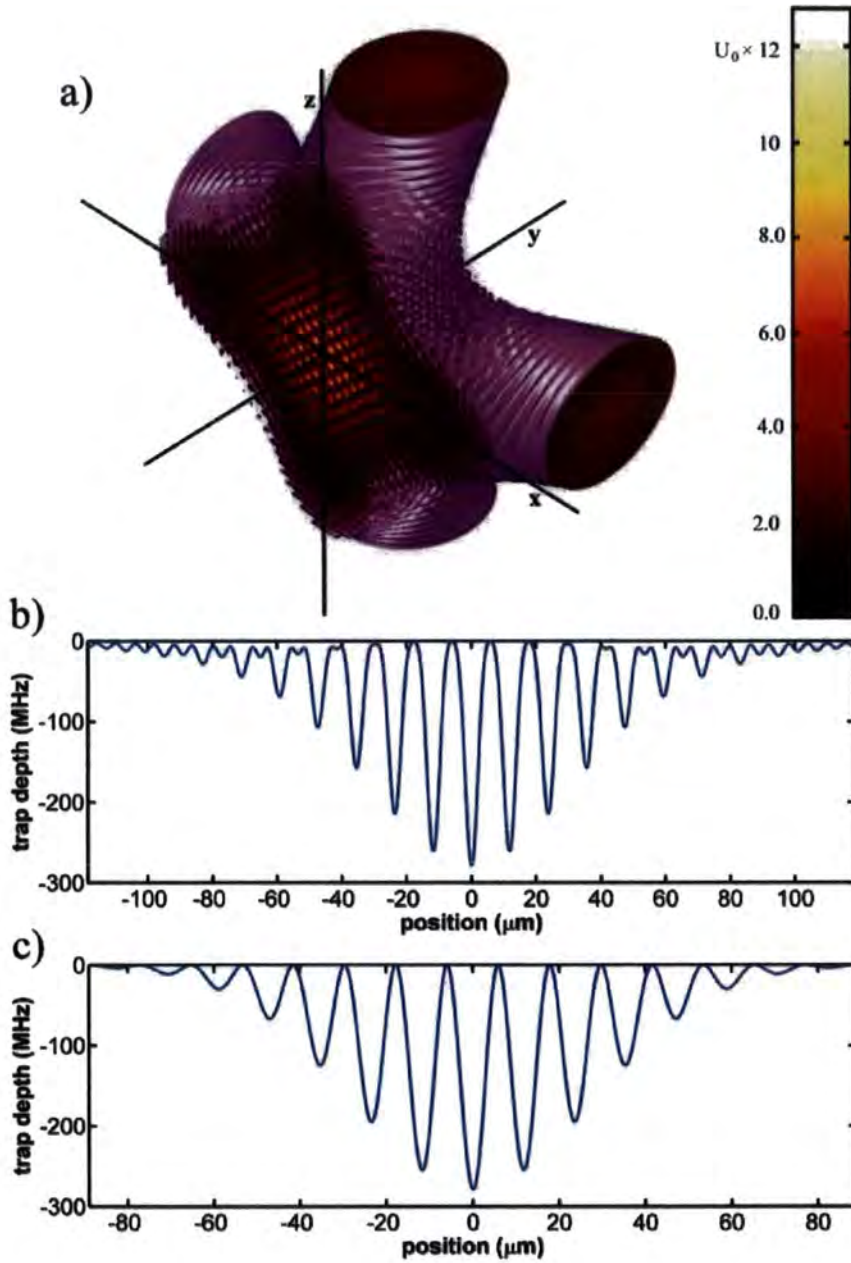


Figure 3.6: 3D lattice formed from four laser beams a) 3D intensity plot with slice through the $y=0$ plane b) Trap depth along the x (and z) axis. c) Trap depth along the y-axis

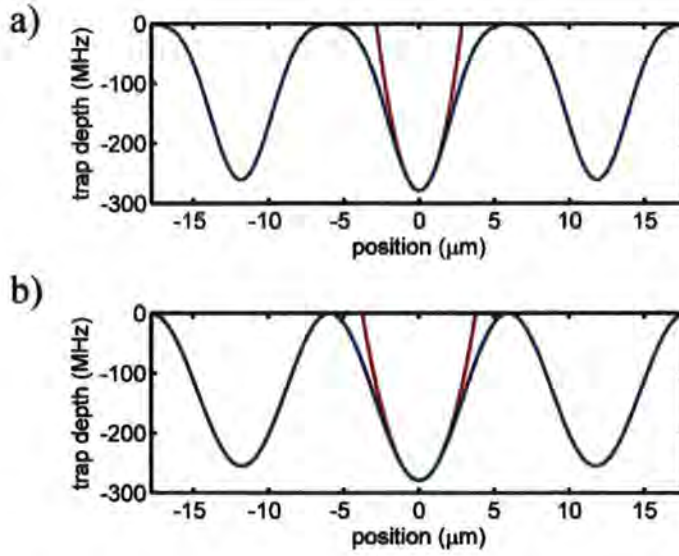


Figure 3.7: Optical potential for the 3D lattice potential along a) the x (and z) axis b) the y-axis. The confining potential is weakest along the y-axis. The red curves represent a harmonic fit to the bottom of the well.

3.6 High T_c BEC

If the high trap frequencies for the 3D lattice predicted in the previous section and shown in table 3.3 can be realized in practice then to the author's knowledge, this experiment would have the highest reported average oscillation frequency for a large volume ($V > (1 \mu\text{m}^3)$) neutral atom trap. An interesting consequence of a very high trap frequency is the increase of the critical temperature at which BEC is formed. The critical temperature T_c is defined by [111]

$$\zeta(3) \left(\frac{k_B T_c}{\hbar \bar{\omega}} \right)^3 = N, \quad (3.7)$$

where N is the number of atoms $\zeta(3) = 1.202$.

For the 3D lattice modeled in the previous section, if we estimate that we can obtain fifty atoms per lattice site (assuming a MOT density of 10^{11} atoms/cm³) then the critical temperature is around 2 μK . This temperature

is almost achievable by direct laser cooling and could in principle allow the creation of BEC without forced evaporative cooling.

Part II

The Experiment

In the following four chapters we detail the design, construction and execution of the laser cooling experiment. We start with a discussion of the vacuum chamber, which contains some unique and note-worthy features. Following that, we describe the optical setup used to laser cool Rb atoms including the design and development work on diode lasers. Next we described some of the infrastructure needed to ensure a safe and reliable experiment, describe the general running of the laser-cooling setup and present the results obtained. Finally we discuss the CO₂ laser and how it is aligned and detail the methods used to try to find the dipole-trap signal.

Chapter 4

The Vacuum Chamber

4.1 Introduction

Like most cold atom experiments this work had to be conducted under Ultra-High Vacuum (UHV) conditions and hence required a vacuum chamber. During previous work [49–51, 112] we measured a vacuum limited CO₂ trap lifetime of approximately 5 s. This lifetime was limited by the Rb vapour pressure in the region of the dipole trap. To improve on this lifetime for this experiment, we decided to use a double vacuum chamber design to separate the high pressure ($\sim 10^{-8}$ Torr) Rb vapour from the CO₂ laser trap. Atoms would be pre-cooled in a *pyramidal* MOT (described in section 4.3) and transferred to a second chamber containing a second MOT with overlapped CO₂ laser trap. To aid clarity, from this point on, we will refer to the chambers containing the pyramid MOT and the CO₂ laser trap as the ‘pyramid’ chamber and ‘science’ chamber respectively. The design and development of the vacuum chamber was challenging and complex, and accounts for a large proportion of the time taken to complete this thesis.

4.2 The Science Chamber

Given the unusual configuration of laser beams needed to make the CO₂ laser lattice described in section 3.5, a standard commercial vacuum chamber could not be used. Hence, it was decided that the main UHV chamber should be

machined from a single piece of stainless steel with added viewports to allow optical access. Before the chamber could be manufactured we had to conceive a design that would accommodate the following criteria:

- Eight viewports for the configuration of laser beams required for the 3D CO₂ laser lattice discussed in section 3.5.
- Six viewports for the MOT beam configuration discussed in section 2.2.3.
- Optical access for the imaging and manipulation of atoms within the lattice
- Access for the Rb to enter the chamber.
- Access for the vacuum pumps and roughing pumps

The chamber was initially designed for a proposed collaboration between Durham University and the University of Strathclyde to laser cool calcium atoms and trap them in a 3D CO₂ laser lattice [110]. The project was re-evaluated and the decision was made to conduct similar experiments on rubidium in Durham with the work on calcium proceeding at Strathclyde.

As stated earlier, it was decided that the second MOT should be loaded with pre-cooled atoms from a pyramidal MOT contained in a separate vacuum chamber, even though loading the MOT directly from a thermal vapour would allow a much simpler experimental setup. This approach was motivated by the long term goals of the project set out in section 1.4.3, which require long coherence times. Hence, the added bulk and complication of connecting together two vacuum chamber was undertaken in the interests of improving the vacuum in the science chamber

To check the geometry of the chamber and to ensure the compatibility of the chamber design with the other required ConFlat® vacuum components, a 3 dimensional computer model of the chamber was drawn to scale using AutoCAD 2000 software. Plan and elevation views of the chamber model can be seen in figure 4.1. The axes in the figure match the orientation of those used to model the optical lattice in chapter 3. 3D modeling of the

chamber proved invaluable as it allowed further aspects of the experiment to be developed without fear of intersecting equipment.

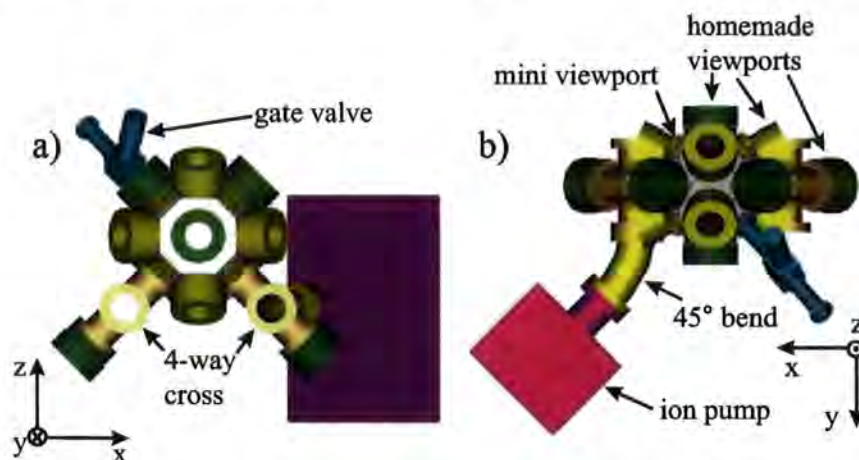


Figure 4.1: 3D model of the science chamber in a) elevation and b) plan view. The coordinate axes shown match the laboratory coordinates used to model the optical lattices in chapter 3 with the point $x = y = z = 0$ at the centre of the chamber.

Once the design was finalised for the science chamber, construction began at the University of Strathclyde in February 2004. A cylindrical billet of LN304 non-magnetic stainless steel was purchased and machined by the technician Robert Wiley. Figure 4.2 shows the chamber partially completed. Once finished the chamber was sent to Poligrat Ltd. for electro-polishing before arriving at Durham University in August 2004.

4.3 The Pyramid Chamber

4.3.1 Introduction

In the time during which the science chamber was manufactured, work commenced on the source of cold atoms. A pyramidal MOT is a useful way of producing a cold atomic beam from a thermal vapour. In this experiment, the use of a pyramid MOT would allow the science chamber to remain at low pressure whilst still collecting many atoms in the second MOT. This scheme



Figure 4.2: Science chamber partially made.

was chosen as the first stage of laser cooling above other methods such as a second MOT with push beam [113], the LVIS [114] and Zeeman slower [115] and the 2D MOT (or atomic funnel) [116–118] because pyramidal MOT technology was already in use within the Durham Atomic physics group. This existing apparatus was duplicated for inclusion in our setup.

4.3.2 Pyramidal MOT

The light-field configuration used in a conventional six-beam MOT described in section 2.2.3 can be achieved using a single laser beam in a pyramidal MOT [119]. The pyramidal MOT is realized by two mirrors and two prisms which form a 90° inverted pyramid that is truncated just before the apex leaving a 1×2 mm hole for the cold atom beam to exit through, see figure 4.3.

The pyramidal MOT optics were made from BK7 glass substrate with a broadband dielectric coating applied at Oxford university. The mirrors have approximately equal reflectivities for s- and p-polarised light and induce similar phase shifts for the two polarisations. The same coating was used in other work [120] and the measured difference in reflectivity for the s- and p-polarisations were found to be $<1\%$. Less than 4% of the light was found to be of the wrong handedness of circular polarisation after reflection from one mir-

ror.

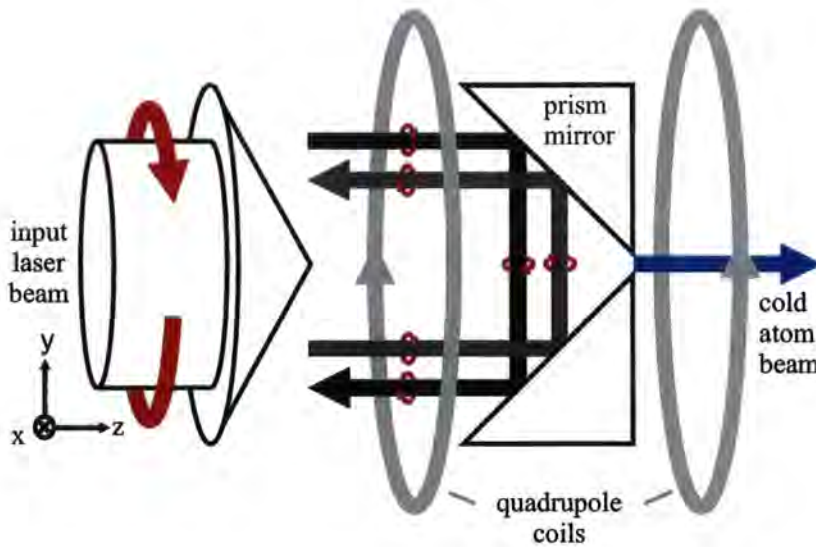


Figure 4.3: Polarization configuration in a pyramid MOT, dark lines indicate portions of the incident circularly polarized laser beam and its reflections. The helicities are indicated by small red arrows.

4.3.3 Pyramid Chamber Construction

The pyramidal MOT requires a separate vacuum chamber which was designed at Oxford university by D. Cassettari and manufactured by Thermo Vacuum Generators. This chamber consists of a DN100 conflat BK7 viewort, the pyramidal MOT optics, rubidium metal dispensers, an exit hole for the cold atom beam, feed-throughs for the electrical connections and an all metal valve. Also connected to the chamber was a Varian Starcell ion pump (40 l/s). Preparation of the vacuum components, construction and bakeout of the chamber was similar to that described later for the science chamber in section 4.4.

The alkali metal dispensers were spot-welded to stainless steel wires which were then connected to the electrical feed-through. Caesium and Rubidium dispensers were added so that the experiment was as versatile as possible. Figure 4.4 shows a photograph of the pyramidal MOT optics and alkali dis-

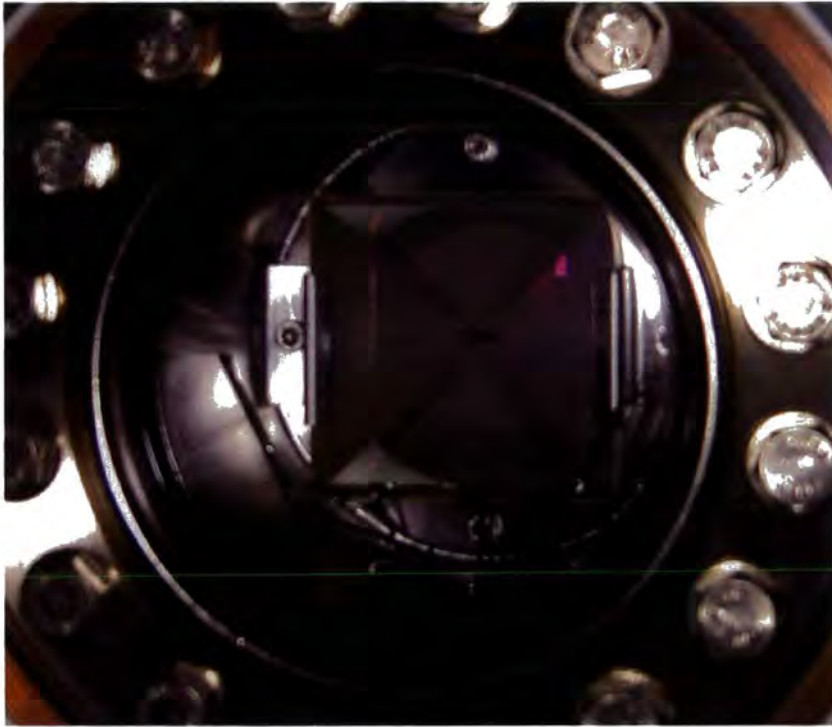


Figure 4.4: The pyramid MOT optics and alkali dispensers within the pyramid chamber viewed through a DN100 conflat viewport. The escape hole for the atomic beam can be seen at the apex of the inverted pyramid.

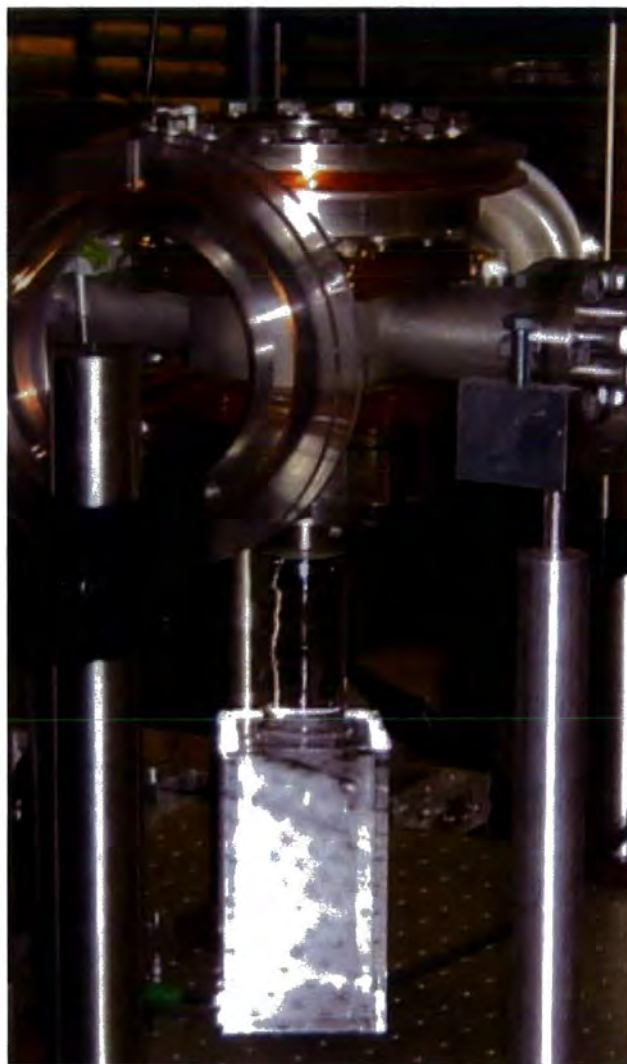


Figure 4.5: Pyramid MOT chamber in the test phase, mounted vertically and used to test the laser cooling apparatus.

penser setup. Quadrupole coils were wound directly onto the exterior of the vacuum chamber by turning the chamber in a lathe. Each turn was secured in place with epoxy resin. There were twenty turns on each coil giving a field gradient of ~ 0.7 G/cm per Amp. Due to a manufacturing mistake of the pyramid chamber, the field zero was approximately 1.2 mm away from its desired place at the centre of the pyramid optics. During the test phase of the pyramidal MOT, the chamber was connected to a quartz cell and mounted vertically such that the cold atom beam was fired downwards into the cell. These tests helped us to develop the laser cooling setup detailed in chapter 5. A photograph of the initial set-up of the pyramidal MOT chamber is shown in figure 4.5. Detailed study of the cold atom source was not conducted at this point since laboratory conditions (especially magnetic field) would be vastly different in the final setup due to the close proximity of a second MOT. The functional pyramid chamber awaited a completed science chamber to connect to.

4.4 Assembly and Bake-out

The completed double vacuum system was constructed in two main stages. First the science chamber was constructed and pumped out and then the pyramid chamber appended to it. This section describes how this was achieved starting with the cleaning of vacuum components and the manufacture of home-made UHV viewports. Details of vacuum components and techniques used in the following sections can be found in reference [121].

4.4.1 Cleaning Vacuum Components

Most of the components and tools used in the construction of the vacuum system had to be cleaned beforehand. Latex gloves were worn throughout to eliminate the possibility of stray fingerprints inside the chamber. Typically the cleaning procedure progressed as follows:

- The items were cleaned for 30 minutes in a 5% solution of decon90 in an ultrasonic cleaner.

- After draining, residual decon90 was removed by rinsing in tap water for 10 minutes.
- The items were then cleaned with distilled water in an ultrasonic cleaner for a further 60 minutes
- A heat gun was used to remove water from the components and then the components were wrapped in foil until ready for use.

Once all of the tools and vacuum components were clean the assembly of the chamber could begin.

4.4.2 Re-Useable UHV Viewports

A problem for many researchers using CO₂ lasers is the prohibitively high price of suitable optical components. Most common optical materials, such as quartz or BK7, strongly absorb far-infrared radiation and are unsuitable for use with CO₂ lasers. Zinc Selenide (ZnSe) transmits at 10.6 μm and is usually used instead. The 3D lattice configuration discussed in section 3.5 requires four laser beams to enter and then leave the science chamber. This scheme requires eight UHV ZnSe viewports to allow passage of the beams. We saved many thousands of pounds by developing and manufacturing our own UHV viewport technology. These home-made viewports have the added advantage of improved optical flatness and parallelism over most commercial products. The viewports used on the science chamber were modified versions of viewports used previously at Durham and described in reference [122]. Anti-reflection (AR) coated ZnSe was sandwiched between pre-flattened flux-free solder. The modified design used on this work incorporates an extra flange to decouple the solder seal from the conflat flange which is bolted to the vacuum system. This arrangement avoids stresses on the conflat flange upon tightening and allows the viewport to be re-used without developing leaks. Figure 4.6 shows a plan view and two cross-sectional views of the modified viewport. The viewport is constructed by mounting an optical element on a double flange, in this case made from a “cut down” tubulated conflat flange with an additional flange for mounting the optic welded in place. This design allows the copper gasket seal of the Conflat flange to be

made without applying stress to the solder seal surfaces. The materials and processes of the solder sealing procedure are the same as reported in reference [122].

During early attempts at viewport manufacture we found that the solder seal was less dependable when using an AR coating on harder substrates (i.e. BK7). For this reason, a coating-free edge was requested around the optic on which to make the seal. No such problems were encountered with the softer AR coated ZnSe optics. A further refinement to the design by Cox *et al.* [122] is the use of different bolts for the solder and conflat seals to eliminate accidental over-tightening of the solder seals. This design was repeatedly tested using BK7 and ZnSe optical elements. A photograph of a completed ZnSe viewport is shown in figure 4.7. During tests the viewports were re-attached and baked six times up to 250°C without affecting the UHV viewport seal. Helium leak testing was performed and no leaks were detected down to partial pressures of 10^{-14} level. Once the six BK7 viewports and eight ZnSe viewports were completed and all other vacuum components purchased, the science chamber was ready for construction. A publication detailing this new viewport design is in preparation.

4.4.3 Science Chamber Assembly

The construction of the science chamber proceeded as follows. Two four-way crossed DN40 conflat connectors were bolted to the chamber (see figure 4.1). The cross pieces of these connectors were then fixed into cradles such that the whole assembly was supported by them. To the three spare flanges of one cross connector was fastened a BK7 homemade viewport for a MOT beam, an ion gauge head and an all-metal valve. Attached to the other crossed connector was a Varian Starcell (40 l/s) ion pump (attached via a 45° connector to allow better optical access to the chamber, see figure 4.1), and a SAES getters CapaciTorr (MK5 series) non-evaporative getter (NEG) pump and a BK7 MOT viewport. Following this, eight home-made ZnSe viewports, four more home-made BK7 viewports, six AR coated commercial mini-conflat viewports, a mini-conflat blanking flange and a mini conflat straight connector (capped with a gate valve to seal the other end) were

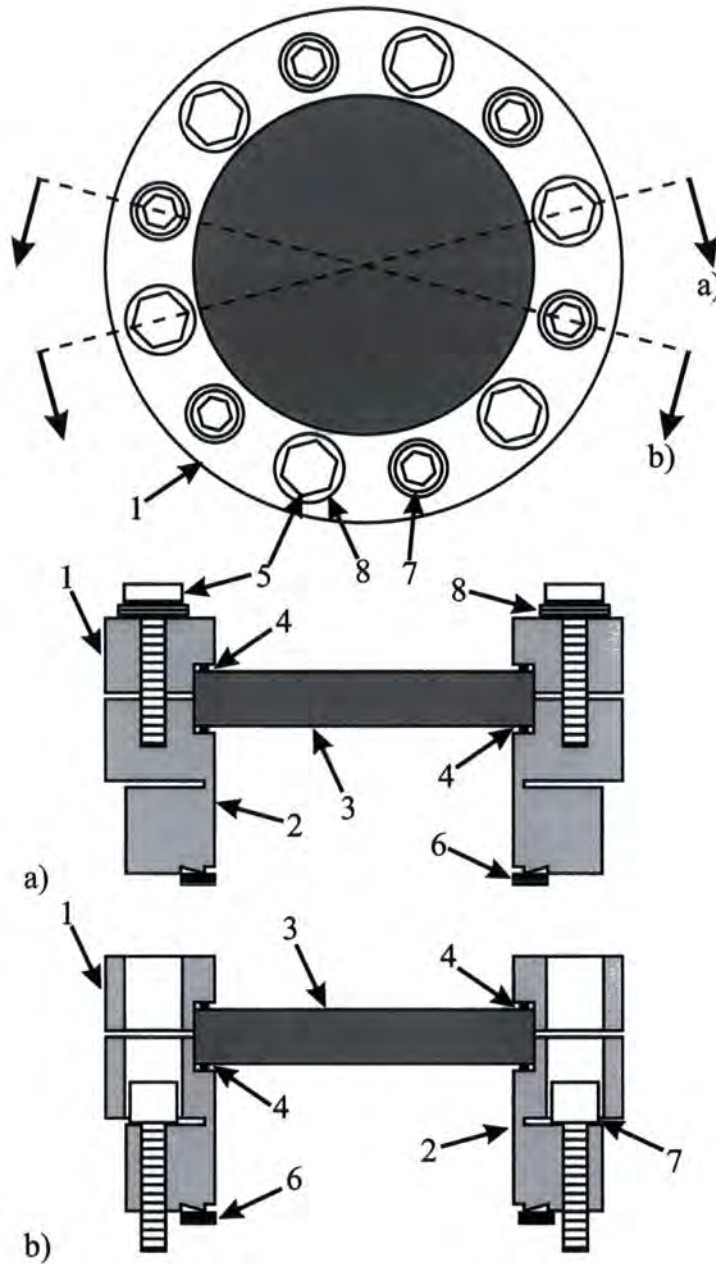


Figure 4.6: (Top) The viewport in plan view. (middle and lower parts) Different c/s views through the viewport, indicated by (a) and (b). 1: clamping flange, 2: tubulated flange with welded attachment 3: optical component, 4: indium based solder, 5: M6 hex-head bolt, 6: copper gasket, 7: M6 cap-head bolt.



Figure 4.7: Photograph of a home-made vacuum viewport containing a ZnSe window.

bolted directly to the science chamber.

4.4.4 Bake-out

The completed assembly was transferred to an oven (details of the oven can be found in Griffin's thesis [51]) and pumped out through the all-metal valve using a Pfeiffer TMU065 (56 l/s) turbo pump backed by a Pfeiffer PKD41702 (2.5 m³/h) rotary vane pump. A pressure of around 8×10^{-8} Torr was reached after 24 hours. At this point the ion pump and NEG pump were activated causing the pressure to increase by two orders of magnitude. The pressure was allowed to recover before the oven was sealed and the chamber baked at 220°C for around two weeks. Once cooled to room temperature, the pressure in the chamber reached 3×10^{-10} Torr. At this point the all-metal valve was closed and pumping provided only by the ion pump and NEG pump.

4.4.5 Joining of the Vacuum Chambers

The science chamber assembly along with its supporting cradles were transferred to a large (60×90 cm) breadboard. The pyramid chamber was mounted on the same breadboard using an angled column at 39° to the horizontal. It was then attached to the gate valve of the science chamber such that the central axis passing through the pyramid optics was aligned with the centre of the science chamber. A flexible mini-conflat connector was used to make this connection to avoid any shearing forces caused by slight misalignment of the chambers. Once joined, the pyramid chamber was pumped out through the all-metal valve and then the ion pump was activated. Baking was achieved by wrapping heater tape around the chamber and then wrapping it in foil to try to make the temperature as even as possible throughout. The chamber was baked in this way for five days before it was allowed to cool. The all-metal valve of the pyramid chamber was sealed before the gate valve between the chambers was then opened, clearing passage between the pyramid chamber and the science chamber. Shortly after the joining process, the ion gauge in the science chamber began to display erroneous readings (10^{-15} Torr) and was henceforth ignored, meaning no reliable pressure measurements could be taken.

Figures 4.8 and 4.9 show photographs of the completed double vacuum chamber viewed from opposite sides. Figures 4.10 and 4.11 show schematics of the double vacuum system in plan and elevation view respectively. All important features are labeled. The laser beams shown in red (labeled σ^+ and σ^-) are beams to be used for the creation of the MOTs. Details of how the appropriate beams were prepared is the subject of the following chapter. The laser beams shown in purple are the CO₂ laser beams. A discussion of the CO₂ laser beam path can be found in chapter 7. The chamber was moved to the laboratory and placed upon the optical table from which point the rest of the experiment was built up around it.

4.5 Summary of the Vacuum Chamber

To summarise, the vacuum system consists of two conjoined chambers.

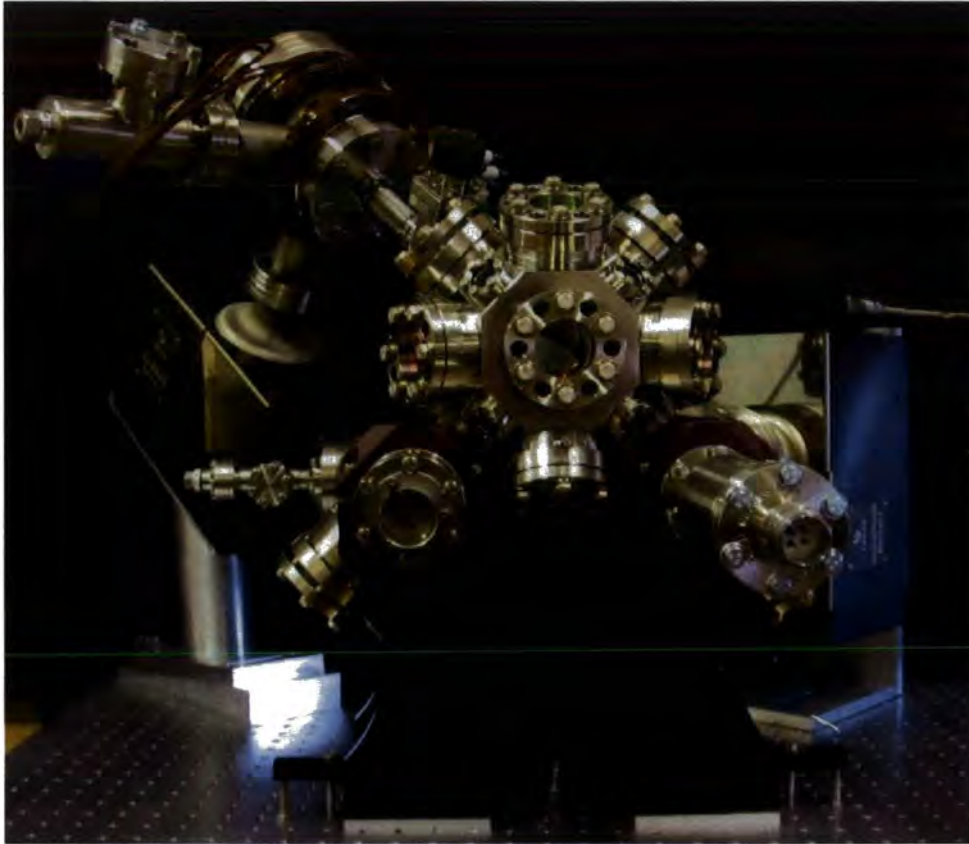


Figure 4.8: Completed vacuum chamber viewed from the front. The ion gauge head (left) and CapaciTorr pump (right) can be seen in the foreground). The cradle clamps are machined to allow access to the lower mini-conflat viewports.

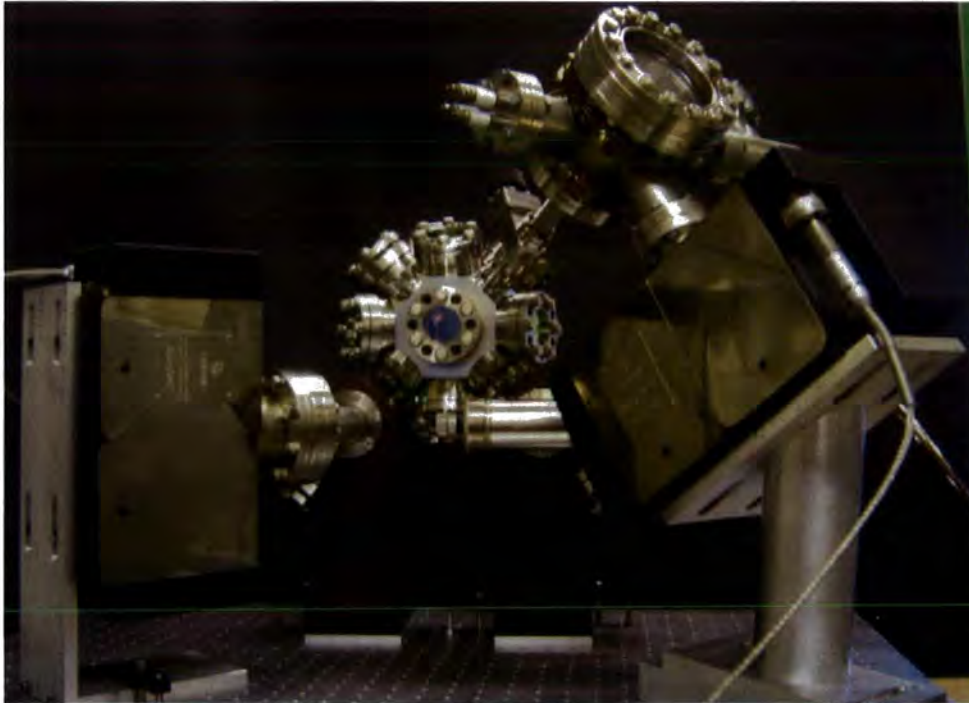


Figure 4.9: Completed vacuum chamber viewed from the back. The upper pyramid chamber is connected to the lower science chamber by a DN16 flexible connector. The pyramid and science MOTs are separated by approximately 23 cm. The large black and silver boxes in the foreground are the ion pumps.

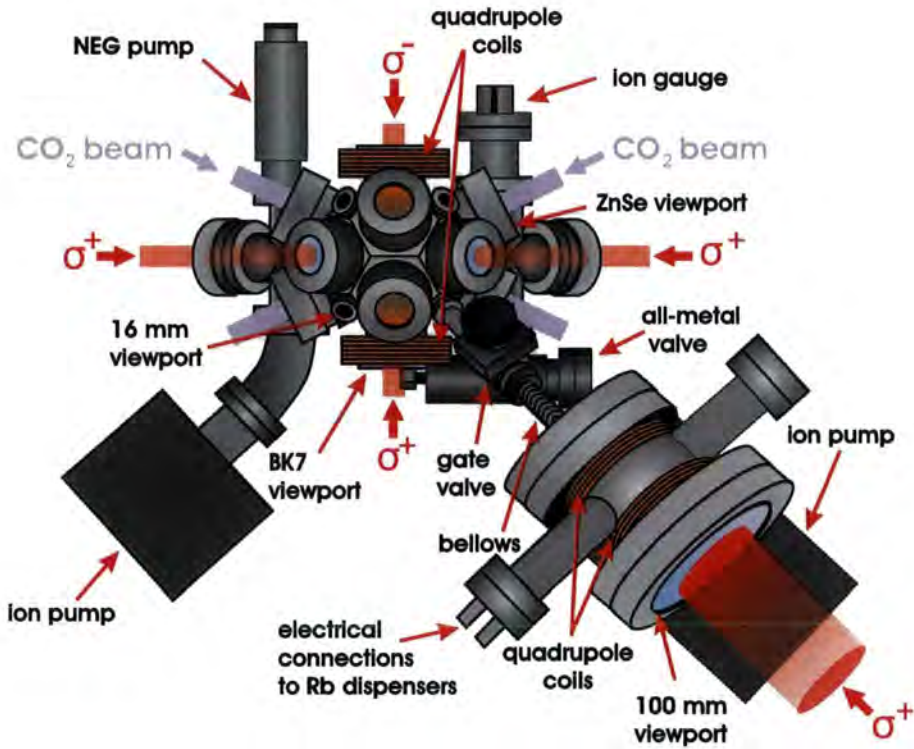


Figure 4.10: Schematic of the double vacuum chamber as viewed from above. All relevant vacuum components are highlighted. Laser beams for the MOTs are shown in red (labeled σ^\pm) and CO₂ laser trap beams in purple. The quadrupole coils shown on the science chamber are discussed in chapter 6.



Figure 4.11: Schematic of the double vacuum chamber as viewed from above. All relevant vacuum components are highlighted. Laser beams for the MOTs are shown in red (labeled σ^\pm) and CO₂ laser trap beams in purple. The quadrupole coils shown on the science chamber are discussed in chapter 6.

- The pyramid chamber with: an all-metal valve for ‘roughing’, an ion pump to maintain vacuum, a single large viewport for optical access, an electrical feedthrough connected to alkali metal dispensers, an inverted pyramidal mirror truncated close to the vertex (creating a small hole for the atoms to escape), and a flexible DN16 connector through which the cold atom beam can leave the chamber.

and

- The science chamber with: two four-way cross connectors, an all-metal valve for ‘roughing’, an ion pump (mounted on a 45° bend) to maintain vacuum, a NEG pump to help pump H₂ and H₂O, an ion gauge head for pressure measurements, eight home-made ZnSe viewports, six home-made BK7 viewports, six commercial BK7 mini-viewports, a mini-conflat blanking flange and a mini-conflat straight connector ending in a gate valve (the other side of which was connected to the pyramid chamber).

The Pyramid chamber was mounted above the science chamber at an angle of 39° to the horizontal and an angle of 45° to the x -axis (see figure 4.1). The distance between the centre of the two chambers (and hence the two MOTs) is approximately 23 cm.

Chapter 5

Laser Stabilisation and Optical Setup

To laser cool Rb the two types of laser typically used are the Ti:sapphire laser and the diode laser. Whilst the Ti:sapphire laser provides a lot of power (> 1 W) it is by far the more expensive option and so diode lasers are more commonly used. To achieve a robust and reliable laser cooling experimental setup it is beneficial to have stable lasers that do not require adjustment once their initial setup is complete. A general requirement is that the laser should have a linewidth smaller than that of the atomic resonance, Γ ($(2\pi)^{-1} 6$ MHz for Rb) and that the frequency can be stabilized to within a linewidth for the extended period of time necessary to perform experiments. These requirements are not typically met by a free-running diode laser. However, by creating an external cavity with a diffraction grating, the linewidth of the laser can be reduced drastically and the frequency tuned and controlled [123].

5.1 Introduction

The decision to use a double MOT system (discussed in the previous chapter) meant that the laser cooling setup used for this thesis was more complex than used for previous work [49–51, 112]. During the setup of this experiment, many different lasers, laser locking schemes, optical setups etc. were used before settling on a final setup. This chapter describes the final setup used

to collect the data discussed in chapter 6 and wherever appropriate, the evolution required to reach this stage.

5.2 Laser Development

In this work the laser cooling, magneto-optical trapping and imaging of the atoms was performed using (Sharp GH0781JA2C) diode lasers. Considerable effort was spent in developing suitable lasers for the experiment. Several iterations of laser design were implemented during the course of this work. In previous work conducted at Durham [124–126] the experiments were hindered to a certain degree by the limited time for which the lasers could be kept on transition. Although temperature stabilized, the lasers were protected only by a perspex cover and the passive frequency stability was poor (> 10 MHz/min). With this in mind, the early work on this thesis (year 1) was dedicated to replacing the older lasers by designing and building new high performance Littrow configuration extended cavity diode lasers [127, 128].

5.2.1 Double Boxed Mirror Mount Design

The first new design saw a replacement of the old homemade laser diode and collimating optic holder with a commercial collimating tube (Thorlabs LT230P-B). This tube was positioned within an aluminium mount which was temperature stabilized using a Wavelength Electronics MPT2500 controller. A plane holographic grating was mounted at 45° to the laser diode output beam upon two piezos (Thorlabs AE0203D04) which were in turn mounted upon a kinematic mirror mount (Thorlabs KS1). It was thought that using two piezos to allow simultaneous translational and rotational adjustment of the grating would improve the scanning range in comparison to translation or rotation alone. However, no appreciable improvement was observed. The laser and grating were mounted in a temperature stabilized box which was placed within another box. The laser beam exited the boxes through anti-reflection coated windows glued into position. A photograph of the laser with the lids removed is shown in figure 5.1. These new lasers were found to be much more stable than the previous design and were subsequently used

on the thesis work of Paul Griffin [51] and the work described in references [49, 50, 112]. Although much of the laser development work was qualitative in nature the benefits of using two levels of temperature stabilisation can be seen from measurements of the passive frequency drifts shown in figure 5.2. The drift was measured by recording a calibrated hyperfine spectrum [129] every fifteen minutes and comparing the location of the spectroscopic features. The observed long term trend of the frequency drift was always in the direction of negative frequency. No satisfactory explanation for this observation has been found.

This laser design has been adopted by other research groups and a variation

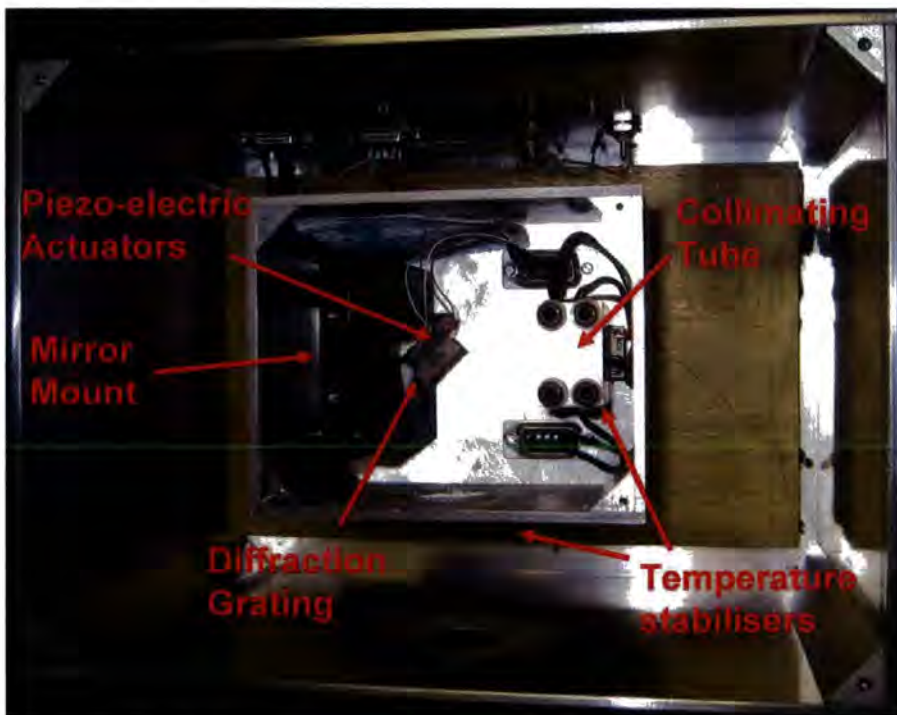


Figure 5.1: Diode laser with two isolating boxes. This laser was used for the thesis work of Griffin. The dimensions of the outer box are 17×23 cm

on the design was used for reference [130]. This style of laser performed well in terms of frequency stability, but the laser itself was bulky, required two separate temperature controllers and often developed runaway heating (or cooling) after power cuts, perhaps because the two coolers worked in

competition. For these reasons further design developments were made.

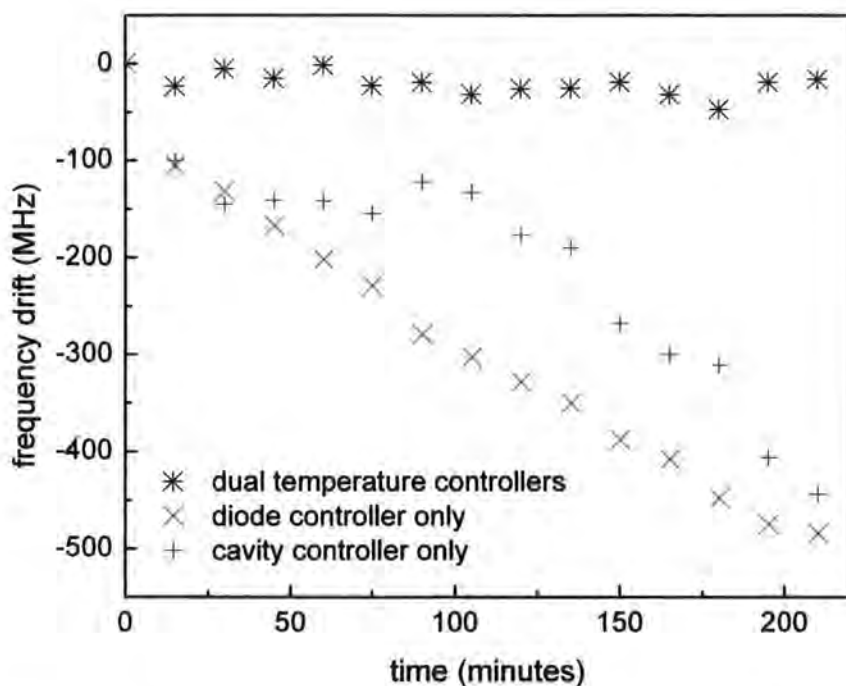


Figure 5.2: Measured frequency drifts of the ‘double box’ laser shown for each temperature controller separately and both together

5.2.2 Compact ‘O’ Ring Design

This later design was much smaller than its predecessor (with base dimensions 8×14 cm) and required only one temperature controller. However, the main alteration to the design was the way in which the diffraction grating was mounted. The alignment of lasers using commercial mirror mounts was found to drift slowly over time, resulting in the need for periodic re-alignment of the grating. We sought to overcome this inconvenience by developing a more rigid mount. The laser was housed on a solid block of aluminium which was temperature stabilized. An ‘O’ ring was sandwiched between a plate holding the piezos/grating and the main body of the laser. Fine adjustment screws were then tightened to squash the ‘O’ ring and still allow fine adjustment

of the angle of the plate. A photograph of the laser can be seen in figure 5.3. Again, this design performed well in terms of stability but was difficult to align so a third design incorporating features of the double boxed mirror mount design and the compact 'O' ring design was settled upon as the optimum laser for our experiments.

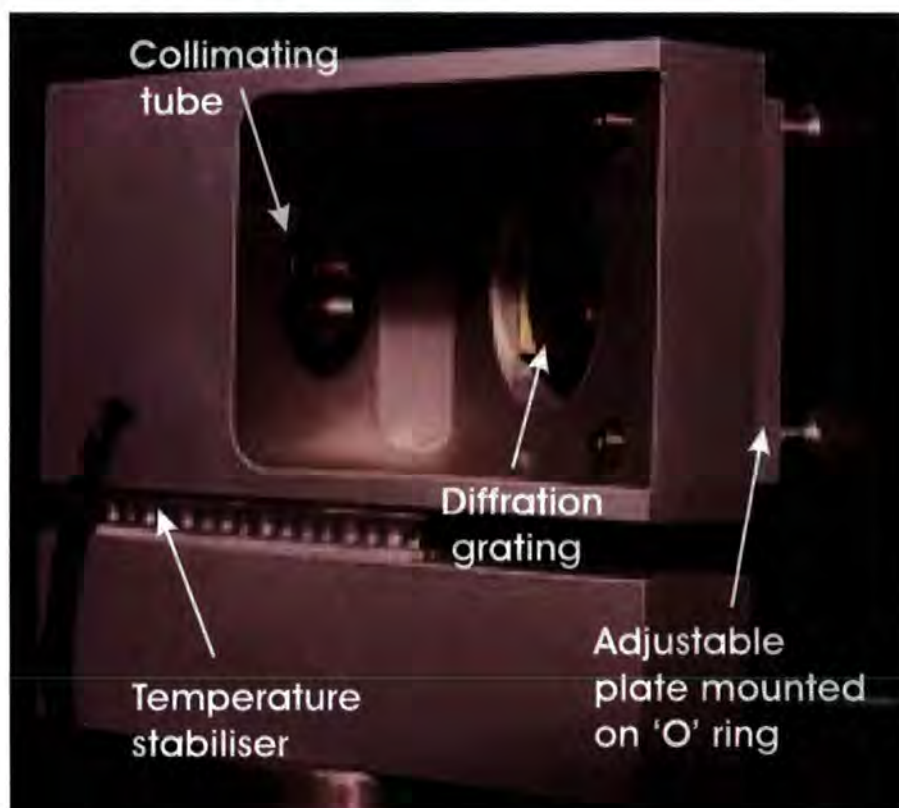


Figure 5.3: Compact diode laser design with tuning piezos mounted upon a 'O' ring mount

5.2.3 Compact Mirror Mount Design

This design was based around a temperature stabilized block of aluminium into which the laser diode collimating tube was set along with a miniature mirror mount (Thorlabs KS05) to hold and adjust the grating. The assembly was placed within an aluminium box to isolate from air currents. A photo-

graph of this laser with the outer box removed can be seen in figure 5.4. This laser satisfied the requirements of compact size and frequency stability necessary to carry out the experiments and so further design iterations were not pursued. It has since become the standard ‘home-made’ laser at Durham and is currently used by all groups within the Durham atomic physics section and was used for the thesis work of D. Smith [131] and an investigation into dichroic-atomic-vapor laser lock (DAVLL) lineshapes in reference [132].

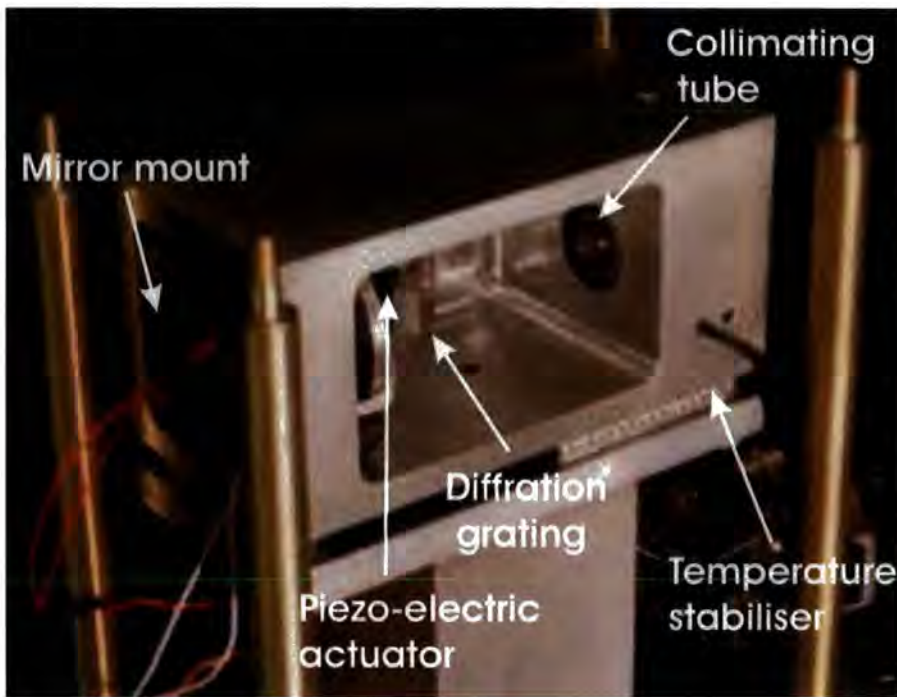


Figure 5.4: Final compact diode laser design used for the laser cooling experiments. This model is now used throughout the Durham atomic physics groups

During the course of this thesis work, the lasers built to this compact design have remained on transition (without the need for re-alignment) for over a year. The output beams do not have rotational symmetry, in fact the horizontal and vertical ($1/e^2$ radius) spot size differed by a ratio of $\sim 2:1$. The longer of which was ~ 1 mm.

5.3 Laser Stabilization

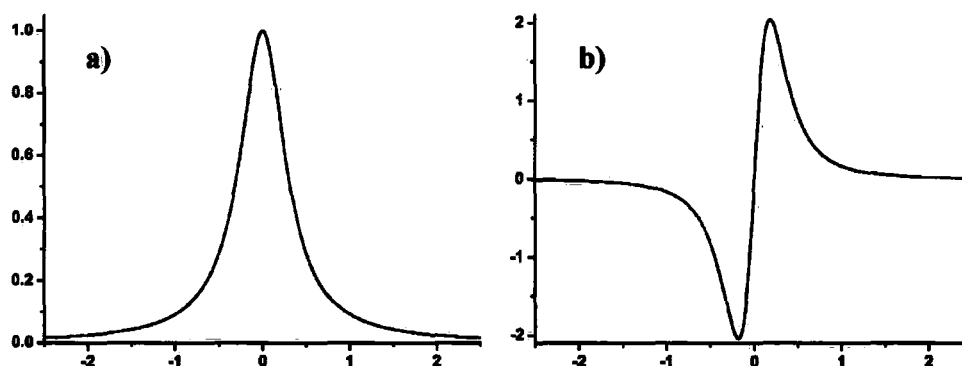


Figure 5.5: a) Normalized Lorentzian lineshape b) Derivative of the Lorentzian

In order to stabilize the laser frequency it is necessary to lock the laser to the peak of a naturally broadened Lorentzian feature in the hyperfine spectrum, see figure 5.5a. It is simpler electronically to lock to a zero crossing than a peak of the spectrum and so a derivative ‘error’ signal like that shown in figure 5.5b is sought. Locking is achieved by means of an integrator circuit along the lines used by Rovera *et al.* [133]. The actual circuit used is shown in figure 5.6. The optimum values of RC in the integrator depends upon the slope of the input signal used, since the output voltage is equal to the integral of the input voltage divided by the RC time constant, i.e.

$$V_{\text{out}} = -\frac{1}{RC} \int V_{\text{in}} dt. \quad (5.1)$$

During the setup stages of the experiment several different schemes for creating ‘error’ signals for the locking of the laser frequency were explored requiring different values of RC . The following section briefly explains the relative merits of these schemes and the reasons for choosing them. In each case the locking frequencies were compared to a hyperfine spectrum [129] like that shown later in figure 5.10a. In this work ^{85}Rb was used due to its greater natural abundance leading to a greater level of absorption in a vapour cell.

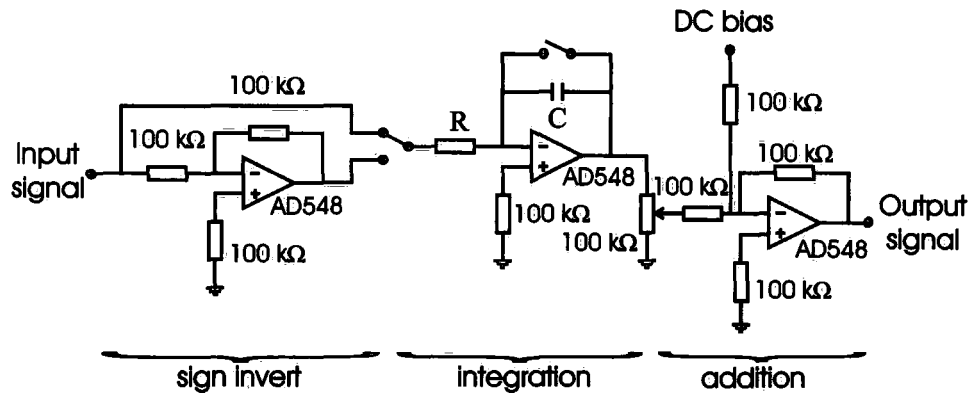


Figure 5.6: Integration circuit used to stabilise the laser frequency

5.3.1 Dichroic-Atomic-Vapor Laser Lock (DAVLL)

The DAVLL was first demonstrated by Cheron *et al.* [134] in 1994 and first demonstrated on alkali vapour by Corwin *et al.* [135] in 1998. This technique uses a magnetic field to split the Doppler-broadened absorption signal into its Zeeman components. The optical setup for the DAVLL is shown in figure 5.7. A linearly polarised input beam has its polarisation angle set by a half-wave plate and then passes through a rubidium vapour cell in a uniform magnetic field. The linearly polarised beam can be thought of two overlapped beams of opposite helicity where the different components of circular polarizations drive different Zeeman transitions. The Zeeman transition $\Delta m_F = +1$ is at a higher frequency than the original transition and absorbs light of one helicity. The $\Delta m_F = -1$ transition is at lower frequency and absorbs light of the opposite helicity. The light then passes through a quarterwave plate followed by a polarizing beam splitter which separates the right and left circular polarized components. For room temperature Rb, when the laser frequency is scanned, each photodiode receives a Doppler-broadened transition spectrum, one shifted to a higher and the other to a lower frequency, with a peak to peak difference of ~ 500 MHz for a magnetic field of the order 100 G. The difference between the two signals gives an antisymmetric ‘error signal’ that is used for laser locking. The desired locking frequency is positioned near the middle of the locking slope see figure 5.10c. The recapture range, defined as \pm the maximum frequency excursion that

the laser can experience and return to the lock point, is of the order 1 GHz. Typically a beam of power $\sim 10 \mu\text{W}$ was used.

Due to the broad shallow locking slope and the asymmetry of the Doppler broadened transitions, intensity fluctuations on the laser light are translated into frequency fluctuations. These frequency fluctuations lead to fluctuations in MOT atom number (discussed in section 6.4) and reduced contrast when imaging the atoms. In preliminary experiments we found that the frequency of the lock point would jitter by up to 3 MHz over a time scale of few seconds and cause the MOT atom number to fluctuate drastically. For this reason we preferred to investigate different locking schemes.

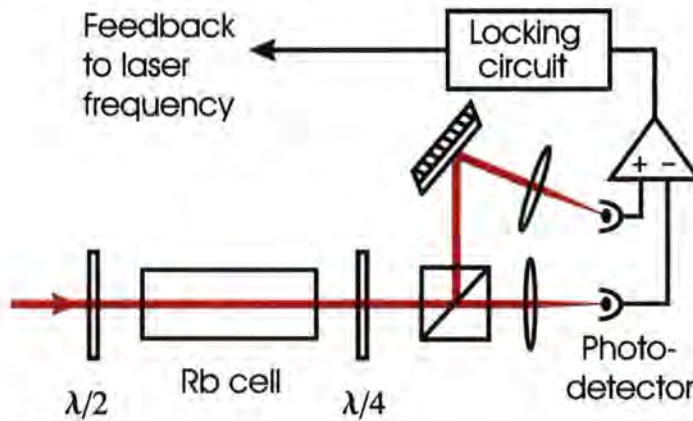


Figure 5.7: Optical setup for the DAVLL. A linearly polarised probe beam with intensity $I = 0.6 \text{ mW/cm}^2$ has its polarisation angle rotated and is then passed through a Rb vapour cell. The beam is then separated into its circular components and the difference signal between them used for laser locking.

5.3.2 Dither Lock

The dither lock is the preferred lock of choice for experimenters who need to stabilize laser frequencies to a transition line center with the greatest accuracy [136]. The optical setup for the dither lock is relatively simple and shown in figure 5.8, but more electronics are required than with DAVLL or polarisation spectroscopy lock (see below). Another drawback of the dither lock technique is that the laser frequency is modulated by necessity. To achieve a dither lock, a signal generator is used to add a small modulation at ~ 10

– 100 kHz to the laser current thus producing a frequency modulation depth of a few hundred kHz. When the laser frequency is close to resonance, this frequency modulation produces an amplitude modulation of the photodiode signal. A hyperfine spectrum [129] like that shown in figure 5.10b is sent to a phase sensitive detector (i.e. lock-in amplifier) which transforms this modulated signal into a derivative signal. The hyperfine spectrum exhibits six features, three of which are the $F = 3 \rightarrow F = 2, 3, 4$ and the other three are cross-over resonances [137]. Typical beam powers are $10 \mu\text{W}$ for the probe beams and $80 \mu\text{W}$ for the pump. After adjustment of the bandpass filter, dither frequency and phase control of the lock-in amplifier, an ‘error’ signal like that shown in figure 5.10d is achieved and is then input to the locking circuit. This method has a steeper locking slope than the DAVLL but a much smaller recapture range ($\sim 50 \text{ MHz}$).

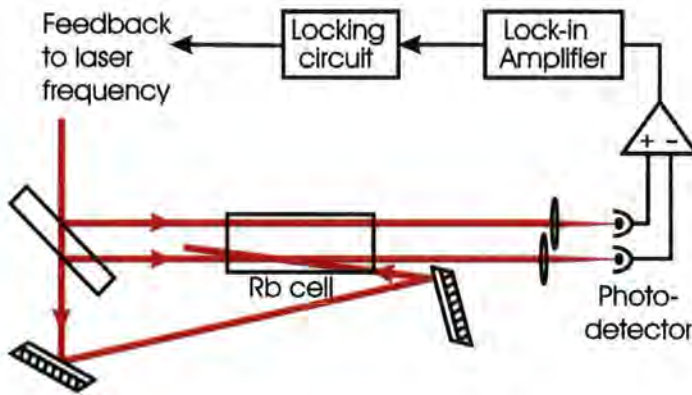


Figure 5.8: Optical setup for the dither lock. Two probe beams are created from reflections from the front and back faces of a thick glass slide. One beam is overlapped with a counter propagating probe beam. The difference between the signal from both probe beams is sent to locking circuitry.

Although this method of laser locking usually provides a consistent and small offset from line centre which can be corrected for [136], we found that our locking point was inconsistent. By monitoring the absorption of another beam derived from the same laser within a reference hyperfine spectrum we observed that the lock point changed by up to a few MHz from day to day. This effect was never satisfactorily explained but could possibly be attributed to the poor quality of the lock-in amplifier used. The drift in locking point

together with the heating of the atoms due to the frequency dither made this locking scheme unattractive. Subsequently, a third scheme based on polarisation spectroscopy was implemented.

5.3.3 Polarization Spectroscopy Lock

Polarization spectroscopy was first demonstrated by Wieman and Hänsch in 1976 on the Hydrogen Balmer- β line with a cw dye laser [138]. Following that much work was done to develop laser stabilization techniques based upon polarization spectroscopy [139–141]. In essence the technique is based on a light induced birefringence of an absorbing gas. The optical setup is shown in figure 5.9. The polarisation rotation of the probe is monitored in the presence of a strong circularly polarised pump beam. At the cooling transition frequency there is a large anisotropy in the medium resulting in the steep gradient spectrum used for locking seen in figure 5.10d. In-depth discussions of this effect can be found in References [130, 142]. The slope of the polarisation spectrum is similar to that of the dither signal but the recapture range can be made much larger by deliberately mis-aligning the pump beam. This ‘washes out’ some of the Doppler-free features leaving only the strongest transition. Typically beam powers of 80 μ W and 10 μ W were used for the pump and probe beams respectively.

5.3.4 Summary and Comparison of Locking Techniques

A table indicating the relative strengths of the three locking schemes is shown in table 5.1. We can see that polarisation spectroscopy compares favorably against the other locking schemes in terms of accuracy and precision. Although the recapture range is not as large as DAVLL, it is sufficiently large to provide a robust lock and keep the laser frequency stable.

Polarisation spectroscopy was found over time to be the most reliable locking scheme as well as the simplest to implement. Although there is a strong dependence of magnetic field on the anisotropy of the Rb vapour, the zero crossing of the locking slope moves very little with changing field, see chap-

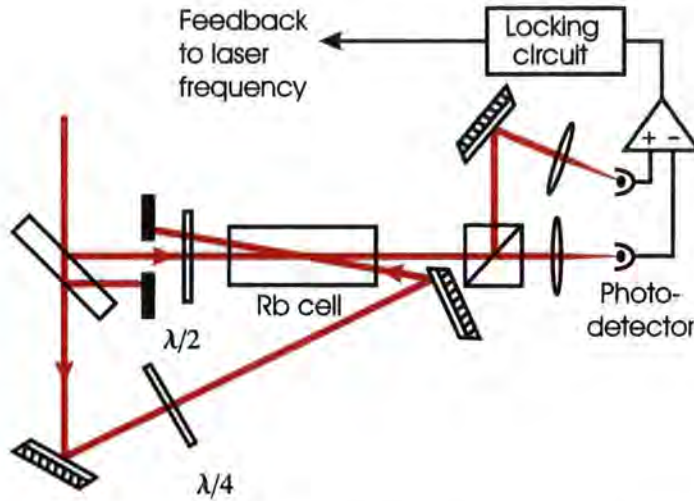


Figure 5.9: Optical setup for the polarisation spectroscopy lock. The reflection of the laser beam from a thick glass slide creates a probe beam and the transmitted beam is used as the pump beam. The (nearly) counterpropagating beams overlap in a Rb vapour cell. A half-wave plate is used to rotate the plane of polarization of the probe beam and a quarter-wave plate is used to make the pump circularly polarized.

Locking Scheme	Deviation from Lock Point (MHz)	Error Signal Slope (V/MHz)	Recapture Range (MHz)
DAVLL	> 100	~ 0.003	>1000
Dither	~ 3	~ 0.02	~ 50
Polarisation Spectroscopy	~ 2	~ 0.02	> 100

Table 5.1: Comparison of the locking techniques used in this work

ter 2 of reference [51]. Polarisation spectroscopy was used to stabilize the frequency of the cooling master laser. DAVLL was used to stabilize the frequency of the repumping laser because the lock is more robust and small frequency drifts are unimportant. The photodiode circuit used to create the error signal is shown in figure D.1 in appendix D.

5.4 The Optical Setup

5.4.1 Introduction

To realise the pyramid and second MOT we needed:

- For the pyramid MOT - approximately 40 mW [143] of frequency stabilised light detuned to the red of the cooling transition and a few mW of light stabilised to the repumping transition, see figure 2.1.
- For the second MOT, optical molasses and fluorescence imaging (see chapter 6) - approximately 20 mW of cooling light, the detuned frequency of which needed to be adjustable between $\Delta = 0$ and $|\Delta| \sim 10\Gamma$ and few mW of light stabilised to the repumping transition.

The laser setup and optical table was split into two clear sections. Section 1, contained the diode lasers along with frequency control optics and stabilisation spectroscopy. Section 2 was enclosed behind 'blackout' panels and contained the MOT beams in the vicinity of the vacuum chamber. The light created in section 1 reached section 2 via optical fibers (discussed later)

5.4.2 Section 1

A schematic of the optics in section 1 can be seen in figure 5.11 and a photograph of the setup seen in figure 5.12

Stabilised Lasers

The (compact mirror mount design) laser stabilised to the cooling transition using polarisation spectroscopy will henceforth be referred to as the 'master'

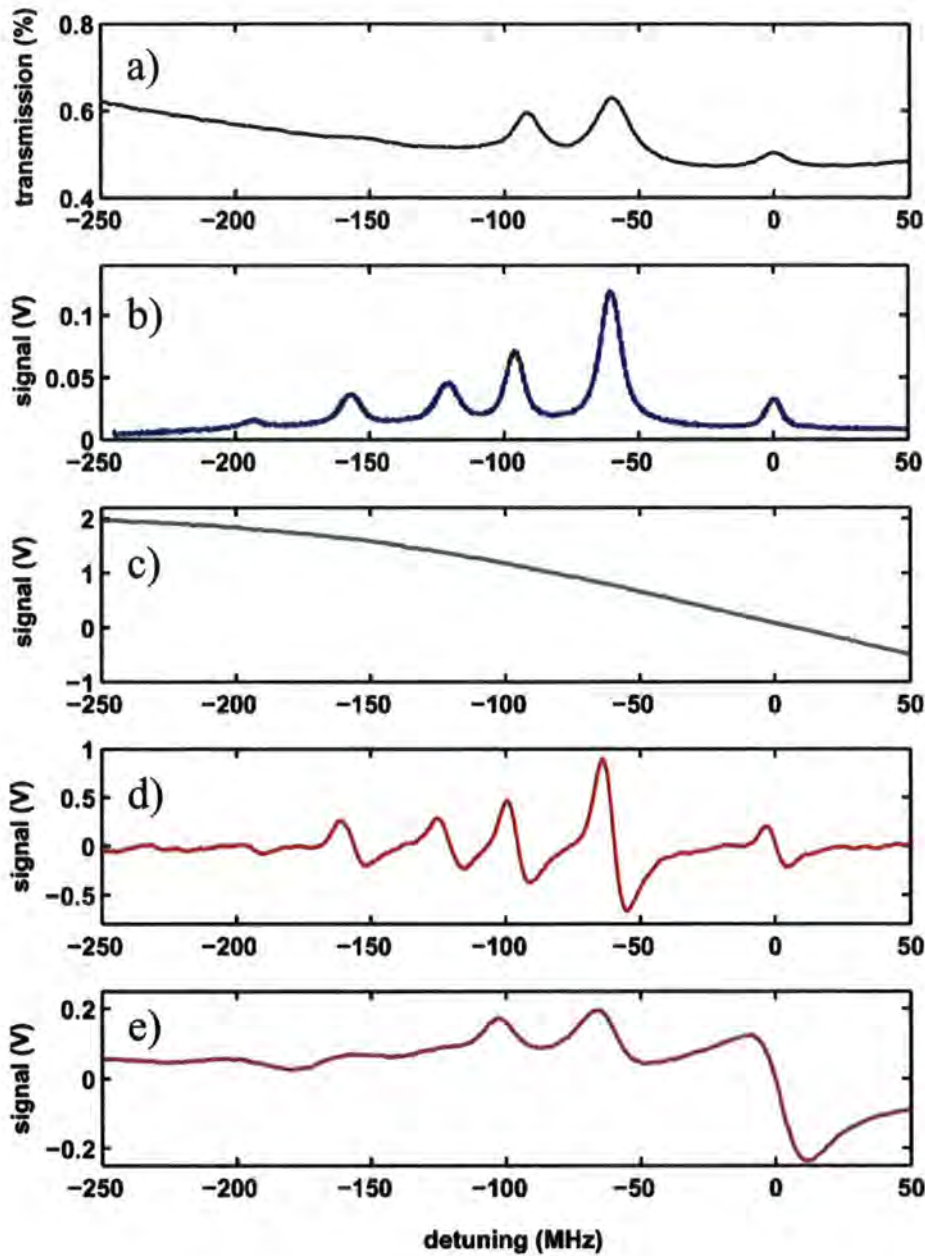


Figure 5.10: Comparison of ^{85}Rb spectra of (top to bottom); a) sub-Doppler hyperfine spectrum on Doppler background, b) hyperfine spectrum with Doppler background subtracted, c) DAVLL error signal, d) dither lock error signal and e) polarisation spectrum for ^{85}Rb , $F=3 \rightarrow F'$. The spectra have been calibrated using known values of the hyperfine splitting from reference [78]. Zero detuning has been set at the frequency of the closed cooling transition

laser. The laser locked close to the repump transition using the DAVLL will henceforth be referred to as the 'repump' laser. Both lasers produce a maximum laser output power of ~ 70 mW and have rms linewidths of less than 500 kHz (deduced from a beat signal sampled at 2MHz). The mode-hop free scanning range for each is greater than 5 GHz.

Slave Lasers

To supply the required amount of cooling light necessitated the use of injection locked slave lasers because we believed that a single home-made diode laser alone would not be able to produce enough light for the pyramid and second MOT. A small amount of light (typically ~ 1 mW) from the master laser was injected into the facet of each slave diode laser resulting in the slave laser output light matching the frequency and linewidth of the input light. Two slave lasers were used to supply light to the pyramid MOT and the second MOT. They will henceforth be referred to as the P-MOT slave and S-MOT slave respectively. The slave lasers were very similar in design to the master lasers but without the diffraction grating. The maximum output power of the slave lasers is ~ 80 mW.

Acousto-Optic Modulators

Fine frequency control of the laser cooling light was achieved using acousto-optic modulators (AOMs) (the principle behind which is discussed in reference [144]). The master laser beam was passed through an optical isolator and then split into two beams (with an intensity ratio of $\sim 10:1$) using a half-wave plate and a polarising beam splitting (PBS) cube. The weaker beam was double-passed through a Crystal Technologies (3080-122-TeO₂-1W-80MHz) AOM which shifted its frequency up by 100 MHz. This beam was then fed to the stabilisation spectroscopy. The high intensity beam was then split into a further two beams of approximately equal intensity and each double passed through an AOM, picking up a frequency shift of between 100 and 170 MHz. This results in two beams which can be independently detuned from atomic resonance over the range $|\Delta|=0-70$ MHz. These beams were attenuated before being used to injection lock the slave lasers.

The repump laser beam was passed through an optical isolator and then split into two beams using a PBS cube. The weaker beam was fed to the stabilisation spectroscopy. The other beam was passed once through an Isle Optics (LM080) AOM which shifted its frequency up by 80 MHz. The beam was then split into two beams of approximately equal intensity which were then overlapped with the output beams of the slave lasers. A schematic of the optical setup can be seen in figure 5.11. The two combined slave/repump laser beams were then coupled into two optical fibers which supply light to the pyramid MOT and second MOT.

Optical Fibers

There were several advantages to using optical fibers:

- The fibers provide excellent spatial filtering resulting in a clean Gaussian laser mode.
- The alignment of the lasers and the alignment of the MOT optics are conveniently separated.
- The length of the fiber allows for the spatial separation of the lasers and the main part of the experiment such that the experiment can be conducted in a dark enclosure.

We used single mode polarisation preserving optical fibers from OZ optics (PMJ-3AF3AF-780-5/125-3-6-1). Great care had to be taken to align the orthogonal polarisations of the slave and repump laser beams with the axes of the optical fibers to ensure stable polarisation output from the fibers.

Shutters

Two types of mechanical shutter were used on this experiment; one based on a speaker coil [145] and the other based upon a computer hard disc [146]. In performance both types of shutter are faster and create less acoustic vibration than shutters based on electromagnetic actuators or relays. The shutters can be placed on the optical table close to the lasers without affecting the laser

lock. The switching time for each is of the order $100 \mu\text{s}$ (for a $w_0 \sim 20 \mu\text{m}$ focused beam) but the range of travel is much greater for the hard disc shutter than the speaker coil (5 cm cf. 5 mm). Three shutters are used in total, see figure 5.11. Speaker coil shutters on the repump laser beam before the AOM and just before the S-MOT slave fiber coupler. A hard disc shutter is placed just before the pyramid MOT fiber. The deflection from the AOM on the repump beam was also used as a fast optical shutter. Each shutter was controlled from a computer via the circuit shown in figure D.4 in appendix D. Two of the three shutters used for the experiment and the circuit used to drive them were constructed by M. Pritchard.

5.4.3 Section 2

A schematic of the optics in section 2 can be seen in figure 5.13.

Pyramid MOT alignment

The alignment of the pyramid MOT was relatively simple. The P-MOT fiber had a quarter-wave plate placed directly after its output to circularly polarise the strongly diverging output beam. This diverging beam was then collimated using a 50 mm diameter $f = 25 \text{ cm}$ lens creating a beam with a $1/e^2$ radius of $\sim 18 \text{ mm}$ and peak intensity of 8.3 mW/cm^2 . This beam was then deflected (by a 75 mm diameter mirror) through an angle of 45° into the pyramid chamber. Alignment was achieved by masking half of the input beam and aligning the beam reflected from the pyramid optics onto the mask.

Second MOT alignment

The second MOT was more difficult to align than the pyramid MOT, in part due to the need to create three beams with specific helicity but also due to the shortage of space around the science chamber in which to work. The S-MOT fiber output a diverging beam which was collimated by a 1" diameter $f = 8 \text{ cm}$ lens resulting in a beam with a $1/e^2$ radius of $\sim 8.0 \pm 0.1 \text{ mm}$ and a peak intensity of 20 mW/cm^2 . This beam was then split into three

beams containing an equal intensity of cooling light using half-wave plates and PBS cubes. One of these beams was raised to the height of the science chamber with a periscope before the appropriate helicity was generated with a quarter-wave plate. It was then directed horizontally through the centre of the science chamber. The other two beams were reflected out of the horizontal plane using mirrors angled at 22.5° to the vertical, thus creating two orthogonal beams at an angle of 45° to the horizontal which intersected at the centre of the science chamber. Each of the three beams was then returned to linear polarisation using a quarter-wave plate before being retro-reflected. This resulted in the light field configuration required to achieve a MOT as discussed in section 2.2.3.

5.5 Summary of the Optical Setup

In summary, the light for the MOTs was created using home-made diode lasers. The master and repump lasers were stabilised to spectroscopic features of Rb and given fine frequency control by AOMs. The light from the master laser was used to injection lock two slave lasers and then cooling and repump light was overlapped and supplied to the separate MOTs using two optical fibers. The pyramid MOT was realised using a single circularly polarised beam. The second MOT was realised using a set of three orthogonal retro-reflected circularly polarised beams which intersect at the centre of the science chamber.

Once the optical setup was complete we were able to perform laser cooling experiments on atomic Rubidium. The following chapter details how the experiments were performed and presents the results obtained.

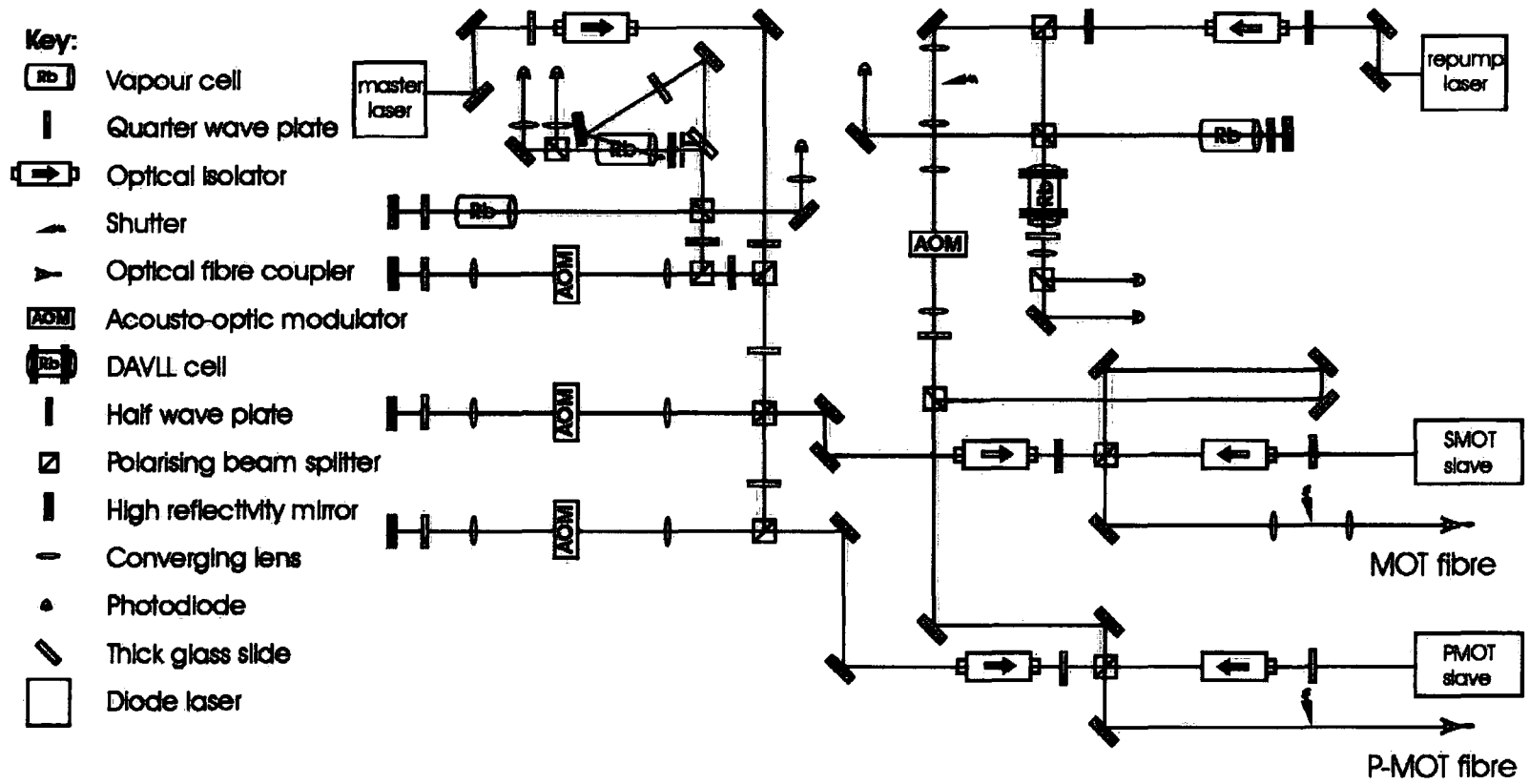


Figure 5.11: Section 1 of the optical setup. The light from the master laser is stabilised using spectroscopic features of Rb. Fine frequency control is achieved using AOMs. Slave lasers are injection locked to the master light. The repumping light comes from the repump laser and is overlapped with the slave laser light before being coupled into optical fibers.

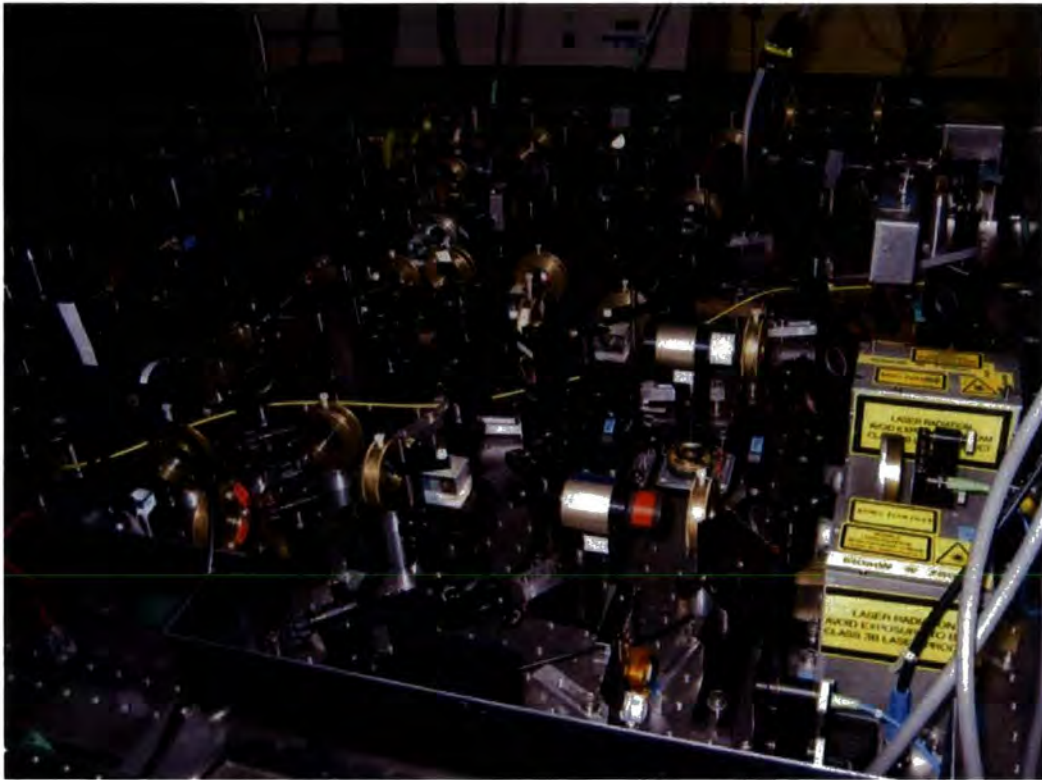


Figure 5.12: Photograph of section 1 of the optical setup. The slave lasers are situated in the bottom right corner

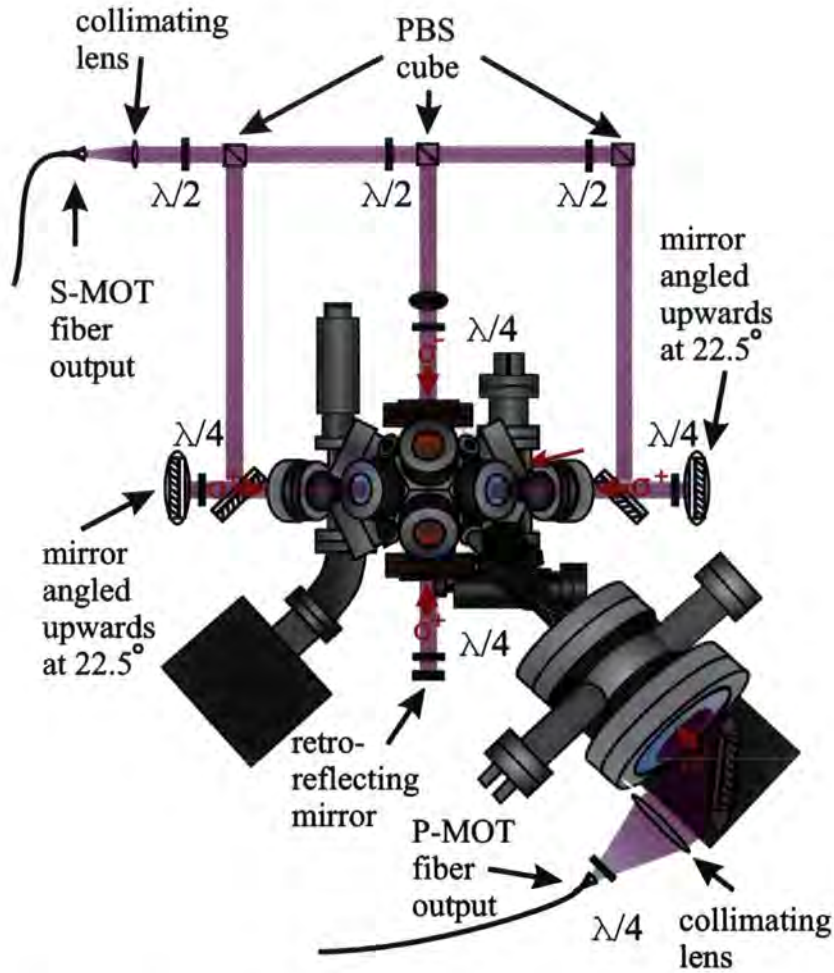


Figure 5.13: Section 2 of the optical setup. The pyramid MOT uses a single circularly polarised and collimated beam. For the second MOT, the beam is split into three and then each beam circularly polarised using $\lambda/4$ plates. The beams are each retro-reflected to make a set of three orthogonal counter-propagating beams. For clarity, the retro-reflecting optics for the out of plane beams are not shown.

Chapter 6

Experimental Procedures

This chapter describes the laser cooling experiment conducted using the apparatus described in the previous two chapters. The specifics of laser parameters and timing sequences used are reported and results presented. Before this we will cover the more general (but equally important) requirements for performing the experiments.

6.1 General Infrastructure

Since our previous reported work [49, 50, 112] the laboratory used for the CO₂ laser experiment has been completely refurbished and much of the infrastructure build up from scratch. This section briefly reports the important features.

6.1.1 Plumbing and Laser Safety

In June and July 2005 the laboratory was re-wired and had the chilled water circuit completely replaced. Once the work was completed, chilled water was supplied to the MOT coils (see section 6.1.2) using 6 mm push-fit pipes and connectors. Flow meters (Honsberg PN300) and temperature sensors were attached to the cooling water circuit. This was to enable cut-out of the MOT power supply and prevent overheating should the flow of water fall below 1 l/min or its temperature rise more than 5° C. Chilled water was also

routed to the CO₂ laser and some of its optical components (see chapter 7). To adhere to stringent new regulations relating to laser safety several new features were added to the experimental setup. These included the addition of ‘blackout’ covers and beams guards to the optical tables resulting in the complete enclosure of the vacuum chamber. This could result in an improved signal to noise ratio of measurements as light pollution from ambient laboratory conditions will be minimised. In addition to this, interlocked shutters were added to all diode lasers so that the light is blocked if the door is opened. We preferred this option to shutting off the power to the lasers, which if done repeatedly could cause the laser diodes to fail.

6.1.2 MOT Coils and Shim Coils

MOT Coils

The quadrupole coils for the Pyramid MOT and the second MOT were wound from hollow bore, 4.1 mm square section copper. This type of material was used so that the coils could be water cooled, allowing higher currents to be used. Hence, fewer turns are required, reducing the inductance of the coils and expediting the turn off of the magnetic field. The pyramid MOT coils have been described previously in section 4.3. The coils for the second MOT were wound onto a removable former using a lathe. Once completed the coils were mounted around a pair of opposite viewports on the science chamber, see figures 4.10 and 4.11. Extensive testing was performed to ensure that minimal heating ($<5^{\circ}$ C) of the coils occurred for the range of currents to be used in the experiment (10–150 A). The water cooling circuit was designed so that water was fed to parallel coils starting at the inside (close to the viewport) and working outwards. 36 turns were wound onto each coil producing a magnetic field gradient of ~ 0.11 G/A/cm at the MOT. The resistance of each coil was measured to be 26 m Ω . The coils were powered by a Hewlett Packard 6671A power supply and the current switched on and off using a simple FET circuit. The measured turn-off time for the coils in place on the chamber (monitored from a Honeywell CSNR161 sensor) was under 140 μ s.

Shim Coils

There were nine shim coils in total used on the experiment. Three coils aligned parallel to the x , y and z axes of figure 4.3 were used to adjust the position of the pyramid MOT. They were composed of 50 turns of 0.5 mm diameter insulated copper wire wound onto perspex formers with a radius of 6.5 cm. A further 6 coils consisting of 25 turns of 1 mm diameter insulated copper wire were wound around the sides of a cuboid frame of dimension $36 \times 58 \times 78$ cm. The frame was centered on the second MOT with each side aligned parallel to the x , y and z axis in figure 4.1. These coils were used to cancel the ambient laboratory field at the centre of the science chamber. All of these coils were controlled and switched from the computer. Owing to the pyramid MOT being positioned at an unusual angle to the second MOT, the changing of any one coil necessitated the changing of many others to correct the field at the region of the second MOT. This was a troublesome feature of the experimental arrangement.

6.1.3 Magnetic Shielding

The ion pumps connected to the chambers each contain a large magnet, the field from which causes a magnetic field gradient across the MOT region. This is undesirable because optical molasses and Raman transitions (proposed to initialise qubit states, see section 8.3 and reference [68]) are sensitive to magnetic fields.

We designed Mumetal shields to encase the ion pump magnets. This high-permeability alloy provides a path of least reluctance for magnetic fields lines and thus prevents the magnetic field from the pumps from reaching the vacuum chambers. Two small holes had to be left in the shield to allow mounting of the pump and access for the controller cable. Although the magnetic fields at the experimental area could not be measured directly, we inferred the magnetic field by measuring at an equal distance in the opposite direction. For the science chamber MOT the B-field from the pump was reduced from $B \approx 2.4$ G with a gradient of 0.5 G/cm to 0.1 G with a gradient of 0.03 G/cm. Figure 6.1 shown a photograph of the experiment from above. The top of the frame supporting the cancelation coils is in the foreground.

The pyramid MOT chamber and one of its shim coils can be partially seen at the bottom right. The Mumetal shield for the science chamber ion pump can be partially seen at the bottom left

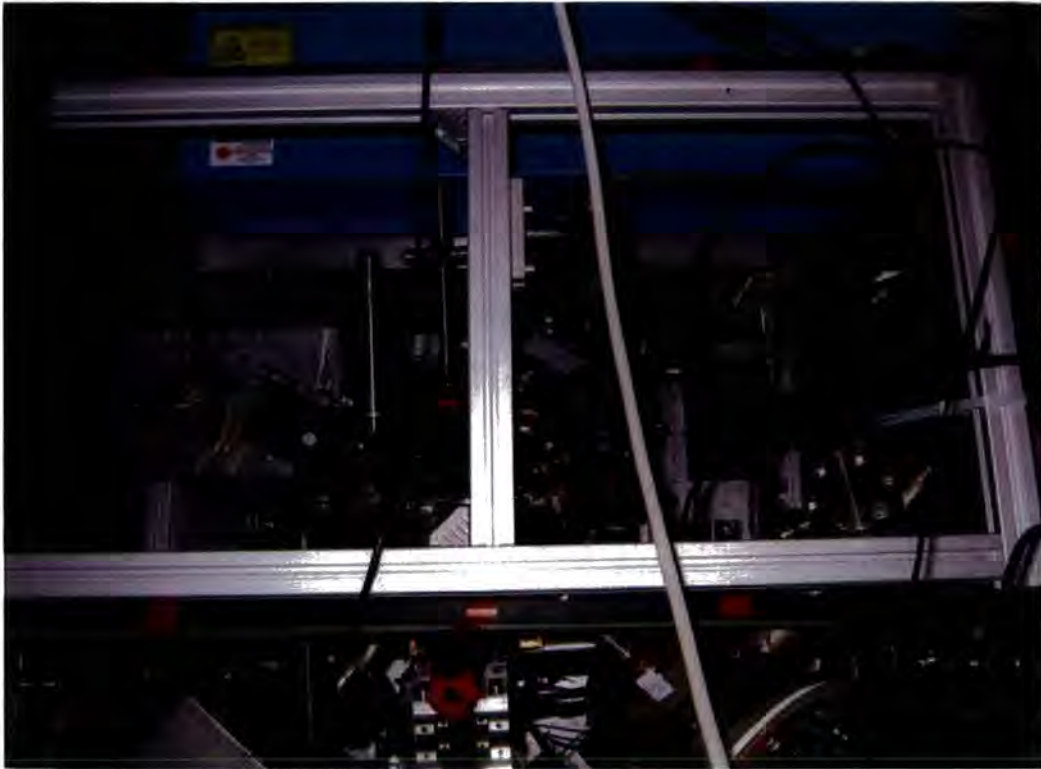


Figure 6.1: Photograph of the experiment from above. The top of the frame supporting the cancellation coils is in the foreground. The pyramid MOT chamber and one of its shim coils can be partially seen at the bottom right. The Mumetal shield for the science chamber ion pump can be partially seen at the bottom left.

6.2 Computer Control of the Experiment

The precision timings required for this work were programmed and output from a PC via National Instruments software and hardware. Two PCI cards were used: A PCI-DIO-32HS 32 channel digital input/output (DIO) board controlled the majority of the equipment. A PCI-6713 8 channel analog output (AO) board (also including a further eight DIO channels) controlled

the CO₂ laser, received an input trigger for the experiment and provided the 20 MHz clock frequency on which all timing for the experiment was based.

Digital patterns were written within LabVIEW software to control the equipment with a time resolution of 10 μ s. Once written, a completed sequence was sent to a buffer on the PCI boards, from there TTL signals were sent to various pieces of equipment. Due to the finite size of the buffer there is a trade off between the time resolution of the program and the duration.

The LabVIEW programming used in this work was based upon methods used in experiments at Oxford university. Inherited code was extensively modified to suit our needs.

6.2.1 Radio Frequency Electronics for AOMs

As described earlier in section 5.4.2, the laser frequencies and intensities were adjusted by AOMs. These devices were controlled by radio frequency (RF) electronics. Specifically, the frequency was set using minicircuits ZOS-100 voltage controlled oscillators (VCOs). The amplitude of the signals were controlled by minicircuits ZX73-2500 voltage controlled attenuators (VCAs). Minicircuits ZHL-3A 2W amplifiers then forward the signals to the AOMs. Voltage level boxes which were designed and manufactured in-house were used to control the voltage levels supplied to the VCOs and VCAs. Details of these can be found in reference [51]. The RF set-up used to control the modulators is shown in figure 6.2

We found that reflection back from the VCAs into the VCOs caused the frequency of the VCOs to change from their set values. To correct for this, the AOM frequency needed to be adjusted accordingly when the attenuation was altered.

6.2.2 Testing of the Injection Locking

Testing of the injection locking was performed on a regular basis, typically at the beginning of each day. A labVIEW routine was written to cycle through the desired frequency detunings for the experiment (ranging from $\Delta = 0$ to $\sim |\Delta| = (2\pi) 70$ MHz). A flipper mirror was placed before the input to

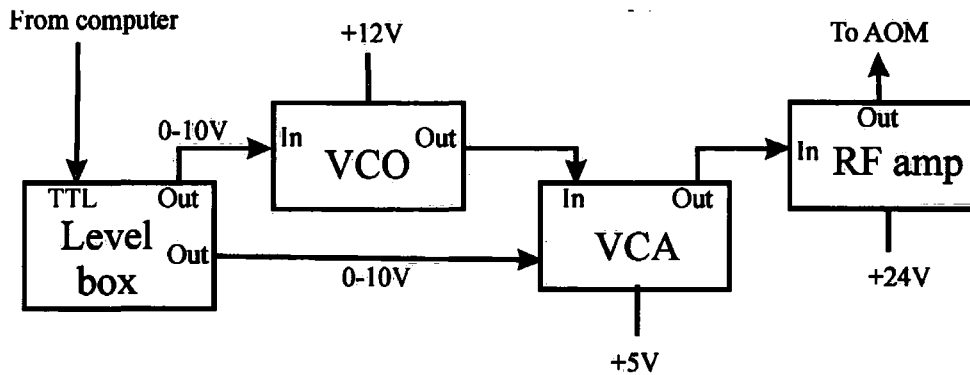


Figure 6.2: The RF set-up used to control the AOMs. TTL signals are received from the computer by the level box. The level box then outputs a voltage to the VCO (minicircuits ZOS100) to set the frequency, and a second independent voltage to the VCA (minicircuits ZX73-2500) to set the amplitude. An RF amplifier (minicircuit ZHL3A) then supplies an amplified signal to the AOMs.

the S-MOT fiber diverting the slave laser light to a saturated absorption spectroscopy setup. With the master laser scanning over resonance, the spectrum from the slave laser light was compared to that from the master laser to ensure that the injection locking was working as required. Due to the frequency-dependent efficiency of the AOMs, the intensity of the injecting beam had to be compensated using the VCAs for different AOM frequencies. In order to achieve large detunings, the AOMs were typically operated far from their optimum frequencies.

6.3 Optimising the Pyramid MOT

Once the light for the cooling and repumping transitions was output from the P-MOT fiber (as described in section 5.4.3), the rubidium dispensers were activated (by passing ~ 2.5 A through them) and the quadrupole coils turned on, the pyramid MOT was then formed and could be viewed with a CCD camera. An image of the pyramid MOT can be seen in figure 6.3. The MOT could be shifted in position using three orthogonal shim coils.

An investigation was performed to find the optimum pyramid MOT param-

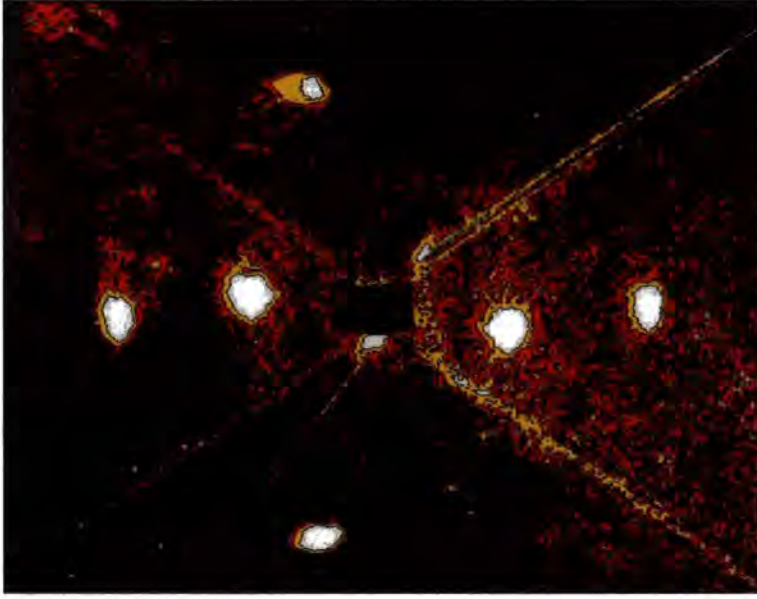


Figure 6.3: A false colour image of the pyramid MOT. Multiple reflection of the MOT in the pyramid optics can be seen. The field of view represents a 4×4 cm section of the pyramid optics.

eters for maximising the flux of atoms from the pyramid MOT. A sequence with a repetition rate of 500 ms was used to pulse on and off the second MOT while the pyramid MOT ran in cw mode. The fluorescence from the captured atoms from the second MOT was observed on an oscilloscope while the currents to the quadrupole and shim coils were altered. The optimum current for the quadrupole coils was 12 A giving a B-field gradient of 8.4 G/cm. Next the detuning was altered and the second MOT filling rate monitored. Figure 6.4 shows how the second MOT filling rate was affected by the detuning of the pyramid MOT.

The maximum filling rate was observed at a pyramid MOT detuning of -12 MHz so henceforth the detuning was set to this value. We found that for a Rb dispenser current of 2.5 A we achieved a flux of 8×10^7 atoms/s.

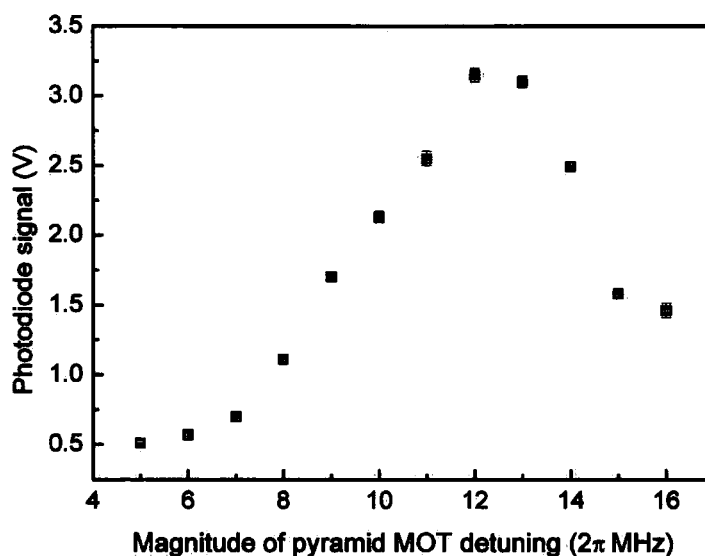


Figure 6.4: Fluorescence collected from the second MOT for various pyramid MOT detunings. Each point is the mean of 12 measurements. The error bars are the standard error on the mean.

6.4 Atom Number Measurements

The optical power emitted from the second MOT is given by

$$P_{\text{MOT}} = \Gamma_{\text{sc}} E N, \quad (6.1)$$

where N is the number of atoms in the MOT and E is the energy per photon ($E = hc/\lambda = 2.55 \times 10^{-19}$ J at 780 nm). Γ_{sc} was defined earlier in equation 2.1. A photodiode (Integrated Photomatrix IPL10050CW) circuit with variable gain was used to monitor the fluorescence from the MOT. The circuit is shown in figure D.2 in appendix D. A pair of 1" diameter plano-convex lenses ($f=10$ cm and $f=5$ cm) placed 10 cm from the MOT were used to image the MOT through a mini-conflat viewport. The emitted light passed through a 780 nm interference filter and a 50 % transmission neutral density filter giving a total measured transmission T_r of 42 % onto the photodiode. The power collected by the photodiode is given by

$$P_{\text{pd}} = \frac{V_{\text{pd}}}{\Theta G Z S}, \quad (6.2)$$

where V_{pd} is the voltage, G is the gain of the circuit, Z is the impedance of the photodiode circuit ($Z=1 \text{ M}\Omega$) and S is the photodiode sensitivity ($S = 0.45 \text{ A/W}$ at 780 nm [147]). Θ is the fractional solid angle for a lens of radius r at an image distance f , i.e. the percentage of the total emitted light collected by the lens.

$$\Theta = \frac{r^2}{4f^2} \approx 0.016. \quad (6.3)$$

Using equations 6.1 and 6.2 and taking into account the transmission of the filters gives us an expression for atom number,

$$N = \frac{V_{\text{pd}}}{GZT_r S \Gamma_{\text{sc}} \Theta}, \quad (6.4)$$

and hence we could relate the measured voltage to atom number.

Since the collection of a large number of atoms was not a priority for this project (the opposite in fact if we go on to use single atoms), we did not go on to try to maximise the number of atoms in the MOT (i.e. increase the laser power and beam size and increase the Rb pressure). We measured a maximum atom number of 5×10^8 atoms at $|\Delta| = (2\pi) 18 \text{ MHz}$ for beams with $1/e^2$ radius of 8 mm and a total intensity at the MOT of 60 mW/cm^2 . We measured the lifetime of the atoms in the second MOT by monitoring the atom number over time after the pyramid MOT light and magnetic field had been turned off. A plot of the MOT decay curve can be seen in figure 6.4. The $1/e$ lifetime of the MOT was deduced to be 33 s from an exponential decay fit to the data. This measured lifetime suggested that the pressure in the science chamber was better than that of previous experiments (discussed in section 4.1) and the move to a double MOT system had been worthwhile.

6.5 Temperature Measurements

The temperature of the laser cooled atom cloud was measured using a time of flight (TOF) technique. TOF techniques involve monitoring the spatial distribution of atoms released from the MOT over time as first reported by Lett *et al.* [148]. In 1D the initial position, (x_i) , and the final position, (x_f) , of an atom can be related by $x_f = x_i + v_x t$, where v_x is the velocity of the atom,

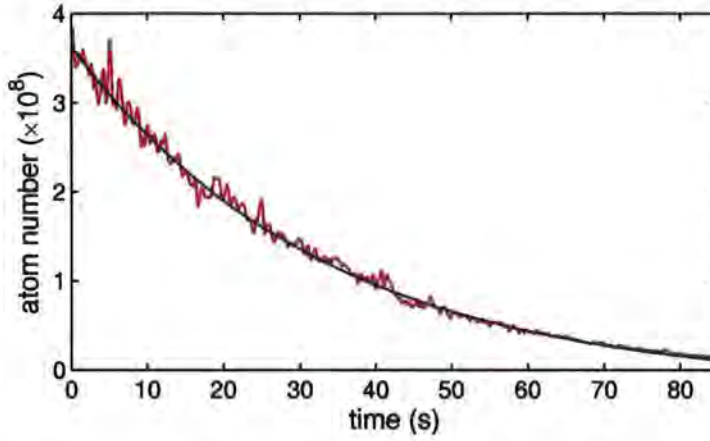


Figure 6.5: Fluorescence collected from the second MOT over time after the pyramid MOT was extinguished. The $1/e$ lifetime was measured to be 33 s

and t is the expansion time. This allows the final position distribution of a cloud of atoms, $P(x_f, t)$, to be written as a convolution of the initial position distribution $P(x_i)$ and the velocity distribution $f(v_{x_i})$. If it is assumed that the cloud has uniform temperature, then the initial position distribution is Gaussian, i.e.

$$P(x_i) = \frac{1}{\sqrt{2\pi}\sigma_x} e^{-x_i/2\sigma_x^2}. \quad (6.5)$$

The velocity distribution is Maxwellian, i.e.

$$f(v_x) = \left(\frac{m}{2\pi k_B T_x}\right)^{1/2} \exp\left(\frac{-mv_x^2}{2k_B T_x}\right), \quad (6.6)$$

where T_x is the temperature of the cloud and m is the mass of a single atom. The final position distribution can be written as

$$P'(x_f, t) = \int_{-\infty}^{+\infty} P(x_i) f(v_x) dx_i = \int_{-\infty}^{+\infty} P(x_i) f\left(\frac{x_f - x_i}{t}\right) dx_i = P(x_i) * f(v_x). \quad (6.7)$$

The expansion of the cloud over time then follows the form

$$\sigma_x(t) = \sqrt{\sigma_x^2(0) + \frac{k_B T_x}{m} t^2}. \quad (6.8)$$

This follows well known results for the convolution of Gaussian functions [149] and we know that the standard deviation of the final position distribution is the root of the quadrature sum of the standard deviation of the initial

position distribution and the standard deviation of the velocity distribution: Therefore, one can obtain the temperature of a cloud from the gradient of a graph of σ_x^2 against t^2 . By taking images of atom clouds at successive times and fitting Gaussian distributions to the images (as described in section 6.5.2), the temperature of the cold atoms can be inferred. Since the taking of each image causes heating to the atoms, the temporal sequence of images must be accumulated over subsequent MOT loading/releasing sequences.

6.5.1 Camera Calibration

Two types of camera were used on the experiment. JAI CV-M50 IR CCD cameras with $f = 58$ mm lenses were used to monitor the MOT and the Pyramid MOT. These cameras were not calibrated and were used for diagnostic purposes only. An Andor Ixon DV885 electron multiplied CCD camera was used to take all quantitative data for the experiment. This camera was chosen because it has the capability of detecting single photons and could prove invaluable for work on single atoms. The camera was fitted with two back to back singlet lenses with $f = 20$ cm and $f = 16$ cm. The resolution of the camera was tested by imaging an United States Air Force test card and a resolution of better than $9 \mu\text{m}$ was observed. To calibrate the image size, the camera was temporarily removed from the setup and used to image a piece of fine graph paper. The pixel size in the x and y directions were measured to be $4.54 \pm 0.05 \mu\text{m}$. The actual pixel size of the camera is $8 \mu\text{m} \times 8 \mu\text{m}$, yielding a magnification of $M = 1.76$. The camera's 1000×1000 pixel array then yields a relatively small field of vision of a square with dimensions approximately 4.5×4.5 mm. This limits the expansion times over which the atom cloud can be accurately measured. Once calibrated the camera was used to perform time of flight (TOF) measurements of the cold atoms. The camera was mounted above the chamber such that the MOT was viewed through one of the ZeSe viewports at an angle of $\arctan(2)$ to the horizontal. The ZeSe viewports transmit around 70% of 780 nm light.

6.5.2 Time of Flight Measurements

Fluorescence imaging was employed in the work to measure the released atom clouds. Although lacking the sensitivity of absorptive imaging, fluorescence imaging is simple to implement and requires no further optics than those already used for the MOT. In this work, the deciding factor to use fluorescence imaging was lack of space, since absorptive imaging requires further optics including an AOM fast shutter. The MOT was loaded until the MOT photodiode circuit measured a preset voltage (corresponding to the desired atom number). A Schmitt trigger circuit (shown in figure D.3 in appendix D) then sent a TTL pulse to the computer to initiate the LabVIEW routine. The atoms were released from the MOT and allowed to expand ballistically for a variable amount of time before the MOT light (typical intensities seen by the atoms are a few tens of times above the saturation intensity) was pulsed on 100 μs after the Andor camera trigger such that the image is taken within the time window set by the camera exposure time. A second background image with no atoms present was taken approximately 100 ms later and was subtracted from the first to give a cleaner image. The image was saved automatically in ASCII format by the Andor Solis software and given the name 'expansion time'.ms.asc

Fitting routine

A fitting routine was developed to facilitate the measurement of temperature from our collected images. When run, the program reads in an arbitrary number of saved images and fits a temperature and initial cloud size. Firstly, the images are binned into 'super pixels' to reduce the noise on the images and to reduce the number of points to be fit (this can also be done by the Andor software before saving the images). The program then performs a second smoothing by circularly shifting the image array to make each pixel an average of its nearest neighbours. This method helps to avoid centering the fit to a single spike in the distribution. A Gaussian profile (equation 6.9) is then fit through the mode of the distribution in the x and y directions.

$$P(x) = \mathcal{A} + \mathcal{B}e^{-(x-c)^2/2D^2} \quad (6.9)$$

Where \mathcal{A} is the height offset, \mathcal{B} is the height of the distribution, \mathcal{C} is the position of the cloud centre and \mathcal{D} is the standard deviation of the cloud. An integration through the atom cloud is not possible since the camera is not aligned with an axis of the MOT. An example of a typical sequence of images is shown in Figure 6.6 A typical output plot from the fitting routine is shown in figure 6.7. The slight difference in the values calculated from the x and y data fall within the bounds of experimental uncertainty ($\sim 10\%$) deduced from repeated measurements.

Heating due to Imaging

During the imaging process, the absorption of resonant light will inevitably impart momentum to the atoms and cause heating of the cloud. If during an imaging pulse of length δt , N photons are scattered by an atom then the root-mean-square velocity, v_{rms} , of the atoms will change by

$$v_{\text{rms}} = \sqrt{\frac{N}{3}} v_{\text{recoil}}, \quad (6.10)$$

due to the emission of isotropic radiation [150], causing a random displacement of

$$r_{\text{rms}} = \frac{v_{\text{rms}}}{\sqrt{3}} \delta t = \frac{\sqrt{N}}{3} v_{\text{recoil}} \delta t. \quad (6.11)$$

For zero detuning and a total intensity of $I/I_s=30$, using equation 2.1 gives $\Gamma_{\text{sc}}=(2\pi)$ 2.9 MHz. For our imaging duration of 80 μs , the number of scattered photons is then $\Gamma_{\text{sc}}\delta t \approx 1450$. Using the value of $v_{\text{recoil}}=6$ mm/s (from reference [1]) gives the random displacement $r_{\text{rms}}=6.1$ μm . Since the pixel resolution of our imaging system is ~ 4.5 μm the effect of this random displacement is to blur the images slightly. This suggests that an alternative imaging method should be sought when we progress to an imaging system with greater magnification and resolution for imaging single CO_2 lattice sites. We discuss this later in section 8.2.2 We note here that this estimate for heating is likely to be an underestimate as absorption also causes heating. Also an intensity imbalance in the MOT beams of greater than 1% would be a more significant cause of heating.

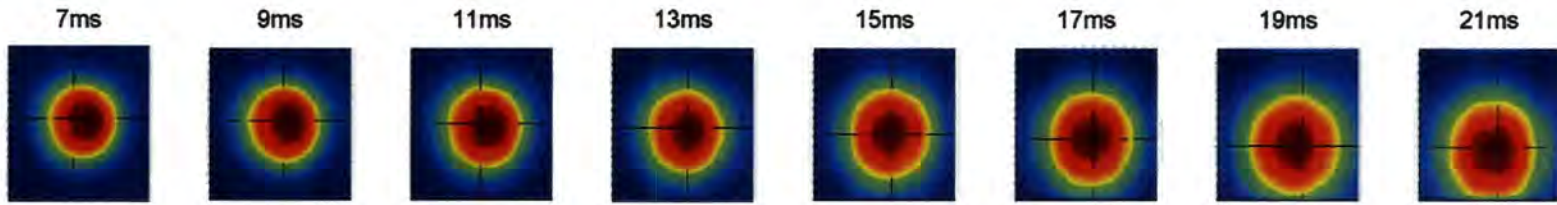


Figure 6.6: A Typical example of a set of temperature measurement images. The atom cloud dimensions are measured for increasing ballistic expansion times and fit to equation 6.8. Molasses duration = 12 ms. Fluorescence imaging duration = $80 \mu\text{s}$. The atoms can be seen to fall under gravity.

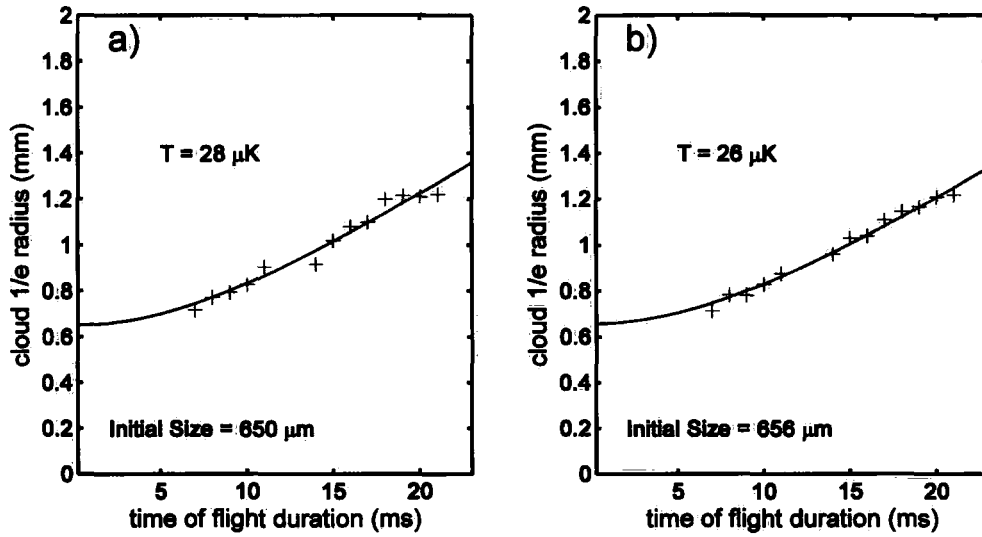


Figure 6.7: A typical set of time of flight data. a) and b) show the fit of equation 6.8 to the cloud image sequence in the x and y directions respectively after a MOT loading time of 1 s and a molasses duration of 12 ms. $|\Delta|=(2\pi)60$ MHz.

6.6 Characterisation of the Optical Molasses

Once the temperature measurement techniques were performing reliably, we conducted a study of the optical molasses. A typical experimental cycle proceeded as follows: both MOTs were run simultaneously until the atom number in the second MOT reached a pre-set value. The LabVIEW routine was then triggered and immediately turned off the pyramid MOT coils and shuttered off the pyramid MOT light. The second MOT was held for 100 ms before the optical molasses phase began. The MOT coils were turned off and simultaneously the detuning of the master light increased in magnitude and the intensity of the repump light reduced to 10% of its original value. The repump was extinguished completely 4 ms before the end of the molasses sequence thus depumping the atomic population to the lower hyperfine state and increasing the density of the cloud [151, 152]. All light was then extinguished and the atoms were imaged after a period of free expansion. The temperature of the atom cloud as a function of molasses duration was investigated. The results are shown in figure 6.8. We found that the

temperature decreased with time until around 12 ms after which there was no observed decrease. Henceforth we used a molasses duration of 12 ms for our experiments.

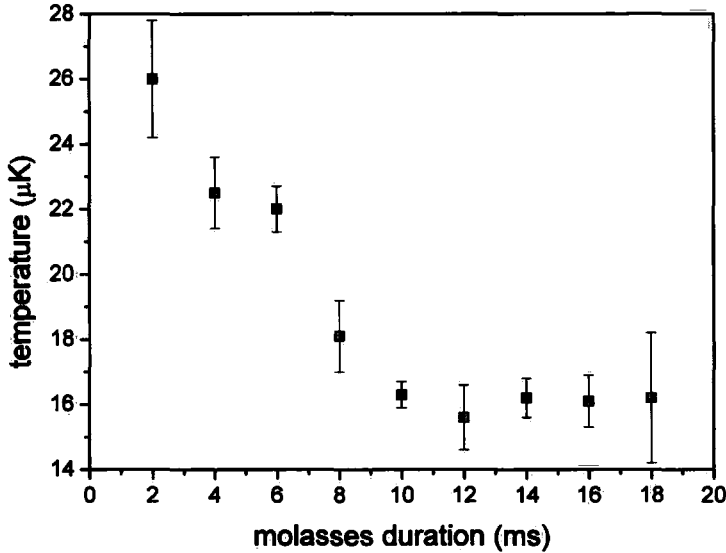


Figure 6.8: The measured temperature of the atom cloud for increasing molasses duration. $|\Delta| = (2\pi) 60$ MHz. MOT loading time = 1 s. Each point is the mean of 8 measurements. The error bar is the standard error of the mean.

Studies conducted by other groups [80, 153] have found that the temperature of optical molasses varies as I/Δ . We tested our optical molasses by plotting the temperature of our atom cloud as a function of the dimensionless light-shift parameter

$$\frac{\Omega}{|\Delta|\Gamma} = \frac{\Gamma}{2\Delta} \times \frac{I}{I_s}. \quad (6.12)$$

Here Ω is the Rabi frequency, Δ is the detuning from resonance, Γ is the linewidth of the transition, I is the laser intensity and I_s is the saturation intensity. The plot can be seen in figure 6.9. The data was fit to the equation [153]

$$\frac{k_B T}{\hbar\Gamma} = C_0 \frac{\Omega^2}{|\Delta|\Gamma} + C_1, \quad (6.13)$$

where C_0 is the slope and C_1 the temperature intercept. From our data we measured a value for C_0 of 0.43 ± 0.03 . The error quoted arises from

the weighted least-squares fit to the data. Our value for C_0 is in excellent agreement with the value of 0.46 ± 0.02 measured by Wallace *et al.* [153].

The limits of our experimental setup prevented us from extending the investigation beyond 64 MHz or reducing the laser intensity in controlled steps.

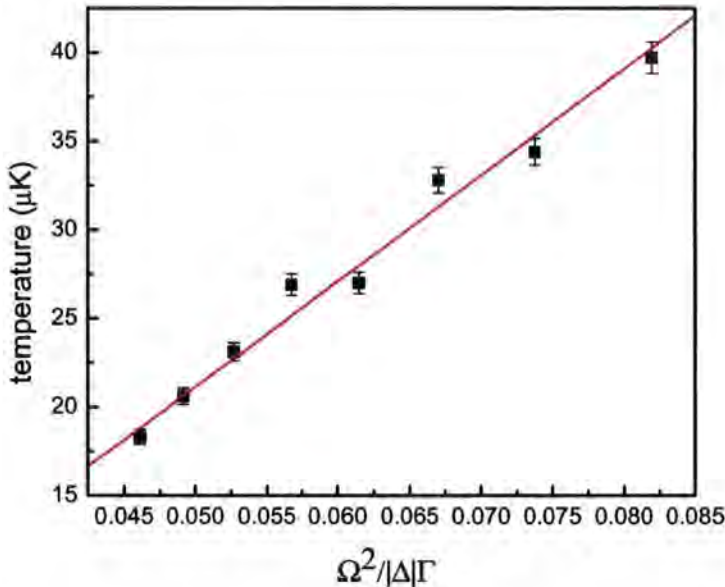


Figure 6.9: The measured temperature of the atom cloud against the dimensionless light-shift parameter. For a total $I/I_s=30$. Each point is the mean of 8 measurements. The error bar is the standard error of the mean. The red line is a weighted straight-line fit to the data.

6.7 Summary of the Experiment

The experimental setup described in this chapter was essentially built up from scratch since July 2005. The laser cooling apparatus for both MOTs and a time of flight sequence was developed to image the atom cloud after its release from the MOT. Optimisation of the pyramid MOT was performed and its flux measured. An investigation into the temperature dependence of the atoms in the science chamber on variable experimental parameters was conducted.

Once the laser cooling experiment was performing reliably we could progress to implementing the CO₂ laser trap. This is the subject of the following chapter.

Chapter 7

CO₂ Laser

7.1 Introduction

The CO₂ laser that was used in this work was a Coherent DEOS GEM Select 100. The principle of operation of a CO₂ laser is not discussed in detail here as it is covered in many textbooks, e.g. reference [154]. Briefly, there is a mixture of CO₂, N₂ and He gases contained between electrodes in the gain region of the cavity. An RF field is applied between the electrodes which creates a discharge. The first vibrational mode of the N₂ molecules (which has a very large excitation cross-section) is excited. This state is metastable and close in energy to the first asymmetric stretch mode of the CO₂ molecules. The CO₂ molecules are excited due to collisions with the N₂ (collisions are augmented by the presence of the He). The first asymmetric stretch mode of the CO₂ molecules decay to the first symmetric stretch mode, resulting in laser output at a wavelength of 10.6 μm . The laser produces a single mode, horizontally polarised beam with a power of 100 W.

7.2 Using the CO₂ Laser

Adding the CO₂ laser into the existing experimental setup required great care and preparation. As well as the necessity of ZnSe optics discussed in section 4.4.2, it is necessary to water cool the laser itself, its power supply, the AOMs (which receive 40 W of RF power) and the laser power meter.

The laboratory door was interlocked such that the laser would shut down immediately should the door open. The interlock was also connected to flow meters in the water cooling circuit to prevent overheating should the water pressure drop. When not in alignment mode, the beam path was completely enclosed. Points in the beam path of very high intensity (such as the foci of telescopes) were enclosed in pipes. The CO₂ laser is pumped by an 2kW RF D1000L power supply. The RF supply is in turn powered by a 35V, 60A Agilent 6573A DC power supply.

7.2.1 Installation

The CO₂ laser was secured to a platform which was mounted above some of the second MOT optics adjacent to the vacuum chamber, see figure 7.1. The use of this platform was necessary to raise the laser beam path up to the required height and also due to the lack of space on the optical table on which to place the laser directly. The output beam of the laser was measured (using knife-edge measurements, see section 7.2.2) to have a $1/e^2$ radius of 1.8 ± 0.2 mm and a divergence of 4.2 mrad. This was in agreement with the technical specifications provided for the laser [155].

7.2.2 Beam Profiling

Knife-edge measurements [156] are a way of measuring the size of a laser beam by measuring the power drop at a detector as a function of the position of a sharp opaque blade moving across the path of a laser beam. When performing measurements on high power CO₂ laser beams the blade used must be sufficiently robust to withstand the laser radiation. Also, any reflections from the blade must be blocked. A schematic of the knife-edge measurement setup employed for the CO₂ laser is shown in figure 7.2.

Another way of measuring the profile of a CO₂ laser beam is to use a specialist beam sampler. During a demonstration of a Spiracon BPS beam sampler the transverse mode of our laser was measured in the near field, directly after the laser output. A false colour image of the beam profile can be seen in figure 7.3. We found that this commercial profiler was cumbersome to use and fringes

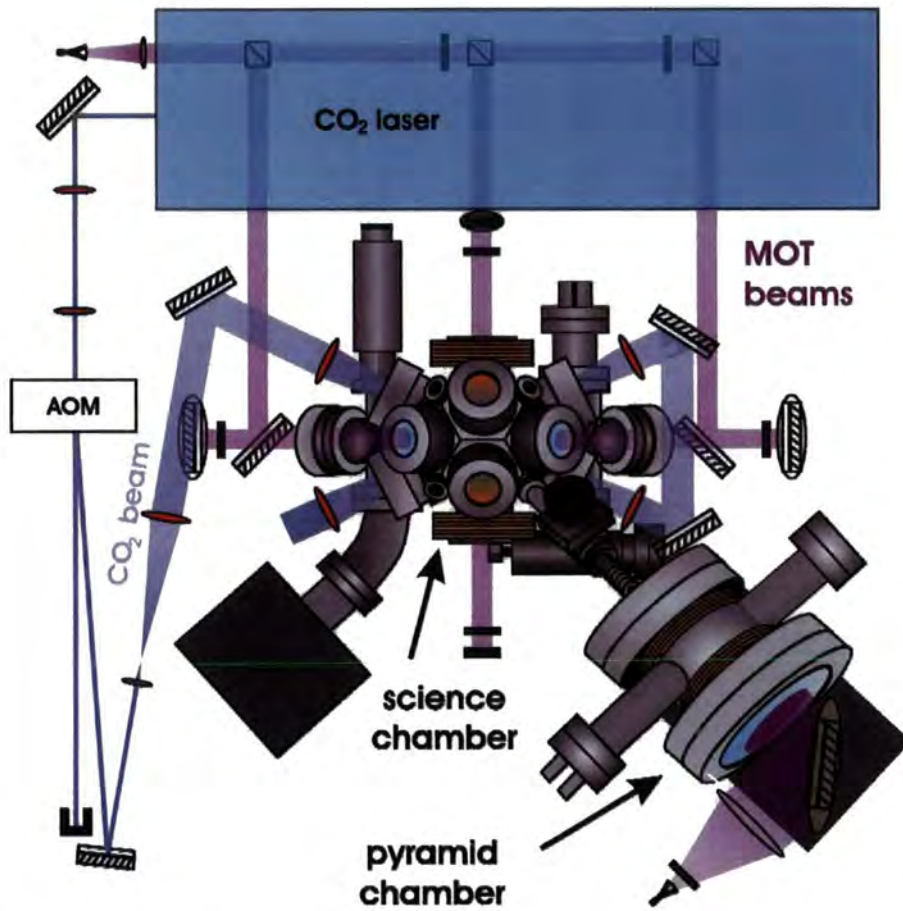


Figure 7.1: Schematic of the intended CO₂ laser beam path. The position of the CO₂ laser and its optics in relation to the vacuum chamber. The orange elements represent ZeSe optics.

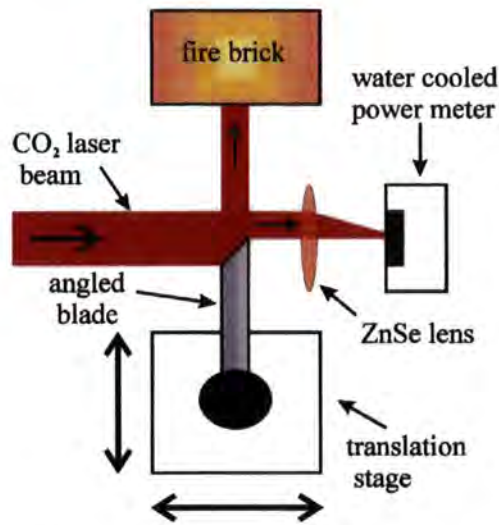


Figure 7.2: Experimental setup for profiling the CO₂ laser beam. The lens is necessary for measuring large diameter beams.

were present on the beam profile images which were not on the beam itself.

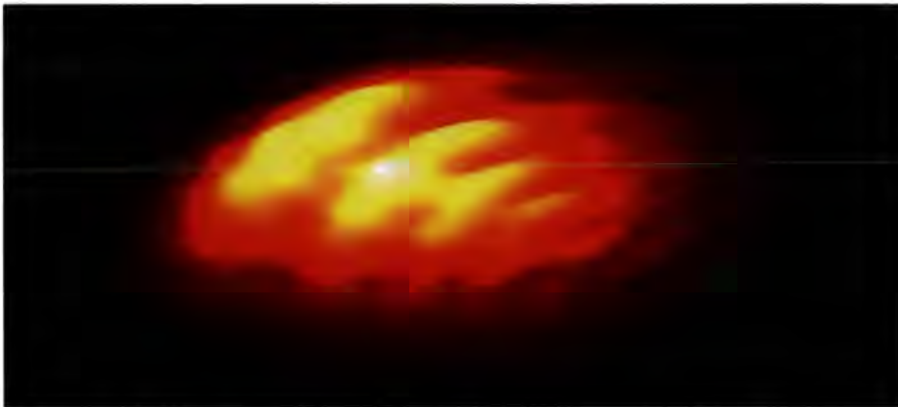


Figure 7.3: False colour image of the CO₂ laser beam profile. The stripes in the profile are due to the measuring instrument.

7.2.3 Initial Alignment

To convey the CO₂ laser beam to the experiment, the output beam was reflected through 90° before being telescoped down in size using a 7:4 telescope, thus allowing >98% transmittance of the beam through the input aperture of

the AOM. The zero order beam from the AOM was reflected 90° downwards into a heatsink beam block located on the optical table surface. The optimised first order diffracted beam was reflected back towards the chamber, see figure 7.1. At this point the alignment of the CO₂ laser became more critical and also more difficult to achieve because of space restrictions. The following section outlines the methods employed to align the first order CO₂ beam from the AOM.

7.3 Methods of Alignment

Aligning the CO₂ laser was difficult and great care had to be taken. Because the radiation is of high intensity and in the far infrared, typical methods of beam detection were not accessible. The pointing stability from the AOM is critically dependent upon its temperature [108]. The diffracted beam takes about 5 minutes to reach thermal equilibrium, during which time the beam was deflected through ~5 mrad. For our experimental arrangement this results in a displacement of the beam spot at the chamber of 1 cm. For this reason the alignment of the beam was (in the most part) conducted at a full power of ~65 W.

7.3.1 Thermal Paper and Imaging Plates

The coarse alignment of the laser beam was performed using thermal paper. The paper turns black (or sets on fire) in the presence of strong thermal radiation. By placing a piece of thermal paper in the path of the beam we could locate the beam position. To align the laser through the vacuum chamber, the full power first order beam was blocked using a fire brick. Then a piece of thermal paper was adhered to a cap containing a small central hole and then the cap placed over the viewport. The beam path would then be unblocked briefly allowing a mark to be burned onto the paper. Figure 7.4 shows a progression of paper pieces used to align the laser beam. Moving left to right then top to bottom we can see how the burn pattern becomes closer to the desired beam path (indicated by the small hole in the thermal paper) as successive iterations are made to the optical alignment.



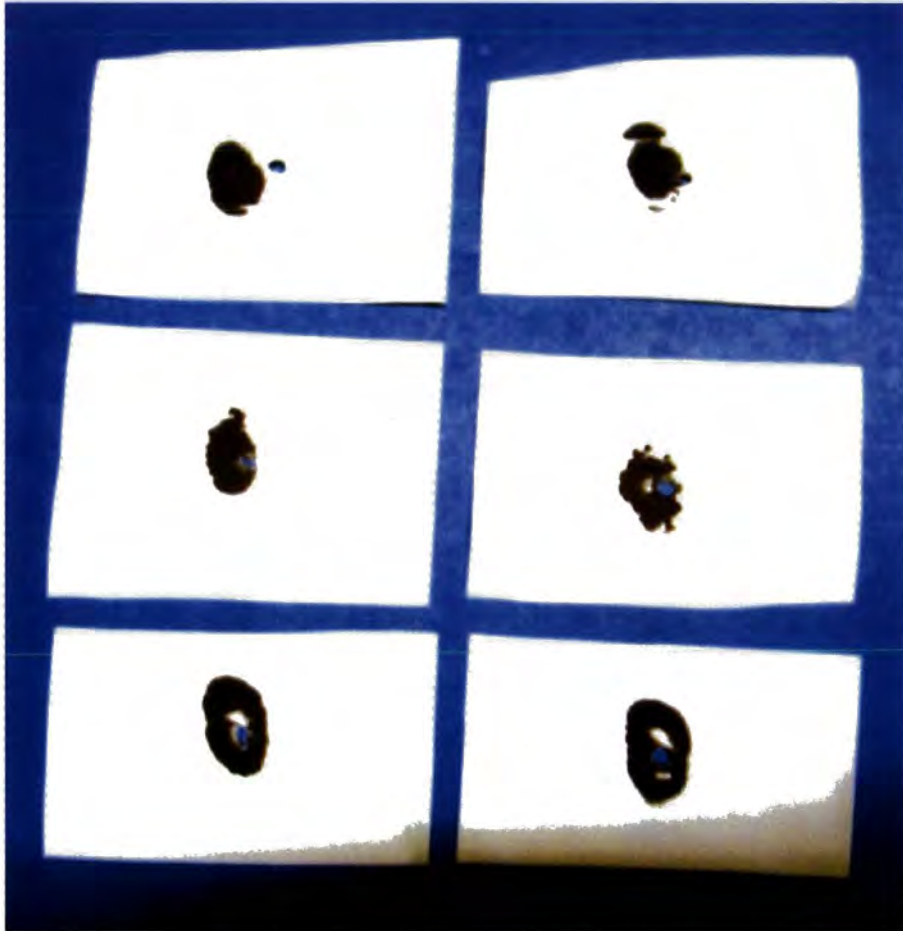


Figure 7.4: Progression of used thermal paper pieces. The burn pattern gets closer to the center (blue dot) with each iteration of the beam alignment.

Another useful tool for detecting the coarse position of the beam was a Macken Instruments phosphorescent plate [157]. When illuminated with UV radiation, the plate glows yellow. In positions where the CO₂ laser beam is incident on the plate the phosphorescent glow is suppressed and a dark patch observed. An photographic example of this can be seen in figure 7.5.

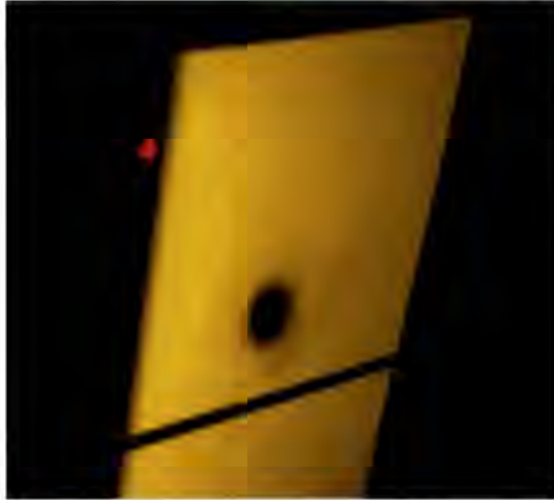


Figure 7.5: Using a thermal imaging plate to locate the CO₂ laser beam. The laser spot appears as a black mark on a fluorescent yellow background.

Once coarse alignment of the CO₂ laser beam through the chamber was achieved, more sensitive methods of alignment were adopted.

7.3.2 Resonant Tracer Beam

A resonant tracer beam was used for fine alignment. This beam was provided by a Toptica DLX laser at a wavelength of 780 nm. The beam was overlapped with the CO₂ laser beam using a ZeSe combining slide after the AOM. The slide reflects only about 30% of the 780 nm light and so a beam with power of around 250 mW was used. Once the beams were overlapped over a distance of several meters, adjustments to the beam path were made using the 780nm light alone. The schematic of the setup for this tracer beam can be seen in figure 7.6. The 780 nm beam was centered through the ZeSe viewports on the science chamber and we found that the MOT could be blown away by sweeping the beam's frequency through resonance.

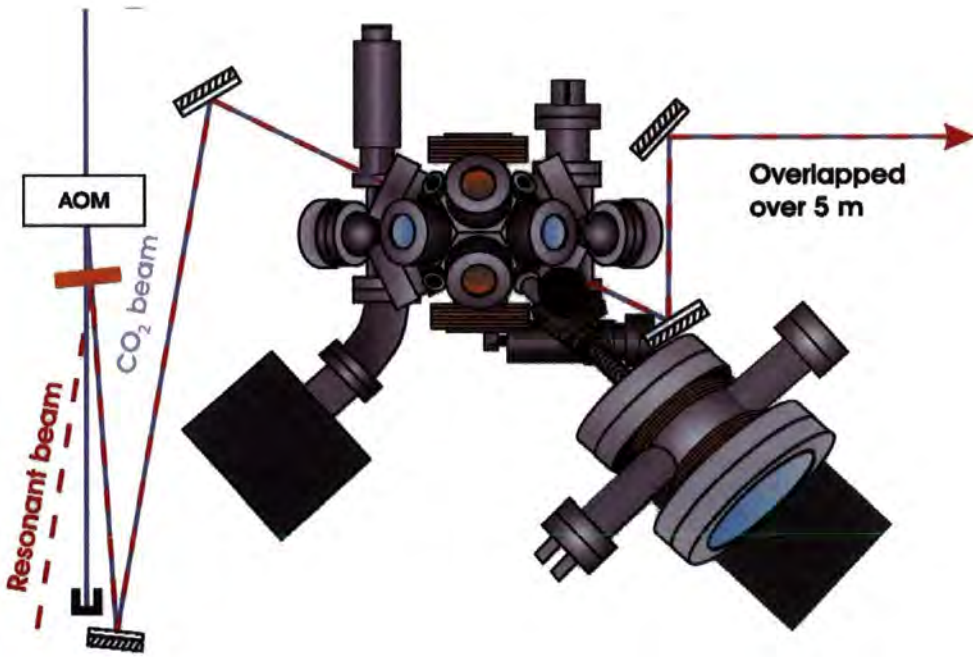


Figure 7.6: Schematic of the tracer beam setup. A 780 nm beam is overlapped with the CO₂ laser beam so that adjustments to the beam path can be made with the CO₂ laser turned off.

For our experimental configuration (requiring a CO₂ beam focus at the centre of the science chamber), the shortest available focal length lens that we could use outside the vacuum chamber was $f = 15$ cm. We then took account of the other available lens focal lengths and decided on using a 1:4 expanding telescope to enlarge the beam diameter to 10 mm. This results in $\ll 1\%$ loss of beam power on a 2" diameter lens and a $< 1\%$ Fresnel ripple from hard-edged truncation of the beam from the lens holder [158]. From Gaussian beam optics, for a collimated beam of $1/e^2$ radius R , and wavelength λ , focused by a lens of focal length f , the beam waist w_0 is given by [105],

$$w_0 \approx \frac{f\lambda}{\pi R}. \quad (7.1)$$

From this expression we calculated that by using a input beam radius of 10 mm we achieve a beam waist of 50 μm hence this is the value we adopted for the numerical modeling of chapter 3.

For a number of reasons we found difficulty in aligning the tracer beam once the expanding telescope was inserted. Firstly, the 780 nm beam was attenuated by the ZnSe optics resulting in a weak and difficult to see beam. Also, reflections from the front and back face of the combining slide were present resulting in a smeared beam spot. The tracer beam was aligned as well as possible and then focused into the centre of the science chamber. Fine adjustment of the focusing lens was achieved using a micrometer-adjusted 3-axis translation stage. We observed the focus of the beam by blowing away only the centre of the MOT. Placing the expanding telescope between two steering mirrors is a far from optimum arrangement but was necessary in this case as there was not space to place it elsewhere.

7.4 Search for the Dipole Trap Signal

Once the tracer beam was focused on to the MOT we assumed that the focus of the CO₂ beam would be in close proximity. Hence we began to search for signatures of a dipole trap using various methods. The input CO₂ beam was focused into the science chamber and the emerging output beam focused onto the power meter and used as a diagnostic.

7.4.1 Time of Flight Technique

Initially we began the search for the dipole trap signal by using a standard time of flight technique similar to that described in section 6.5.2. In this case however, we allowed over 35 ms of ballistic expansion so that the vast majority of atoms from the MOT had fallen away under gravity and out of the field of vision of the camera. The CO₂ laser was left on for the duration of the experimental cycle and then turned off only when the fluorescence imaging pulse was applied. We expected to see fluorescence from atoms trapped in the CO₂ beam after the rest of the MOT has dissipated but no signal was observed. Next, an experimental cycle was initiated so that a time of flight image was taken every 1.5 s and displayed on a monitor. The focusing input lens for the CO₂ beam was then translated through an x, y, z grid covering a cubic centimeter in steps of 0.5 mm. No signal was observed for the > 1000 lens positions adopted and so we moved on to try alternative methods.

7.4.2 Anti-Trap Signal

During previous work [49–51] we observed the dipole trap signal by making use of the difference in polarisability of the $5S$ and $5P$ states. The technique was implemented as follows, The MOT was made as large and diffuse as possible by reducing the B-field gradient to around 1 G/cm and reducing the magnitude of the detuning to less than 5 MHz (as close to resonance as possible without experiencing excessive flickering of the MOT). The CO₂ laser was then turned on. In the region of the CO₂ beam focus, the atoms experience a much greater light-shift in the excited state than the ground state and the atoms will experience blue detuned MOT light and be heated from the trap. This is illustrated in figure 7.7. For our beam parameters we expect a differential light-shift of over 30 MHz at the focus of the CO₂ beam. The focus of the dipole trap then shows as a dark stripe in a light background which can be seen to move as the input lens is adjusted. In this work we used this technique for several days without seeing any evidence of the dipole trap.

A variation on this technique was also implemented where a cycle was im-

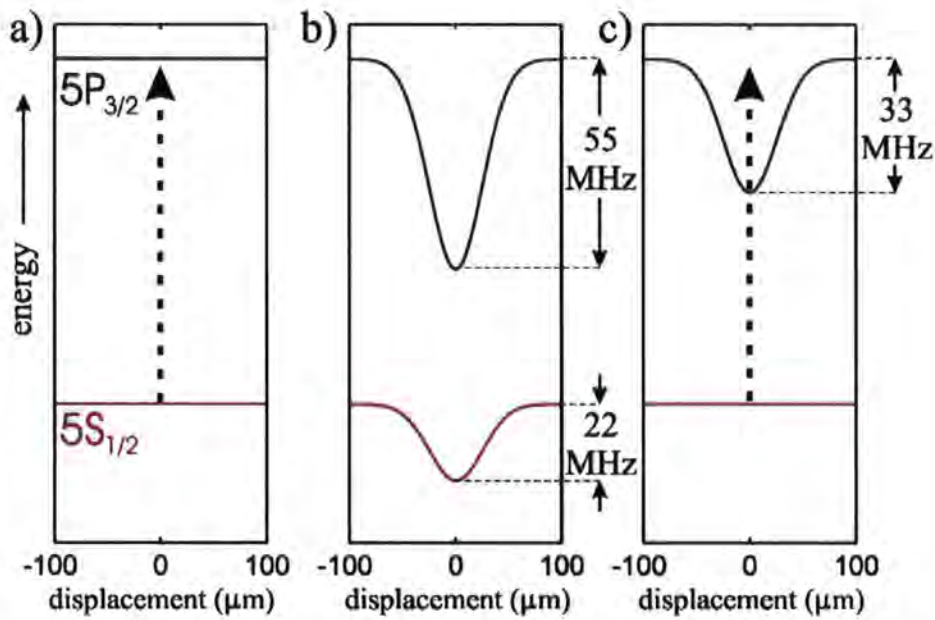


Figure 7.7: Principle of anti-trap technique. a) The atomic energy levels in free space, the laser cooling beam is red detuned. b) The CO₂ laser light creates a light-shift in the ground and excited states. c) The atomic transition energy in the CO₂ beam, the laser cooling light is blue detuned at the centre of the beam.

plemented to step the detuning of the laser from above resonance (so that no atoms were trapped in the MOT) to four linewidths below resonance in the hope that atoms would preferentially load into the region of the MOT overlapped with the CO₂ beam. We would expect then to see a light stripe on a dark background. No evidence for this was observed.

7.5 Possible Reasons for Null Result

In the search for the dipole trap signal we believe that there are two possibilities for the null results achieved thus far: firstly, we have achieved a dipole trap and our detection techniques are not sensitive enough to observe it. Second, we have not been able to overlap the CO₂ laser beam focus with the MOT.

We will begin with the first possibility; the detection techniques are not sensitive enough. For the time of flight technique we are confident that even small numbers of atoms ~ 1000 can be detected as we have imaged small atom numbers directly from the MOT. However, we are not able to tell if the CO₂ laser turns off as desired (shuttered by the AOM) during the imaging pulse because we do not have a fast enough detector for use with 10.6 μm radiation. If the CO₂ laser remains on, this would lead to a much reduced imaging contrast as the imaging light frequency experienced by the atoms would not be on resonance if they were still in the trap. For the anti-trap technique it is feasible to suggest that the signal, if present, could be missed easily as the search is conducted in real time and by eye.

The second possibility; no overlap between the CO₂ beam focus and the MOT. Around the science chamber, there is little space in which to make measurements on the CO₂ beam. Since the refractive index of the ZeSe is dependent on wavelength, refraction will cause deflection of the CO₂ beam relative to the tracer beam if the lenses are not centered perfectly. This could lead to the CO₂ beam path being offset from its assumed position. If this is the case, the beam position could fall outside the volume we have searched. Also, downstream from the expanding telescope the Rayleigh range of the CO₂ laser beam is so large that we could not measure changes in the beam size

above the uncertainty in the knife-edge measurements over the measurement length available (~ 10 cm). As a result of this we have no measure of the divergence of the CO_2 beam when it reaches the input lens and we cannot calculate (and correct for) the expected shift in position of the focal plane from $ABCD$ matrices [104] or using the method of Self [159]. This could also make the focus of the CO_2 laser beam fall outside of our search volume.

We believe that the second possibility is probably the most likely and that if we expand the volume of our search parameters, then we will eventually see the dipole trap signature. Work to achieve this is ongoing. The next chapter discusses other planned and ongoing work to improve the current experimental setup and also outlines plans for future experiments using the apparatus described in this thesis.

Part III

The Future

Chapter 8

Discussion and Future Directions

This chapter describes the intended future developments of this experiment. We will first discuss ways in which the current experimental setup will be extended and then discuss ways in which it can be improved upon. The final section comprises a list of further experiments we may wish to perform.

8.1 Discussion

As discussed in the previous chapter, detecting the CO₂ laser beam has proved to be a far from trivial exercise. This puts into perspective the extension of the experiment to a 1D (or 3D) optical lattice. As alignment of one beam into the chamber has proved difficult then it follows that focusing the beam through the chamber four times could prove very difficult indeed. Let us return to the two possible reasons for this difficulty as described in the previous chapter.

If the problem with trap alignment proves to be due to the lack of sensitivity of the detection technique, then once resolved, finding a second (or third or fourth) beam focus should not prove much more difficult than finding the first.

However, for the more likely situation in which the problem with trap align-

ment is due to the unknown location of the focus of the input beam, we may need to adopt a new strategy. It is clear that we need to gain better characterisation of the CO₂ laser beam before it reaches the input lens. One possibility to help achieve this is to make use of a manual, rotating brewster-angle CO₂ laser beam attenuator [160]. We could then attenuate the beam without deflecting it and perform knife-edge measurements without the need for bulky beam blocks. Another option is to ‘unfold’ the beam path into an area of the optical table in which we have more space. We could then perform measurements on the beam before reverting to the original setup.

Once the problems with trap alignment are overcome we will look to improving certain other aspects of the current setup.

8.2 Improvements to the Current Setup

8.2.1 Absorptive Imaging

A real drawback to the current experimental setup is the fluorescence imaging technique employed. The shortest imaging duration that we were able to use whilst maintaining a reasonable signal to noise ratio was 80 μ s. The signal to noise problem is worsened by the fact that we cannot integrate through the fluorescence images as explained in section 6.5.2. We have shown in section 6.5.2 that the heating experienced by the atoms for this imaging duration causes blurring to the image. This will be catastrophic when trying to resolve individual lattice sites. Using absorptive imaging instead is the obvious alternative as it uses a short exposure ($<10 \mu$ s) of low intensity ($I/I_s \approx 0.1$) light [161] and so the heating will be negligible. Space restrictions prohibit absorptive imaging being implemented using the imaging optics currently in place. However, in principle an absorptive imaging beam could be overlapped with one of the MOT beams. This absorptive imaging beam would have to be circularly polarised with opposite helicity to the MOT beam and separated from the MOT using polarisation optics once it has passed through the science chamber.

8.2.2 Imaging Optics

An objective lens for resolving individual sites in the CO₂ laser lattice has been designed and built by M. Pritchard. The lens was based upon the method of Alt [162] and the performance of which is covered in the thesis of M. Pritchard [163]. Briefly, the resolution of the lens was designed to be better than 2 μm . Unfortunately, the lens did not perform as well as was hoped with a resolution of 6 μm and a revised imaging setup will be necessary to achieve the resolution and magnification we require. Scheunemann *et al.* used a confocal microscope with a magnification of 40 to achieve a pixel resolution of <1 μm [44]. We intend to adopt a similar setup for our future work.

8.2.3 RF Power Compensation for the CO₂ laser AOM

If we need to perform evaporative cooling in the CO₂ lattice then the problem of temperature dependent beam steering from the AOMs discussed in chapter 7 will need to be overcome. This could be achieved by adding a second off-resonant frequency component to the RF signal supplied to the AOM crystal. As the amplitude of the resonant component is decreased, the off-resonant component is increased accordingly such that the total power absorbed by the crystal (and hence the crystal temperature) remains constant. Modifications to the RF electronics within the AOM driver will have to be made. We expect that to image atoms in individual lattice sites, evaporative cooling will be required, as was the case for Scheunemann *et al.* [45]. Another option would be to automate a manual CO₂ attenuator of the type mentioned in section 8.1.

8.3 Future Experiments

Here we will allude to certain future directions of the experiment that we may wish to investigate:

- **Raman Beam Generation:** We have begun work on generating Raman beams to couple groundstate hyperfine levels in ⁸⁷Rb. This cou-

pling will be necessary to initiate qubit states in our QIP scheme. Using a single frequency diode laser we use an electro-optic modulator to generate sidebands on the beam at a frequency of 6.8 GHz. This corresponds to the groundstate hyperfine splitting. We then injection lock a slave laser to the upper sideband averting the need for an interferometer to separate out the frequencies [164]. We can achieve a 12 mW beam at the sideband frequency with a better than 20 dB attenuation of the carrier. Expected two-photon Rabi frequencies are of the order of 1 GHz. This work has been principally carried out by M. Bason.

- **State Selective Transport:** This is a necessary step in the journey towards executing quantum gates in the CO₂ laser lattice. For an atom experiencing circularly polarized light the degeneracy of the magnetic sub-levels is lifted and the atom experiences a light-shift which depends on the wavelength of the laser and upon its magnetic quantum number m_F and is interpreted in terms of a ‘fictitious magnetic field’ [165]. We may choose to use an optical tweezer [166] to move atoms between neighboring lattice sites, depending on which state they occupy. If we define two qubit states as different magnetic levels of the Rb ground term then we can then use a wavelength at which one qubit state experiences a light shift and the other does not (for example at $\lambda \approx 785$ nm, where the polarisability of groundstate Rb changes sign between the D1 and D2 resonances).
- **Light Shift Engineering Revisited:** We could improve the resolution and simplicity of our light shift engineering technique [49, 50] by using a diode laser instead of a Nd:YAG laser to create the auxiliary field. By detuning to the red of the 5P_{3/2} to 5D_{5/2} transition in Rb at 776 nm we could load selected lattice sites with greater resolution and using less laser power.
- **Light-Induced Evaporation with Blue Light:** Another experiment that we would like to perform is light-induced evaporation from the CO₂ laser lattice. This could bypass the need to compensate the RF power to the CO₂ laser AOM. By using light from a frequency doubled high-power diode laser (Toptica TA-SHG 110) at around 421 nm we

can excite the $5S \rightarrow 6P$ transition. For Rb the polarisability of the $6P$ state is 38 times greater than that of the $5S$ state at the CO_2 laser wavelength [48], and so we believe that we could selectively heat only the hotter atoms at the edges of the lattice sites. It is feasible that by chirping the frequency of the light we could gradually remove all but the coldest atoms from the lattice.

- **Phase Modulated Lattice:** In a collaboration with the adaptive optics group of G. Love, we intend to produce a moving optical lattice by using two beams overlapping at a shallow angle. A liquid Crystal cell [167] will be used to introduce a phase shift to one of the beams. Using $\lambda \approx 785$ nm beams crossing at $\sim 16^\circ$ produces a structure with a similar periodicity to the CO_2 laser lattice. The state-selective transport technique mentioned earlier may be attempted using this 'optical conveyer belt'. Initial tests suggest that the lattice structure can be reliably controlled to $< 1 \mu\text{m}$ and moved by tens of microns in times on the order of 10 ms. This work has been carried out by J. Taylor.

Chapter 9

Conclusion

In summary, during the course of this work we have designed and constructed an experiment to laser cool Rb atoms and load them into a CO₂ laser optical lattice. Numerical modeling of the optical potentials that we expect to produce from the CO₂ laser lattice has been performed and the relevant experimental parameters such as trap depth and oscillation frequency deduced from them.

The experimental work began with the development of lasers for use in laser cooling. Successive iterations in design have led to a compact, stable and reliable laser system which has since been adopted by other researchers. Further to that, a double vacuum chamber system incorporating some novel features was constructed and home-made UHV viewports used. The lifetime of the atoms in the MOT suggests a vacuum pressure of less than 10^{-10} Torr within the science chamber. We have successfully implemented a double MOT system that performs reliably and we have compared our laser cooling performance to that of other researchers. We have attempted to implement a CO₂ laser optical dipole trap and despite trying several methods of detection we have so far not succeeded. Possible reasons for the null result were discussed. Also, limitations of the experiment have been identified and suggestions made for carrying out improvements. Other experiments that we propose to carry out on the apparatus have been briefly outlined.

We believe that neutral atoms in optical lattices offer an excellent testing-ground for developing quantum control techniques and present a promising

paradigm for quantum information processing. We have made significant progress towards these ends by developing an experimental framework in which to perform QIP experiments.

Part IV

Appendices

Appendix A

A Note on Polarisability

In the literature, polarisability values are most often quoted in ‘atomic’ units (a.u.). In these fundamental units the polarisability has units of volume but care has to be taken to distinguish if the values are quoted in Angstrom, $\text{\AA}^3 = 10^{-24}\text{cm}^3$ or Bohr radii, $a_0^3 = 0.14818 \text{\AA}^3$. In SI units the polarisability is defined from the relationship between the induced dipole moment and the applied field and hence has units of Cm^2/V . Hence in terms of atomic units $1 \text{ a.u.} = (4\pi\epsilon_0 a_0^3) = 0.16487 \times 10^{-40} \text{ Cm}^2/\text{V}$

The scalar polarisability $\alpha_0 = (\alpha_{xx} + \alpha_{yy} + \alpha_{zz})/3$

The tensor polarisability $\alpha_2 = (\alpha_{xx} - \alpha_{zz})/3$

For spherically symmetric states $\alpha_{xx} = \alpha_{yy} = \alpha_{zz}$ so $\alpha_2 = 0$

Appendix B

Light-Shifts for the Two-Level Atom

Here we derive in full the light shifts for a two-level atom using time dependent perturbation theory. The derivation can be found outlined in many sources (such as references [3, 76, 77]).

The time-dependant Schrödinger equation of an atom in a laser field reads,

$$i\hbar\frac{\partial\Psi}{\partial t} = H_{\text{at}}\Psi(\mathbf{r}, t) + V(\mathbf{r}, t)\Psi(\mathbf{r}, t), \quad (\text{B.1})$$

where H_{at} is the atomic Hamiltonian

$$H_{\text{at}} = -\frac{\hbar^2}{2m}\nabla^2 + V_{\text{at}}(r), \quad (\text{B.2})$$

with $V_{\text{at}} = -e^2/(4\pi\epsilon_0 r)$ and $V(\mathbf{r}, t) \equiv e\mathcal{E}(t)\cdot\mathbf{r}$ is the interaction potential.

We denote the eigenfunctions and eigenenergies of H_{t} as ϕ_k and E_k such that

$$H_{\text{at}}\phi_k(\mathbf{r}) = E_k\phi_k(\mathbf{r}), \quad (\text{B.3})$$

and we assume that the eigenfunctions are orthogonal and normalized according to

$$\int \phi_n^*(\mathbf{r})\phi_k(\mathbf{r})d\mathbf{r} = \delta_{nk}. \quad (\text{B.4})$$

We can write the wavefunction of the atom in the field as a linear superpo-

sition of the eigenfunctions ϕ_k , since they form a complete set:

$$\Psi(\mathbf{r}, t) = \sum_k c_k(t) \phi_k(\mathbf{r}) e^{-iE_k t/\hbar}. \quad (\text{B.5})$$

The coefficients of the superposition, the function $c_k(t)$, have an important physical meaning: *the probability that the atom is in the eigenstate k at time t is $|c_k(t)|^2$.*

Substituting in equation B.1 Ψ by the right-hand side of equation B.5 results in a system of differential equations for the coefficients $c_k(t)$:

$$\begin{aligned} & \sum_k i\hbar \dot{c}_k(t) \phi_k e^{-iE_k t/\hbar} + \sum_k c_k(t) E_k \phi_k e^{-iE_k t/\hbar} \\ &= \sum_k [H_{\text{at}} + V(\mathbf{r}, t)] c_k(t) \phi_k e^{-iE_k t/\hbar} \\ &= \sum_k c_k(t) E_k \phi_k e^{-iE_k t/\hbar} + \sum_k V(\mathbf{r}, t) c_k(t) \phi_k e^{-iE_k t/\hbar}. \end{aligned} \quad (\text{B.6})$$

Canceling like terms gives,

$$\sum_k i\hbar \dot{c}_k(t) \phi_k e^{-iE_k t/\hbar} = \sum_k V(\mathbf{r}, t) c_k(t) \phi_k e^{-iE_k t/\hbar}. \quad (\text{B.7})$$

Now we multiply both sides of this last equation by the complex conjugate of each eigenfunction in turn, and integrate over space. Using equation B.4, we find

$$i\hbar \dot{c}_n(t) e^{-iE_n t/\hbar} = \sum_k V_{nk}(t) c_k(t) e^{-iE_k t/\hbar}, \quad (\text{B.8})$$

where the $V_{nk}(t)$ are the matrix elements of the dipole operator:

$$V_{nk}(t) = \int \phi_n^*(\mathbf{r}) V(\mathbf{r}, t) \phi_k(\mathbf{r}) d\mathbf{r} = \langle \phi_n | V | \phi_m \rangle. \quad (\text{B.9})$$

Note that $V_{nn} = 0$, since $V(\mathbf{r}, t)$ is odd for $\mathbf{r} \rightarrow -\mathbf{r}$ while $|\phi_n(\mathbf{r})|^2$ is even.

Equation B.8 can be written in the slightly simpler form

$$i\hbar \dot{c}_n(t) = \sum_{k \neq n} V_{nk}(t) c_k(t) e^{i\omega_{nk} t}, \quad (\text{B.10})$$

by introducing the Bohr angular frequency

$$\omega_{nk} \equiv \frac{(E_n - E_k)}{\hbar}. \quad (\text{B.11})$$

So far no approximations have been made and equation B.10 is exactly equivalent to the Schrödinger equation, equation B.1. We now restrict the analysis to two atomic states, the ground state and a single excited state which are coupled by the external field. The coupled equations are:

$$i\hbar \frac{dc_g}{dt} = c_g V_{ge} e^{-i\omega_0 t}; \quad i\hbar \frac{dc_e}{dt} = c_g V_{eg} e^{-i\omega_0 t}. \quad (\text{B.12})$$

Recall that $V(\mathbf{r}, t) \equiv e\mathcal{E}(t) \cdot \mathbf{r} = -\mathbf{d} \cdot \mathcal{E}$ and note that the spatial variation of the field is negligible over the size of the atom (the dipole approximation) $\mathcal{E} = \mathcal{E}_0 \cos \omega t$

We now define the Rabi frequency

$$\Omega = \frac{-e\mathcal{E}_0}{\hbar} \langle e | \mathbf{r} | g \rangle \quad (\text{B.13})$$

and define the matrix elements in terms of the Rabi frequency

$$\mathbf{e} \cdot \mathcal{E} = \frac{e\mathbf{r}}{2} \mathcal{E}_0 (e^{i\omega t} + e^{-i\omega t}) \implies V_{ge} = \frac{\hbar\Omega}{2} (e^{i\omega t} + e^{-i\omega t}) \quad (\text{B.14})$$

Substituting the matrix elements into equation (12) gives

$$\begin{aligned} i\hbar \frac{dc_g}{dt} &= \frac{c_e \hbar\Omega}{2} (e^{i\omega t} + e^{-i\omega t}) e^{-i\omega_0 t} \\ \implies i\hbar \dot{c}_g &= \frac{c_e \hbar\Omega}{2} (e^{i(\omega-\omega_0)t} + e^{-i(\omega+\omega_0)t}) \end{aligned} \quad (\text{B.15})$$

similarly

$$i\hbar \dot{c}_e = \frac{c_g \hbar\Omega}{2} (e^{-i(\omega-\omega_0)t} + e^{i(\omega+\omega_0)t}) \quad (\text{B.16})$$

Now we make the rotating wave approximation and drop the terms in $(\omega+\omega_0)$. (This is an excellent approximation when $\omega \approx \omega_0$) and define the detuning, $\Delta = \omega - \omega_0$ so,

$$i\hbar \dot{c}_g = \frac{c_e \hbar\Omega}{2} e^{i\Delta t}; \quad i\hbar \dot{c}_e = \frac{c_g \hbar\Omega}{2} e^{-i\Delta t}. \quad (\text{B.17})$$

We now need to define new variables to include the time dependency.

$$\tilde{c}_1 = c_2 \frac{\Omega}{2} e^{-i\Delta t/2}; \quad \tilde{c}_2 = c_1 \frac{\Omega}{2} e^{i\Delta t/2} \quad (\text{B.18})$$

Differentiating equations. B.18 with respect to time, and multiplying by i gives

$$i\dot{\tilde{c}}_1 = i\dot{c}_1 e^{-i\Delta t/2} + \frac{\Delta}{2} c_1 e^{-i\Delta t/2} \quad (\text{B.19})$$

$$i\dot{\tilde{c}}_2 = i\dot{c}_2 e^{i\Delta t/2} - \frac{\Delta}{2} c_2 e^{i\Delta t/2}. \quad (\text{B.20})$$

Substituting in equations B.17 and B.18 into these differential equations yields,

$$i \dot{\tilde{c}}_1 = \frac{1}{2} (\tilde{c}_1 \Delta + \tilde{c}_2 \Omega) \quad (\text{B.21})$$

$$i \dot{\tilde{c}}_2 = \frac{1}{2} (\tilde{c}_1 \Omega - \tilde{c}_2 \Delta) . \quad (\text{B.22})$$

We can now combine Equations B.21 and B.22 and write them in matrix form

$$i \begin{pmatrix} \dot{\tilde{c}}_1 \\ \dot{\tilde{c}}_2 \end{pmatrix} = \begin{pmatrix} \frac{\Delta}{2} & \frac{\Omega}{2} \\ \frac{\Omega}{2} & -\frac{\Delta}{2} \end{pmatrix} \begin{pmatrix} \tilde{c}_1 \\ \tilde{c}_2 \end{pmatrix} . \quad (\text{B.23})$$

Now solving for the eigenenergies of the perturbed system gives,

$$E = \pm \frac{\hbar}{2} \sqrt{\Delta^2 + \Omega^2} . \quad (\text{B.24})$$

In the limit that $|\Delta| \gg \Omega$ the energies are

$$E = \pm \frac{\hbar}{2} \left(\Delta + \frac{\Omega^2}{2\Delta} \right) , \quad (\text{B.25})$$

or an energy shift of the electronic states of

$$\Delta E = \pm \frac{\hbar \Omega^2}{4\Delta} . \quad (\text{B.26})$$

The ground state is shifted down and the excited state shifted up.

Appendix C

Lorentz Oscillator Model

The optical *dipole* force can be derived by considering the Lorentz model of a classical oscillator. In terms of the complex polarisability α of the atom, the interaction potential can be expressed as

$$U = -\frac{1}{2}\langle \mathbf{b} \cdot \mathbf{E} \rangle = -\frac{1}{2\epsilon_0 c} \text{Re}(\alpha) I. \quad (\text{C.1})$$

The imaginary part of the polarisability results in absorption. The power of which can be expressed as

$$P_{ab} = \frac{\omega}{\epsilon_0 c} \text{Im}(\alpha) I \quad (\text{C.2})$$

The power absorbed is re-emitted and can be interpreted in terms of photon scattering. The rate of which is then given by

$$\Gamma_{sc} = \frac{P_{ab}}{\hbar\omega} = \frac{1}{\hbar\epsilon_0 c} \text{Im}(\alpha) I \quad (\text{C.3})$$

Now we need to find an expression for the polarisability. The equation of motion for an electron in an external field is given by

$$\frac{d^2x}{dt^2} + \Gamma_c \frac{dx}{dt} + \omega_0^2 x = -\frac{e}{m_e} \mathcal{E}(t) \quad (\text{C.4})$$

where Γ_c is the classical damping due to radiative energy loss and is given by the Larmor formula

$$\Gamma_c = \frac{e^2 \omega^2}{6\pi \epsilon_0 m_e c^3} \quad (\text{C.5})$$

Solving equation C.4 of motion gives an expression for x which can be equated to the polarisability, α , as

$$\alpha = 6\pi \epsilon_0 c^3 \frac{\Gamma/\omega_0^2}{\omega_0^2 - \omega^2 - i(\omega^3/\omega_0^2)\Gamma} \quad (\text{C.6})$$

and so using equations C.1 and C.3 we obtain expressions for the potential and the scattering rate.

$$U(\mathbf{r}) = -\frac{3\pi c^2}{2\omega_0^3} \left(\frac{\Gamma}{\omega_0 - \omega} + \frac{\Gamma}{\omega_0 + \omega} \right) I(\mathbf{r}) \quad (\text{C.7})$$

$$\Gamma_{sc} = \frac{3\pi c^2}{2\hbar \omega_0^3} \left(\frac{\omega}{\omega_0} \right)^3 \left(\frac{\Gamma}{\omega_0 - \omega} + \frac{\Gamma}{\omega_0 + \omega} \right)^2 I(\mathbf{r}) \quad (\text{C.8})$$

We have assumed that $\Delta \gg \Gamma$ and that there is negligible excited state population

Appendix D

Circuits

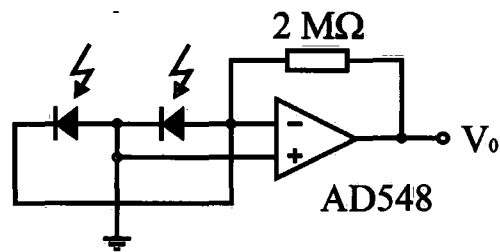


Figure D.1: Differential Photodiode circuit used to generate the polarisation spectrum and DAVLL signal.

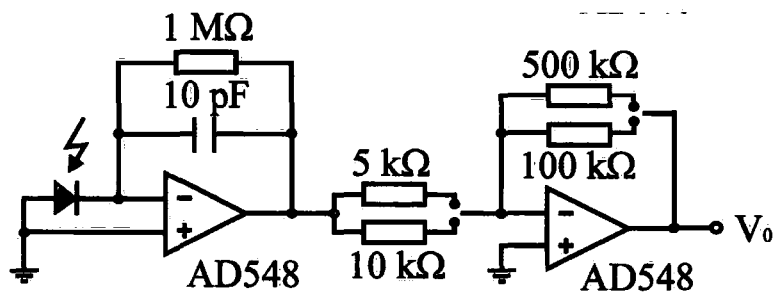


Figure D.2: Photodiode circuit used to collect fluorescence signal from the MOT.

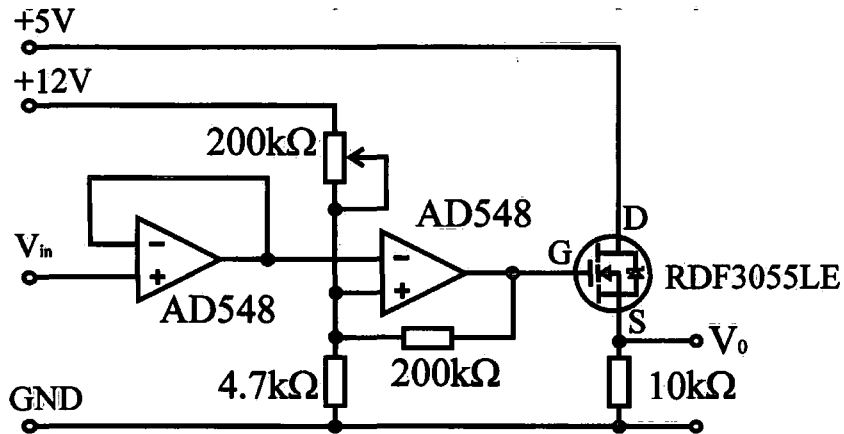


Figure D.3: Circuit used to trigger the experiment. The variable resistor sets a trigger point which is compared to V_{in} . A 5V TTL signal is output.

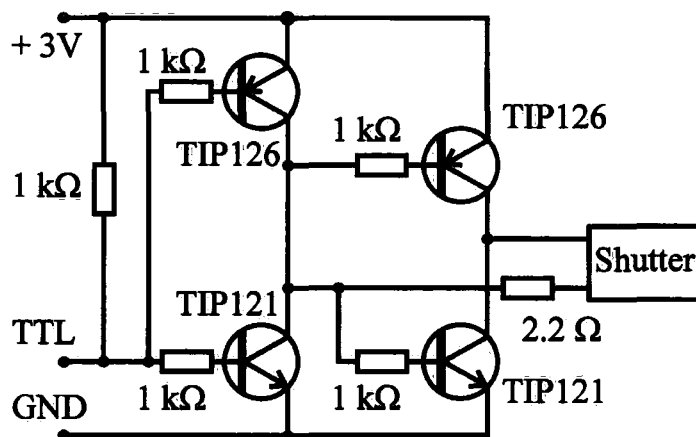


Figure D.4: Circuit used to drive the shutters.

Bibliography

- [1] C. S. Adams and E. Riis, *Laser Cooling and Trapping of Neutral Atoms*, Prog. Quant. Electron. **21**, 1 (1997).
- [2] C. J. Foot, *Laser Cooling and Trapping of Atoms*, Contemp. Phys. **32**, 369 (1991).
- [3] H. J. Metcalf and P. van der Straten, *Laser Cooling and Trapping* (Springer, 1999).
- [4] D. M. Stamper-Kurn *et al.*, *Optical Confinement of a Bose-Einstein Condensate*, Phys. Rev. Lett. **80**, 2027 (1998).
- [5] B. P. Anderson and M. A. Kasevich, *Macroscopic Quantum Interference from Atomic Tunnel Arrays*, Science. **282**, 1686 (1998).
- [6] M. Barrett, J. Sauer, and M. Chapman, *All-Optical Formation of an Atomic Bose-Einstein Condensate*, Phys. Rev. Lett. **87**, 010404 (2001).
- [7] T. Weber, J. Herbig, M. Mark, H.-C. Nägerl, and R. Grimm, *Bose-Einstein Condensation of Cesium*, Science **299**, 232 (2003).
- [8] Y. Takasu *et al.*, *Spin-Singlet Bose-Einstein Condensation of Two-Electron Atoms*, Phys. Rev. Lett. **91**, 040404 (2003).
- [9] T. Kinoshita, T. Wenger, and D. S. Weiss, *All-Optical Bose-Einstein Condensation using a Compressible Crossed Dipole Trap*, Phys. Rev. A. **71**, 011602 (2005).
- [10] B. DeMarco and D. S. Jin, *Onset of Fermi Degeneracy in a Trapped Atomic Gas*, Science. **285**, 1703 (1999).

-
- [11] S. R. Granade, M. E. Gehm, K. M. O'Hara, and J. E. Thomas, *All-Optical Production of a Degenerate Fermi Gas*, Phys. Rev. Lett. **88**, 120405 (2002).
- [12] H. Katori, M. Takamoto, V. Palchikov, and V. D. Ovsiannikov, *Ultra-stable Optical Clock with Neutral Atoms in an Engineered Light Shift Trap*, Phys. Rev. Lett. **91**, 173005 (2003).
- [13] M. Takamoto, F.-L. Hong, R. Higashi, and H. Katori, *An Optical Lattice Clock*, Nature **435**, 321 (2005).
- [14] N. Schlosser, G. Reymond, and P. Grangier, *Collisional Blockade in Microscopic Optical Dipole Traps*, Phys. Rev. Lett. **89**, 023005 (2002).
- [15] J. McKeever *et al.*, *State-Insensitive Cooling and Trapping of Single Atoms in an Optical Cavity*, Phys. Rev. Lett. **90**, 133602 (2003).
- [16] P. Staannum, S. D. Kraft, J. Lange, R. Wester, and M. Weidemüller, *Experimental Investigation of Ultracold Atom-Molecule Collisions*, Phys. Rev. Lett. **96**, 023201 (2006).
- [17] N. Zahzam, T. Vogt, M. Mudrich, D. Comparat, and P. Pillet, *Atom-Molecule Collisions in an Optically Trapped Gas*, Phys. Rev. Lett. **96**, 023202 (2006).
- [18] C. Chin *et al.*, *Observation of Feshbach-Like Resonances in Collisions between Ultracold Molecules*, Phys. Rev. Lett **94**, 123201 (2005).
- [19] K. I. Petsas, A. B. Coates, and G. Grynberg, *Crystallography of Optical Lattices*, Phys. Rev. A. **50**, 5173 (1994).
- [20] J. Stenger *et al.*, *Spin Domains in Ground-State Bose-Einstein Condensates*, Nature. **396**, 345 (1998).
- [21] A. Kaplan, M. F. Andersen, and N. Davidson, *Suppression of Inhomogeneous Broadening in rf Spectroscopy of Optically Trapped Atoms*, Phys. Rev. A. **66**, 045401 (2002).
- [22] M. V. Romalis and E. N. Fortson, *Zeeman Frequency Shifts in an Optical Dipole Trap used to Search for an Electric-dipole Moment*, Phys. Rev. A. **59**, 4547 (1999).

- [23] A. Ashkin, *Trapping of Atoms by Resonance Radiation Pressure*, Phys. Rev. Lett. **40**, 729 (1978).
- [24] R. Grimm, M. Weidemüller, and Y. B. Ovchinnikov, *Optical Dipole Traps for Neutral Atoms*, Adv. Atom. Mol. Opt. Phys **42**, 95 (2000).
- [25] C. Cohen-Tannoudji, J. Dupont-Roc, and G. Grynberg, *Atom-Photon Interactions* (Wiley, 1998).
- [26] S. Chu, J. E. Bjorkholm, A. Ashkin, and A. Cable, *Experimental Observation of Optically Trapped Atoms*, Phys. Rev. Lett. **57**, 314 (1986).
- [27] J. D. Miller, R. A. Cline, and D. J. Heinzen, *Far-Off-Resonance Optical Trapping of Atoms*, Phys. Rev. A. **47**, R4567 (1993).
- [28] T. Takekoshi, J. R. Yeh, and R. J. Knize, *Quasi-electrostatic Trap for Neutral Atoms*, Opt. Comm. **114**, 421 (1995).
- [29] T. Takekoshi and R. J. Knize, *CO₂ Laser Trap for Cesium Atoms*, Opt. Lett. **21**, 77 (1996).
- [30] T. Takekoshi, B. M. Patterson, and R. J. Knize, *Observation of Optically Trapped Cold Cesium Molecules*, Phys. Rev. Lett. **81**, 5105 (1998).
- [31] H. Engler, T. Weber, M. Mudrich, R. Grimm, and M. Weidemüller, *Very Long Storage Times and Evaporative Cooling of Cesium Atoms in a Quasi-electrostatic Dipole Trap*, Phys. Rev. A. **62**, 031402 (2000).
- [32] K. M. O'Hara *et al.*, *Ultrastable CO₂ Laser Trapping of Lithium Fermions*, Phys. Rev. Lett. **82**, 4204 (1999).
- [33] Z.-Y. Ma, A. M. Thomas, C. J. Foot, and S. L. Cornish, *The Evaporative Cooling of a Gas of Caesium Atoms in the Hydrodynamic Regime*, J. Phys. B. **36**, 3533 (2003).
- [34] A. Griesmaier, J. Werner, S. Hensler, J. Stuhler, and T. Pfau, *Bose-Einstein Condensation of Chromium*, Phys. Rev. Lett. **94**, 160401 (2005).

- [35] A. Mosk *et al.*, *Mixture of Ultracold Lithium and Cesium Atoms in an Optical Dipole Trap*, Applied Physics B **73**, 791 (2001).
- [36] M. Mudrich *et al.*, *Sympathetic Cooling with Two Atomic Species in an Optical Trap*, Phys. Rev. Lett. **88**, 253001 (2002).
- [37] J. Herbig *et al.*, *Preparation of a Pure Molecular Quantum Gas*, Science **301**, 1510 (2003).
- [38] M. Greiner, C. A. Regal, and D. S. Jin, *Emergence of a molecular Bose-Einstein condensate from a Fermi gas*, Nature **426**, 537 (2003).
- [39] M. Zwerlein *et al.*, *Observation of Bose-Einstein Condensation of Molecules*, Phys. Rev. Lett. **91**, 250401 (2004).
- [40] P. Jessen and I. Deutsch, *Optical Lattices*, Adv. Atom. Mol. Opt. Phys **37**, 95 (1996).
- [41] M. Lewenstein *et al.*, *Ultracold Atomic Gases in Optical Lattices: Mimicking Condensed matter Physics and Beyond*, cond-mat/0606771. To be published in 'Advances in Physics' (2006).
- [42] S. Friebe, C. D. Andrea, J. Walz, M. Weitz, and T. W. Hänsch, *CO₂-Laser Optical Lattice with Cold Rubidium Atoms*, Appl. Phys. B **67**, 669 (1998).
- [43] S. Friebe, R. Scheunemann, J. Walz, T. W. Hänsch, and M. Weitz, *Laser Cooling in a CO₂-Laser Optical Lattice*, Appl. Phys. B **67**, 669 (1998).
- [44] R. Scheunemann, F. S. Cataliotti, T. W. Hänsch, and M. Weitz, *An Optical Lattice with Single Lattice Site Optical Control for Quantum Engineering*, J. Opt. B. **2**, 645 (2000).
- [45] R. Scheunemann, F. S. Cataliotti, T. W. Hänsch, and M. Weitz, *Resolving and Addressing Atoms in Individual Sites of a CO₂-Laser Optical Lattice*, Phys. Rev. A **62**, 051801 (2000).
- [46] G. Cennini, G. Ritt, C. Geckeler, and M. Weitz, *Bose Einstein Condensation in a CO₂-Laser Optical Dipole Trap*, Appl. Phys. B **77**, 773 (2003).

- [47] G. Cennini, G. Ritt, C. Geckeler, and M. Weitz, *All-Optical Realization of an Atom Laser*, Phys. Rev. Lett **91**, 240408 (2003).
- [48] S. Magnier and M. Aubert-Fréon, *Static Dipolar Polarizabilities for Various Electronic States of Alkali Atoms*, J. Quant. Spec. Rad. Trans. **75**, 121 (2002).
- [49] P. F. Griffin, K. J. Weatherill, S. G. MacLeod, R. M. Potvliege, and C. S. Adams, *Spatially Selective Loading of an Optical Lattice by Light-shift Engineering using an Auxiliary Laser Field*, New. J. Phys **8**, 11 (2006).
- [50] P. F. Griffin, K. J. Weatherill, S. G. Macleod, R. M. Potvliege, and C. S. Adams, *Loading of Selected Sites in an Optical Lattice using Light-shift Engineering*, Proceedings of the XVII International Conference of Laser Spectroscopy (2005).
- [51] P. F. Griffin, *Laser Cooling and Loading of Rb into a Large Period, Quasi-Electrostatic, Optical Lattice*, PhD thesis, Durham University, 2005.
- [52] M. A. Nielsen and I. L. Chaung, *Quantum Computation and Quantum Information* (Cambridge, 2000).
- [53] D. P. DiVincenzo, *The Physical Implementation of Quantum Computation*, Fortschritte der Physik **48**, 771 (2000).
- [54] ARDA, *A Quantum Information Science and Technology Roadmap*, 2004, http://qist.lanl.gov/qcomp_map.shtml.
- [55] L. M. K. Vandersypen *et al.*, *Experimental Realization of Shor's Quantum Factoring Algorithm using Nuclear Magnetic Resonance*, Nature **414**, 883 (2001).
- [56] J. Chiaverini *et al.*, *Implementation of the Semiclassical Quantum Fourier Transform in a Scalable System*, Science **308**, 997 (2005).
- [57] S. Seidelin *et al.*, *Microfabricated Surface-Electrode Ion Trap for Scalable Quantum Information Processing*, Phys. Rev. Lett. **96**, 253003 (2006).

- [58] D. Jaksch *et al.*, *Fast Quantum Gates for Neutral Atoms*, Phys. Rev. Lett. **82**, 1975 (2000).
- [59] D. Jaksch, H.-J. Briegel, J. I. Cirac, C. W. Gardiner, and P. Zoller, *Entanglement of Atoms via Cold Controlled Collisions*, Phys. Rev. Lett. **82**, 1975 (1999).
- [60] O. Mandel *et al.*, *Coherent Transport of Neutral Atoms in Spin-Dependent Optical Lattice Potentials*, Phys. Rev. Lett. **91**, 010407 (2003).
- [61] O. Mandel *et al.*, *Controller Collisions for Multi-Particle Entanglement of Optically Trapped Atoms*, Nature **425**, 937 (2003).
- [62] M. Greiner, O. Mandel, T. Esslinger, T. W. Hänsch, and I. Bloch, *Quantum Phase Transition from a Superfluid to a Mott Insulator in a gas of Ultracold Atoms*, Nature **415**, 39 (2002).
- [63] M. Greiner, O. Mandel, T. W. Hänsch, and I. Bloch, *Collapse and Revival of the Matter Wave Field of a Bose-Einstein Condensate*, Nature **419**, 51 (2002).
- [64] D. Schrader *et al.*, *Neutral Atom Quantum Register*, Phys. Rev. Lett. **93**, 150501 (2004).
- [65] D. Haubrich *et al.*, *Observation of Individual Neutral Atoms in Magnetic and Magneto-Optical Traps*, Europhys. Lett **34**, 663 (1996).
- [66] I. Dotsenko *et al.*, *Submicrometer Position Control of Single Trapped Neutral Atoms*, Phys. rev. Lett. **95**, 033002 (2005).
- [67] Y. Miroshnychenko *et al.*, *Precision preparation of strings of trapped neutral atoms*, New. J. Phys. **8**, 191 (2006).
- [68] D. D. Yavuz *et al.*, *Fast Ground State Manipulation of Neutral Atoms in Microscopic Optical Traps*, Phys. Rev. Lett. **96**, 063001 (2006).
- [69] J. Vala *et al.*, *Perfect Pattern Formation of Neutral Atoms in an Addressable Optical Lattice*, Phys. Rev. A. **71**, 032324 (2005).

- [70] C. Zhang, S. L. Rolston, and S. D. Sarma, *Manipulation of Single Neutral Atoms in Optical Lattices*, Phys. Rev. A. **74**, 042316 (2006).
- [71] T. W. Hänsch and A. L. Schawlow, *Cooling of Gases by Laser Radiation*, Opt. Comm. **13**, 68 (1975).
- [72] D. Wineland and H. Dehmelt, *Proposed $10^{14} \Delta\nu < \nu$ Laser Fluorescence Spectroscopy on Ti^+ Mono-ion Oscillator III*, Bull. Am. Phys. Soc. **20**, 637 (1975).
- [73] S. Chu, *Nobel Lecture: The Manipulation of Neutral Particles*, Rev. Mod. Phys **70**, 685 (1998).
- [74] C. Cohen-Tannoudji, *Nobel Lecture: Manipulating Atoms with Photons*, Rev. Mod. Phys **70**, 707 (1998).
- [75] W. D. Phillips, *Nobel Lecture: Laser Cooling and Trapping of Neutral Atoms*, Rev. Mod. Phys **70**, 721 (1998).
- [76] C. J. Foot, *Atomic Physics* (Oxford University Press, 2005).
- [77] C. S. Adams and I. G. Hughes, *Handbook of Laser Technology and Applications: Vol III* (Institute of Physics, 2003), chap. D6.1.
- [78] U. Rapol, A. Krishna, and V. Natarajana, *Precise measurement of hyperfine structure in the $5P_{3/2}$ state of ^{85}Rb* , Euro. Phys. J. D. **23**, 185 (2003).
- [79] S. Chu, L. Hollberg, J. E. Bjorkholm, A. Cable, and A. Ashkin, *Three-Dimensional Viscous Confinement and Cooling of Atoms by Resonance Radiation Pressure*, Phys. Rev. Lett. **55**, 48 (1985).
- [80] J. Dalibard and C. Cohen-Tannoudji, *Laser Cooling Below the Doppler Limit by Polarization Gradients: Simple Theoretical Models*, J. Opt. Soc. Am. B **6**, 2023 (1989).
- [81] P. J. Ungar, D. S. Weiss, E. Riis, and S. Chu, *Optical Molasses and Multilevel Atoms: Theory*, J. Opt. Soc. Am. B. **6**, 2058 (1989).

- [82] Y. Castin, J. Dalibard, and C. Cohen-Tannoudji, *The Limits of Sisyphus Cooling*, Light Induced Kinetic Effects on Atom, Ions and molecules, Pisa: Eds L.Moi, S. Gozzini, C. Gabbaninni, E. Arimondo and F. Strumia. , 5 (1991).
- [83] C. Fertig and K. Gibble, *Measurement and Cancellation of the Cold Collision Frequency Shift in an ^{87}Rb Fountain Clock*, Phys. Rev. Lett. **85**, 1622 (2000).
- [84] E. L. Raab, M. Prentiss, A. Cable, S. Chu, and D. E. Pritchard, *Trapping of Neutral Sodium Atoms using Radiation Pressure*, Phys. Rev. Lett. **59**, 2631 (1987).
- [85] A. M. Steane, M. Chowdhury, and C. J. Foot, *Radiation Force in the Magneto-optical Trap*, J. Opt. Soc. Am. B. **9**, 2142 (1992).
- [86] C. G. Townsend *et al.*, *Phase-space Density in the Magneto-Optical Trap*, Phys. Rev. A. **52**, 1423 (1995).
- [87] C. J. Cooper *et al.*, *The Temperature of Atoms in a Magneto-optical Trap*, Europhys. Lett. **28**, 397 (1994).
- [88] W. Petrich, M. Anderson, J. Ensher, and E. Cornell, *Behaviour of Atoms in a Compressed Magneto-Optical Trap*, J. Opt. Soc. Am. B. **1**, 1332 (1994).
- [89] A. S. Arnold and P. J. Manson, *Atomic Density and Temperature Distributions in Magneto-Optical Traps*, J. Opt. Soc. Am. B. **17**, 497 (2000).
- [90] A. M. Steane and C. J. Foot, *Laser Cooling below the Doppler Limit in a Magneto-Optical Trap*, Europhys. Lett.. **14**, 231 (1991).
- [91] L. Allen and J. H. Eberly, *Optical Resonance and Two-Level Atoms* (Dover, 1987).
- [92] J. Jackson, *Classical Electrodynamics 3rd Ed.* (Wiley, 1999).
- [93] N. Davidson, H. J. Lee, C. S. Adams, M. Kasevich, and S. Chu, *Long Atomic Coherence Times in an Optical Dipole Trap*, Phys. Rev. Lett. **74**, 1311 (1995).

- [94] K. D. Bonin and V. V. Kresin, *Electric-Dipole Polarizabilities of Atoms, Molecules and Clusters* (World Scientific Press, 1997).
- [95] M. S. Safronova, C. J. Williams, and C. W. Clark, *Relativistic Many-Body Calculations of Electric-dipole Matrix Elements, Lifetimes, and Polarizabilities in Rubidium*, Phys. Rev. A **69**, 022509 (2004).
- [96] M. S. Safronova, B. Arora, and C. W. Clark, *Frequency-dependent Polarizabilities of Alkali-metal Atoms from Ultraviolet through Infrared Spectral Regions*, Phys. Rev. A **73**, 022505 (2006).
- [97] D. M. Brink and G. R. Satchler, *Angular Momentum* (Oxford University Press, 1968).
- [98] D. Suter, *The Physics of Laser-Atom interactions* (Cambridge University Press, 1997), .
- [99] R. Loudon, *The Quantum Theory of Light* (Oxford University Press, 2000).
- [100] J. E. Sansonetti, *Wavelengths, Transition Probabilities, and Energy Levels for the Spectra of Rubidium (RbI through RbXXXVII)*, J. Phys. Chem. Ref. Data. **35**, 301 (2005).
- [101] J. R. P. Angel and P. G. H. Sanders, *The Hyperfine Structure Stark Effect*, Proc. Roy. Soc. A. **305**, 125 (1968).
- [102] R. W. Schmieder, *Matrix Elements of the Quadratic Stark Effect on Atoms with Hyperfine Structure*, Am. J. Phys **40**, 297 (1972).
- [103] W. A. Wijngaarden, *Scalar and Tensor Polarizabilities of Low Lying S, P, D, F and G States in Rubidium*, J. Quant. Spec. Rad. Tran. **57**, 275 (1997).
- [104] G. Brooker, *Modern Classical Optics* (Oxford University Press, 2003).
- [105] A. E. Siegman, *Lasers* (University Science Books, 1986).
- [106] P. K. Ghosh, *Ion Traps* (Oxford Science Publications, 1995), chap. 5.

- [107] H. Perrin, A. Kuhn, I. Bouchoule, and C. Salomon, *Sideband Cooling of Neutral Atoms in a Far-detuned Optical Lattice*, *Europhys Lett* **42**, 395 (1998).
- [108] J. Kobayashi, Y. Izumi, M. Kumakura, and Y. Takahashi, *Stable All-optical Formation of Bose-Einstein Condensate using Pointing-Stabilized Optical Trapping Beams*, *Appl. Phys. B* **83**, 21 (2006).
- [109] V. Vuletić, C. Chin, A. J. Kerman, and S. Chu, *Degenerate Raman Sideband Cooling of Trapped Cesium Atoms at Very High Atomic Densities*, *Phys. Rev. Lett.* **81**, 5768 (1998).
- [110] C. S. Adams, S. G. Cox, E. Riis, and A. S. Arnold, *Laser Cooling of Calcium in a Golden Ratio Quasi-Electrostatic Lattice*, *J. Phys. B* **36**, 1933 (2003).
- [111] Y. Castin, *Bose-Einstein Condensates in Atomic Gases: Simple Theoretical Results*, *Lecture Notes of Les Houches Summer School*, 1 (1999).
- [112] P. F. Griffin, K. J. Weatherill, and C. S. Adams, *Fast Switching of Alkali Atom Dispensers using Laser-Induced Heating*, *Rev. Sci. Inst.* **76**, 093102 (2005).
- [113] C. J. Myatt, N. R. Newbury, R. W. Ghrist, S. Loutzenhiser, and C. E. Wieman, *Multiply Loaded Magneto-optical Trap*, *Opt. Lett.* **21**, 290 (1996).
- [114] Z. T. Lu *et al.*, *Low-Velocity Intense Source of Atoms from a Magneto-optical Trap*, *Phys. Rev. Lett.* **77**, 3331 (1996).
- [115] W. D. Phillips and H. Metcalf, *Laser Deceleration of an Atomic Beam*, *Phys. Rev. Lett* **48**, 596 (1982).
- [116] E. Riis, D. S. Weiss, K. A. Moler, and S. Chu, *Atom Funnel for the production of a Slow, High-Density Atomic Beam*, *Phys. Rev. Lett.* **64**, 1658 (1990).

- [117] K. Dieckmann, R. J. C. Spreeuw, M. Weidemüller, and J. T. M. Walraven, *Two-Dimensional Magneto-Optical Trap as a Source of Slow Atoms*, Phys. Rev. A. **58**, 3891 (1998).
- [118] H. Chen and E. Riis, *Cold Atomic Beam from a Rubidium Funnel*, Appl. Phys. B. **70**, 665 (2000).
- [119] K. Lee, J. Kim, H. Noh, and W. Jhe, *Single-Beam Atom Trap in a Pyramidal and Conical Hollow Mirror*, Opt. Lett. **21**, 1177 (1996).
- [120] J. Arlt, O. Maragò, S. Webster, S. Hopkins, and C. Foot, *A Pyramidal Magneto-Optical Trap as a Source of Slow Atoms*, Opt. Comm. **157**, 303 (1998).
- [121] N. Harris, *Modern Vacuum Practice* (McGraw-Hill, 1989).
- [122] S. G. Cox, P. F. Griffin, C. S. Adams, D. DeMille, and E. Riis, *Reusable Ultrahigh Vacuum Viewport Bakeable to 240 °C*, Rev. Sci. Instrum. **74**, 3185 (2003).
- [123] C. E. Wieman and L. Hollberg, *Using Diode Lasers for Atomic Physics*, Rev. Sci. Instrum. **62**, 1 (1991).
- [124] H. J. Davies and C. S. Adams, *Transferring Laser-Cooled Atoms to a Spatially Separated Magnetic Trap using a Far-off Resonance Optical Guide*, J. Phys. B **33**, 4079 (2000).
- [125] H. J. Davies, K. Szymaniec, and C. S. Adams, *Cold-atom Accumulation using an Optical Trap Door*, Phys Rev A **62**, 013412 (2000).
- [126] K. Szymaniec, H. J. Davies, and C. S. Adams, *An Atomic Fountain Guided by a Far-off Resonance Laser Beam*, Europhys. Lett. **45**, 450 (1999).
- [127] L. Ricci *et al.*, *A Compact Grating-Stabilized Diode Laser System for Atomic Physics*, Opt. Comm **117**, 541 (1995).
- [128] A. S. Arnold, J. S. Wilson, and M. G. Boshier, *A Simple Extended-Cavity Diode Laser*, Rev. Sci. Inst. **69**, 1236 (1998).

- [129] D. A. Smith and I. G. Hughes, *The Role of Hyperfine Pumping in Multilevel Systems Exhibiting Saturated Absorption*, Am. J. Phys **72**, 631 (2004).
- [130] M. L. Harris *et al.*, *Polarization Spectroscopy in Rubidium and Cesium*, Phys. Rev. A. **73**, 062509 (2005).
- [131] D. A. Smith, *Single-Impulse Magnetic Focusing of Launched Cold Atoms*, PhD thesis, Durham University, 2005.
- [132] A. Millett-Sikking, I. G. Hughes, P. Tierney, and S. L. Cornish, *DAVLL Lineshapes in Atomic Rubidium*, TJ. Phys. B. **40**, 187 (2007).
- [133] G. D. Rovera, G. Santarelli, and A. Clarion, *Laser Diode System Stabilized on the Caesium D_2 Line*, Rev. Sci. Instrum. **65**, 1502 (1994).
- [134] B. Cherón, H. Gilles, J. Hamel, O. Moreau, and H. Sorel, *Laser Frequency Stabilization using Zeeman Effect*, J. Physique III **4**, 401 (1994).
- [135] K. L. Corwin, Z.-T. Lu, C. F. Hand, R. J. Epstein, and C. E. Wieman, *Frequency-Stabilized Diode Laser with the Zeeman Shift in an Atomic Vapor*, Appl. Opt. **37**, 3295 (1998).
- [136] A. Ferguson, 2004, Private communication.
- [137] W. Demtröder, *Laser Spectroscopy 3rd Ed.* (Springer, 2003).
- [138] C. Wieman and T. Hänsch, *Doppler-Free Laser Polarization Spectroscopy*, Phys. Rev. Lett. **36**, 11170 (1976).
- [139] G. P. T. Lancaster, R. S. Conroy, M. A. Clifford, J. Arlt, and K. Dhoklakia, *A Polarisation Spectrometer Locked Diode Laser for Trapping Cold Atoms*, opt comm **170**, 79 (1999).
- [140] C. P. Pearman *et al.*, *Polarization Spectroscopy of a Closed Atomic Transition: Applications to Laser Frequency Locking*, J. Phys. B. **35**, 5141 (2002).
- [141] Y. Yoshikawa, T. Umeki, T. Mukae, Y. Torii, and T. Kuga, *Frequency Stabilization of a Laser Diode with use of Light-Induced Birefringence in an Atomic Vapor*, Appl. Opt. **42**, 6645 (2003).

- [142] W. Demtröder, *Laser Spectroscopy 3rd Ed* (Springer, 2003), chap. 7, pp. 463–476.
- [143] S. L. Cornish, 2003, Private communication.
- [144] D. Meschede, *Optics, Lasers and Light* (Wiley-VCH, 2004).
- [145] K. Singer, S. Jochim, M. Mudrich, A. Mosk, and M. Weidemüller, *Low-cost mechanical shutter for light beams*, *Rev. Sci. Inst* **73**, 4402 (2002).
- [146] L. P. Maguire, S. Szilagy, and R. E. Scholten, *High Performance Laser Shutter using a Hard Disk Drive Voice-coil Actuator*, *Rev. Sci. Inst.* **75**, 3077 (2004).
- [147] R.S., *IPL10050CW photodiode datasheet*, Website, 2006, <http://docs-europe.electrocomponents.com/webdocs/0318/0900766b80318e05.pdf>.
- [148] P. D. Lett *et al.*, *Optical Molasses*, *J. Opt. Soc. Am. B* **6**, 2084 (1989).
- [149] M. L. Boas, *Mathematical Methods in the Physical Sciences, 2nd Edition*. (Wiley, 1983), pp. 655–600.
- [150] M. A. Joffe, W. Ketterle, A. Martin, and D. E. Pritchard, *Transverse Cooling and Deflection of an Atomic Beam inside a Zeeman Slower*, *J. Opt. Soc. Am. B.* **10**, 2257 (1993).
- [151] W. Ketterle, K. B. Davis, M. A. Joffe, A. Martin, and D. E. Pritchard, *High Densities of Cold Atoms in a Dark Spontaneous-Force Optical Trap*, *Phys. Rev. Lett.* **70**, 2253 (1993).
- [152] C. G. Townsend *et al.*, *High-density trapping of cesium atoms in a dark magneto-optical trap*, *Phys. Rev. A.* **53**, 1702 (1996).
- [153] C. D. Wallace *et al.*, *Measurements of temperature and spring constant in a magneto-optical trap*, *J. Opt. Soc. Am. B.* **11**, 703 (1994).
- [154] W. T. Silfvast, *Laser Fundamentals* (Cambridge, 1996).

- [155] Coherent, *Gem Select 100 Datasheet*, Website, 2003, <http://www.coherentinc.com/downloads/ACF2C.pdf>.
- [156] S. Cornish, *Gaussian Beams and the Knife-Edge Measurement*, Website, 2006, http://massey.dur.ac.uk/resources/grad_skills/KnifeEdge.pdf.
- [157] M. Insrtuments, *Thermal Image Plates*, 2003, <http://www.macken.com/thermal.shtml>.
- [158] A. E. Siegman, *Lasers* (University Science Books, 1986), .
- [159] S. A. Self, *Focusing of Spherical Beams*, *Appl. Opt.* **22**, 658 (1983).
- [160] U. L. O. Optics, *CO₂mpact Manual Attenuator*, Website, 2004, http://www.vs-scientific.co.uk/docs/pdf/tdsulo_96_05.pdf.
- [161] H. J. Lewandowski, D. M. Harber, D. L. Whitaker, and E. A. Cornell, *Simplified System for Creating a BoseEinstein Condensate*, *Journal of Low Temperature Physics* **132**, 309 (2003).
- [162] W. Alt, *An Objective Lens for Efficient Fluorescence Detection of Single Atoms*, *Optik.* **113**, 142 (2002).
- [163] M. J. Pritchard, *Manipulation of Ultracold Atoms using Magnetic and Optical Fields*, PhD thesis, Durham University, 2006.
- [164] I. Dotsenko *et al.*, *Application of Electro-Optically Generated Light Fields for Raman Spectroscopy of Trapped Cesium Atoms*, *Appl. Phys. B.* **78**, 711 (2004).
- [165] C. C. Tannoudji and J. Dupont-Roc, *Experimental Studies of Zeeman Light Shifts in Weak Magnetic Fields*, *Phys. Rev. A.* **5**, 968 (1972).
- [166] R. B. Diener, B. Wu, M. G. Raizen, and Q. Niu, *Quantum Tweezer for Atoms*, *Phys. Rev. Lett.* **89**, 070401 (2002).
- [167] W. J. Hossack, E. Theofanidou, and J. Crain, *High-speed Holographic Optical Tweezers using a Ferroelectric Liquid Crystal Microdisplay*, *Opt. Exp.* (2003).

